DETERMINATION OF COARSE AGGREGATE MORPHOLOGICAL INDICES AND SHAPE PROPERTIES BY 3D PHOTOGRAMMETRY METHOD

A THESIS SUBMITTED TO
THE GRADUATE SCHOOL OF NATURAL AND APPLIED SCIENCES
OF
MIDDLE EAST TECHNICAL UNIVERSITY

BY

ISFANDIYAR RASHIDZADE

IN PARTIAL FULFILLMENT OF THE REQUIREMENTS
FOR
THE DEGREE OF MASTER OF SCIENCE
IN
CIVIL ENGINEERING

JANUARY 2021

Approval of the thesis:

DETERMINATION OF COARSE AGGREGATE MORPHOLOGICAL INDICES AND SHAPE PROPERTIES BY 3D PHOTOGRAMMETRY METHOD

submitted by **ISFANDIYAR RASHIDZADE** in partial fulfillment of the requirements for the degree of **Master of Science** i**n Civil Engineering, Middle East Technical University** by,

Prof. Dr. Halil Kalıpçılar
Dean, Graduate School of **Natural and Applied Sciences** _____

Prof. Dr. Ahmet Türer
Head of the Department, **Civil Enginering** _____

Assist. Prof. Dr. Hande Işık Öztürk
Supervisor, **Civil Engineering, METU** _____

Examining Committee Members:

Prof. Dr. Murat Güler
Civil Engineering, METU _____

Assist. Prof. Dr. Hande Işık Öztürk
Civil Engineering, METU _____

Assoc. Prof. Dr. Hediye Tüydeş Yaman
Civil Engineering, METU _____

Assist. Prof. Dr. Güzide Atasoy Özcan
Civil Engineering, METU _____

Assoc. Prof. Dr. Mustafa Kürşat Çubuk
Civil Engineering, Gazi University _____

Date: 05.01.2021

I hereby declare that all information in this document has been obtained and presented in accordance with academic rules and ethical conduct. I also declare that, as required by these rules and conduct, I have fully cited and referenced all material and results that are not original to this work.

Name Last name : Isfandiyar Rashidzade

Signature :

ABSTRACT

DETERMINATION OF COARSE AGGREGATE MORPHOLOGICAL INDICES AND SHAPE PROPERTIES BY 3D PHOTOGRAMMETRY METHOD

Rashidzade, Isfandiyar
Master of Science, Civil Engineering
Supervisor : Asst. Prof. Hande Işık Öztürk

January 2021, 103 pages

The morphological properties of the aggregates play a crucial role in the performance of the pavements. Therefore, there exist various empirical methods and image-based approaches that directly or indirectly measure these properties. Image-based approaches are majorly classified as two-dimensional (2D) or three dimensional (3D). It has been reported in many studies that the 3D methods capture the overall aggregate morphological and shape properties more accurately than any 2D alternatives. However, the equipment need in the 3D approaches are expensive and processing durations are extensively long. Therefore, this study aimed to develop a practical and inexpensive 3D photogrammetry based method to overcome the need for 3D imaging equipment. This study introduces a detailed guideline including a testing setup and analysis methodology to measure morphological indices (angularity and form indices) and also shape features (volume, surface area, and diameters). Overall 56 aggregates from basalt, dolomite, limestone, perlite, and river gravel sources that retained on 1/2" and 3/8" sieve sizes were analyzed utilizing the proposed 3D and traditional 2D methods. Moreover, sensitivity analysis based on triangulation and angle increments were performed to optimize the time and efficiency of the developed algorithm.

Consequently, the analysis revealed that the proposed 3D method is capable to accurately determine the shape features and morphological indices. This method can be successfully utilized as a quality control/assurance method by the construction industry.

Keywords: Coarse aggregate, image processing, morphological indices, shape features

ÖZ

KABA AGREGA MORFOLOJİK ENDEKSLERİNİN VE ŞEKİL ÖZELLİKLERİNİN 3B FOTOGRAMETRİ YÖNTEMİYLE BELİRLENMESİ

Rashidzade, Isfandiyar
Yüksek Lisans, İnşaat Mühendisliği
Tez Yöneticisi: Dr.Öğr.Üyesi Hande Işık Öztürk

Ocak 2021, 103 sayfa

Agregaların morfolojik özellikleri, kaplamaların performansında önemli bir rol oynar. Bu nedenle, bu özellikleri doğrudan veya dolaylı olarak ölçen çeşitli deneysel yöntemler ve görüntü işleme tabanlı yaklaşımlar vardır. Görüntü işleme tabanlı yaklaşımlar büyük ölçüde iki boyutlu (2B) veya üç boyutlu (3B) olarak sınıflandırılır. Birçok çalışmada, 3B yöntemlerin morfolojik ve şekil özelliklerini 2D alternatiflerden daha doğru bir şekilde yakaladığı bildirilmiştir. Bununla birlikte, 3B yaklaşımlardaki ekipman ihtiyacı pahalıdır ve işlem süreleri oldukça uzundur. Bu nedenle, bu çalışma 3B görüntüleme ekipmanı ihtiyacının üstesinden gelmek için pratik ve ucuz bir 3B fotogrametri tabanlı yöntem geliştirmeyi amaçlamıştır. Bu çalışma, morfolojik indeksleri (köşelilik ve form indeksleri) ve ayrıca şekil özelliklerini (hacim, yüzey alanı ve çaplar) ölçmek için bir test düzeneği ve analiz metodolojisi içeren ayrıntılı bir kılavuz sunmaktadır. 1/2” ve 3/8” elek üstünde kalan bazalt, dolomit, kireçtaşı, perlit ve nehir çakıl kaynaklarından elde edilen toplam 56 agrega, önerilen 3B ve geleneksel 2B yöntemleri kullanılarak analiz edilmiştir. Ayrıca, geliştirilen algoritmanın verimliliğini optimize etmek için üçgenleme ve açı artışlarına dayalı hassasiyet analizi de yapılmıştır. Sonuç olarak, yapılan analizler ile önerilen 3B yönteminin

şekil özelliklerini ve morfolojik indeksleri doğru bir şekilde belirleyebildiğini ortaya çıkarılmıştır. Bu yöntem, inşaat sektörü tarafından bir kalite kontrol / güvence yöntemi olarak başarıyla kullanılabileceği öngörülmüştür.

Anahtar Kelimeler: Kaba agrega, fotogrametri, görüntü işleme, morfolojik indeksler, şekil özellikleri

To my parents

ACKNOWLEDGMENTS

The author wishes to express his deepest gratitude to his supervisor Dr. Hande Işık Öztürk for her guidance, advice, criticism, encouragements and insight throughout the research.

The author would also like to thank Ahmet Sağlam and inters for their helps in laboratory experiments.

TABLE OF CONTENTS

LIST OF TABLES

TABLES

LIST OF FIGURES

FIGURES

LIST OF ABBREVIATIONS

ABBREVIATIONS

AI: Angularity Index

FI: Form Index

AI_{2D}: 2D Angularity Index

FI_{2D}: 2D Form Index

AI_{2D}^{avg}: Weighted awerage of 2D Angularity Indices

FI_{2D}^{avg}: Weighted awerage of 2D Form Indices

AI_{3D}: 3D Angularity Index

FI_{3D}: 3D Form Index

NAI_{3D}: Normalized 3D Angularity Index

NFI_{3D}: Normalized 3D Form Index

R^2: Coefficient of determination

LIST OF SYMBOLS

SYMBOLS

θ, ϕ: Azimuthal angles

$\Delta\theta$, $\Delta\phi$: Angle increments

CHAPTER 1

INTRODUCTION

1.1 Research Objectives and Scope

Flexible pavement is typically composed of a thick layer system, asphalt concrete placed on top of the granular base, subbase, and subgrade. The surface layer, asphalt concrete layer, of flexible pavements, is traditionally constructed by using an asphalt mixture. More than 75% of its volume is composed of aggregates [1]. It has been proved in many studies that the morphological properties of the aggregates affect performance such as workability, shear resistance, and durability of asphalt mixtures [2]. Therefore, it is important to precisely measure the morphology of aggregates in order to enhance the performance, and as well to analyze the effects of the morphology of particles on flexible pavement behavior.

There exist empirical standards (such as ASTM D3398, ASTM D5821) and image-based approaches (i.e. Aggregate Imaging Measurement System, University of Illinois Aggregate Image Analyzer) that directly or indirectly measure the morphological properties of aggregates. However, the traditional (empirical) methods are dependent on human precision during visual inspections and measures. Also, only a limited number of morphological properties can be measured by using these conventional methods [3]. On the other hand, various researchers have developed methodologies that measure the morphology of aggregates by using imaging technologies and correlated these properties with the mechanical mixtures of asphalt mixtures. Imaging technologies (such as X-ray tomography, digital cameras, laser, and optical scanners) enable researchers and practitioners to analyze particle geometry by using two-dimensional (2D) images or three dimensional (3D) models. In 2D methods, the researchers mostly use the direct output of cameras. On the other hand, 3D methods require the processing of the output of the devices

(X-ray tomography, laser scanner, etc.) to create 3D models. 2D approaches require single and multiple images from the different perspectives of aggregate to measure morphological indices. Utilizing multiple images in 2D approaches are assumed to procure 3D characterization while focusing on 3D shape information [4]. However, the 3D models capture the overall aggregate shape properties more accurately than any 2D alternatives [5]. However, the equipment (X-ray tomography, laser, and optical scanners) that are typically used in the 3D approaches, are expensive and processing durations are extensively long. On the other hand, there are a few preliminary attempts in the literature that utilizes 3D photogrammetry.

This study proposes a detailed guideline including a testing setup and analysis methodology to measure morphological indices (angularity and form indices) and also shape features (volume, surface area, and diameters) utilizing the triangulated 3D aggregate model that was obtained by 3D photogrammetry method. In this section, briefly, the analysis steps are summarized as follows. Firstly, a 3D model of the coarse aggregate is obtained by capturing photos of the sample from different views and creating a mesh of sample by using ContextCaptrure software. Secondly, the stick that was used to hold the sample is removed, and the surface of the aggregate is re-triangulated by using MeshMixer software. Thirdly, the output of the software is imported to the MATLAB to measure the volume, surface area, and centroid of the particle by using the coordinates of the triangles that represent the surface of the aggregate. Fourthly, diameters (line passes from centroid) are generated by using the ray-triangle intersection. Ray-triangle intersection algorithm allows creating artificial radii (lines from the centroid to the surface of the model) at any desired angle by using ellipsoidal (or spherical) to cartesian coordinate system conversion without using a bounding box. Lastly, morphological indices are calculated by using generated diameters. The proposed methodology is economical and time-efficient than the available 3D approaches in this literature.

This study also compares 3D morphological indices and shape features that are obtained by using 2D methods utilizing images from three different orthogonal perspectives. After preprocessing these images, by using the MATLAB, centroid,

area, and diameters of each orthogonal image calculated by using the boundary coordinates of binary images of each orthogonal image. 2D angularity and form indices are also calculated by using the diameters of all three perspective images.

Finally, to present the efficiency and precision of the proposed method, the morphological indices and shape features measured using the proposed 3D approach and traditional 2D approach are compared and discussed. Overall, this thesis presents a novel 3D approach for the estimation of 3D morphological indices.

1.2 Motivation

As briefly discussed in the previous section. it is essential to measure and express the morphology of aggregate particles in order to enhance the asphalt mixture properties. Although there exist conventional standards that measure only limited parameters, the results of these experiments are sensitive to the human factor. Since the focus of the image-based methods is to eliminate the human factors and obtain direct measures of these properties, various researchers have been attempting to develop precise, cost-effective, and time-efficient methods.

It has been acknowledged in many studies that are discussed in the Literature Chapter that 2D image-based methods are faster than 3D methods. On the other hand, 3D methods are more accurate than 2D approaches [4]. Although the need for level precision has not been addressed in any of the studies yet, most of the researchers have been developing 3D approaches that measure the morphology of aggregates. In these approaches, the researchers have been utilizing sophisticated and expansive equipment i.e. X-ray computed tomography, laser, and optical scanners. Considering the disadvantages of existing standards, 2D and 3D approaches in the literature, this study introduces a simple, economical (overall price is less than 1000$), accurate and detailed measure of the morphology of aggregates by using a 3D model created by photogrammetry method.

1.3 Outline of Research

Chapter 2 includes a broad literature review of the empirical and image-based approaches used to determine morphological indices of coarse aggregates.

Chapter 3 introduces the sample preparation and the setups that are used for the proposed 3D photogrammetry method and the traditional 2D approach.

Chapter 4 discussed the theories and developed algorithms for both proposed 3D photogrammetry method and the traditional 2D approach.

Chapter 5 contains results and a discussion of the analysis with respect to aggregate type and size. Moreover, this chapter handles the comparison between the proposed and 2D approaches. In addition, the efficiency and sensitivity of the proposed approach are presented.

Chapter 6 includes the conclusion driven according to the results and discussion. It also comprises recommendations for future studies.

CHAPTER 2

LITERATURE REVIEW

2.1 Introduction

Flexible pavements have two major compounds asphalt cement and aggregate. The asphalt cement provides the bonding within the aggregate structure. Aggregate structure and its properties play a major role in the overall performance of asphalt mixtures. As indicates in the previous chapter, the morphology of aggregates affects the workability, shear resistance, and durability of the asphalt structures. Thus, the quantification of morphological indices is essential for higher mixture quality and performance. Therefore, there have been several studies that correlate the physical properties of aggregates with pavement performance. In this section, various studies are summarized in order to presents the effects of morphology on the rutting resistance, adhesion property, void content, resilient modulus, and high-temperature resistance on flexible pavements, and as well to address the importance of this thesis study.

In the literature, the morphology of particles is typically expressed in terms of form index, angularity index, and texture. Form index reflects the variations in proportions. Angularity index describes the variations at corners of aggregate. Texture reflects the surface irregularity at a scale that is too small to affect the overall shape.[6][2][7]

In the literature, there exist many studies that focus on the effect of the morphology of fine and coarse aggregates on the asphalt mixture performance (workability, shear resistance, and durability). A limited number of these researches studying the morphology of coarse aggregates from different perspectives of performance are

summarized in this section to reveal the importance of morphology on the mixture performance, and also to reveal the importance of this study.

Chen et al. [8] investigated the influence of coarse aggregate shape on the asphalt concrete mixtures. The study focused on the effect of cubical and flat elongated particles on the rutting potential of the mixtures. It was observed that cubical particles showed higher rutting resistance than flat elongated particles.

Cui et al. [9] measured angularity and sphericity of limestone and basalt samples by using the Aggregate Imaging Measurement System (AIMS) and then studied the effect of these indices on the binder-aggregate bonding. Consequently, a linear relationship between angularity or sphericity of aggregates and asphalt coverage ratio was obtained. Moreover, it was reported that the higher angularity or lower sphericity showed better adhesion property (or greater coverage ratio).

Neham et al. [10] investigated the effects of morphological properties, shape and surface texture, of coarse aggregates on resilient modulus and Marshall properties of the asphalt mixtures. The study revealed that minimum Marshall Flow, minimum air void values, and maximum resilient modulus were achieved when cubical shaped and rough-textured aggregates were used.

Lei et al. [11] studied the effect of aggregate morphology on the spatial distribution of internal air void in the compacted asphalt mixture. In this study, the morphological properties of the aggregates were determined by AIMS. It was observed that aggregates with higher sphericity and lower angularity guarantee a more homogeneous spatial distribution of air voids in the compacted asphalt mixture.

Gao et al. [12] investigated the effect of angularity of coarse aggregates on skid resistance, high-temperature performance, and compactability of asphalt mixtures. The angularity of the aggregates was determined utilizing X-ray tomography. It was observed that lower angularity resulted in lower skid resistance and higher

aggregate angularity resulted in better high-temperature stability but caused difficulty in compaction.

As discussed with a limited number of studies, consideration of morphological indices in asphalt mixture design is essential to improve the performance. Thus, in order to estimate these morphological properties of aggregates, there exist various conventional and unconventional (image-based) methods. The conventional methods are mostly dependent on human precisions as discussed in the following section. Therefore, researchers introduced nonconventional methods in order to fully or partially automate the testing process by using image processing methods.

2.2 Conventional Methods

Conventional methods include laboratory testing methods that mostly depend on visual inspections or human precision and do not requires any image-based methods/tools to measure the geometric features of aggregates.

According to ASTM D3398 (Standard Test Method for Index of Aggregate Particle Shape and Texture) [13] particle shape and texture characteristics are measured in terms of particle index (PI). PI is calculated after detecting percent-vise void amounts for 10 and 50-rod drops. In this procedure, cylindrical mold is equally filled with aggregates in three steps. At each step, a rod is freely dropped 10 times to compact the particles. After the final layer, the mass of aggregate is measured. This process is also repeated for the 50-rod drops. Void percent for each step is calculated by using the measured mass, the bulk-dry specific gravity of aggregates, and the volume of the cylindrical mold. PI value is obtained by using a monograph or formula by inputting the void percent values.

ASTM D5821 (Standard Test Method for Determining the Percentage of Fractured Particles in Coarse Aggregate) [14] is guiding to detect the amount of fractured (angular) particles inside the coarse aggregate batch. In this procedure, the washed and dried aggregate samples are placed on a flat and clean surface so that the faces

of the aggregates are viewed directly. It is accepted that the fractured face of the particle should constitute at least one-quarter of the largest cross-sectional area. Inspecting the reference aggregate figures and samples' face the fractured samples manually separated by using a spatula.

ASTM D4791 (Standard Test Method for Flat Particles, Elongated Particles, or Flat and Elongated Particles in Coarse Aggregate) [15] is used to determine the percentage of flat, elongated, and flat and elongated particles in a coarse aggregate batch. Particles are grouped by using two different methods (method A and B) and both methods require the use of proportional caliper (**Figure 1**). The aggregate particles are categorized by checking the properties manually for each opening. In method A, the samples are grouped as flat, elongated, flat and elongated or neither flat nor elongated particles. The caliper's larger opening is equated to the maximum width of particle and aggregate labeled as flat if the maximum thickness can pass through the smaller opening. The particle is assumed to be elongated if the maximum width can pass through the caliper's smaller opening when the larger opening is equal to the maximum length of the particle. In method B, the particles are grouped as flat and elongated or not flat and elongated. The proportional caliper's longest opening equated to aggregate's longest length and particle assumed to be flat and elongated if its maximum thickness can pass through the smaller opening.

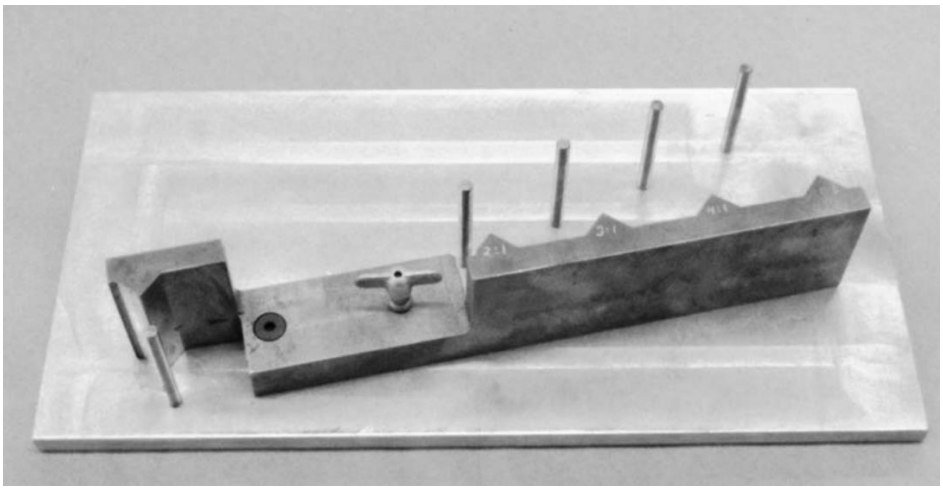

Figure 1 Proportional caliper [15]

As summarized above, none of the above-mentioned standards are capable of directly measuring the morphological indices. The existing standards mostly qualitatively measure the morphology of aggregates. Thus, the researchers have developed nonconventional methods as discussed in the following section.

2.3 Nonconventional Methods

Nonconventional methods are the methods that measure the morphological indices of aggregates by using image-based methods. Image-based methods can be categorized into two as: (i) two-dimensional (2D) methods and (ii) three dimensional (3D) methods with respect to the imaging tool used. In the litrature, the proposed methods are very different from each other in the order of values of the morphology properties. Moreover, the studies introduced different indices and even indices that has the same name were calculated by using the different formulas. Therefore, there is not unique formula and range of indices for the image-based non-convetional methods.

2.3.1 2D Methods

This chapter reviews studies that measure morphological indices and/or shape features by analyzing single or multiple images without creating the 3D model of the aggregate particles. Typically, for the studies that use multiple images, single or multiple cameras are used to capture the 2D images of aggregates from different perspectives. Starting by the early 1930's [16], researchers attempted to gather morphological properties of the aggregates using image-based tools. Therefore, till now, there have been various approaches developed by researchers. Thus, a limited number of the latest innovative studies and well-accepted studies are discussed in this section. It should be noted that the calculation of 2D indices is discussed separately in Chapter 3 in detail.

Most well-known 2D approach was developed and later improved by Masad et al. [17]. Form index (FI) is the sum of the changes in radius, and angularity index (AI) is the measure of the difference between the particle radius and equivalent ellipse radius. In order to calculate the indices of fine and coarse aggregates, the researchers captured 2D gray-scaled images of particles by using the setup shown in **Figure 2**. In this thesis, AI and FI that were developed by Masad et al. were also used in order to compare the result of the proposed 3D approach and the traditional 2D method. The details of these indices were given in Chapter 4. U.S Federal Highway Administration [18] reported the target price of the 1st phase of the AIMS project as 30000$.

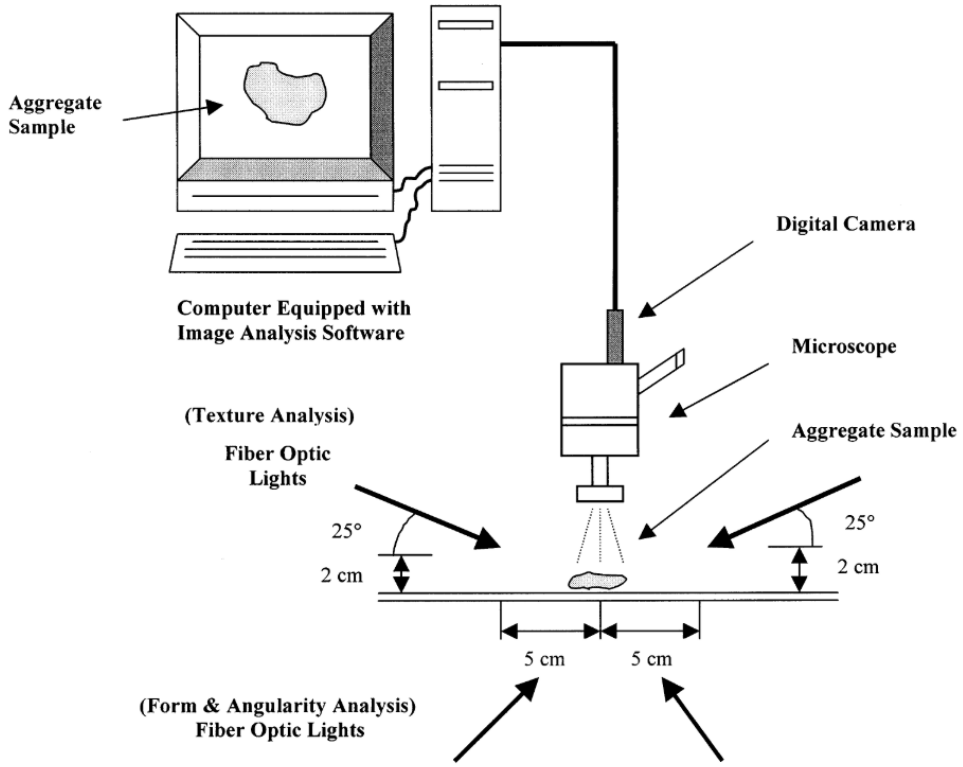

Figure 2 Experimental setup to capture fine aggregates [17]

Another well-known setup and procedure were developed by Rao et al. [19], named as University of Illinois Aggregate Image Analyzer (UI-AIA). The system is capable of determining the dimensions, volume, flat, and elongated ratio by using the images of coarse aggregates taken from three orthogonal directions. The schematic view of UI-AIA is shown in **Figure 3**. An infrared and a fiber optic sensor activates the cameras to capture the images of aggregate that is transported from the feed bin on the conveyor belt. In this setup, each camera captures $640x480$ pixels grayscale images. The grayscale images are converted to binary (black and white) images in order recognize the regions of aggregate. The researchers calculated volume of bounding box (assumed to be volume of aggregate) that created by merging minimum bounding rectangles which drawn around each orthogonal image of aggregate. The authors defined longest dimension and the dimension that perpendicular to longest from orthogonal images in order calculate the flat and elongated ratio. Later, Rao et al. [20] presented a new AI that

was calculated by using the images obtained by UI-AIA. Different than AI proposed by Masad, this AI considers the change in the slope of particle boundary and uses three orthogonal images of aggregate. In this procedure, boundary coordinates of aggregate were extracted from the binary image and each boundary coordinate equally away from its neighbor was located in clockwise direction. The subtended angle was calculated for each coordinate. The slope changes subsequently were calculated by taking the difference of angle at each coordinate and the angle in the preceding (neighbor that is located in the clockwise direction) coordinate. The frequency distribution of angle changes was recorded for 10^0 intervals. The10^0 incremental intervals (e) and the probability of slope change having value ($P(e)$) in that interval is used to calculate angularity (A_{Rao}) as given in **Eq. 2-1**. The researchers calculated angularity for each orthogonal image of aggregate and took the weighted average of these three angularities as new AI of aggregate.

$$A_{Rao} = \sum_{e=0}^{170} e * P(e) \qquad \text{Eq. 2-1}$$

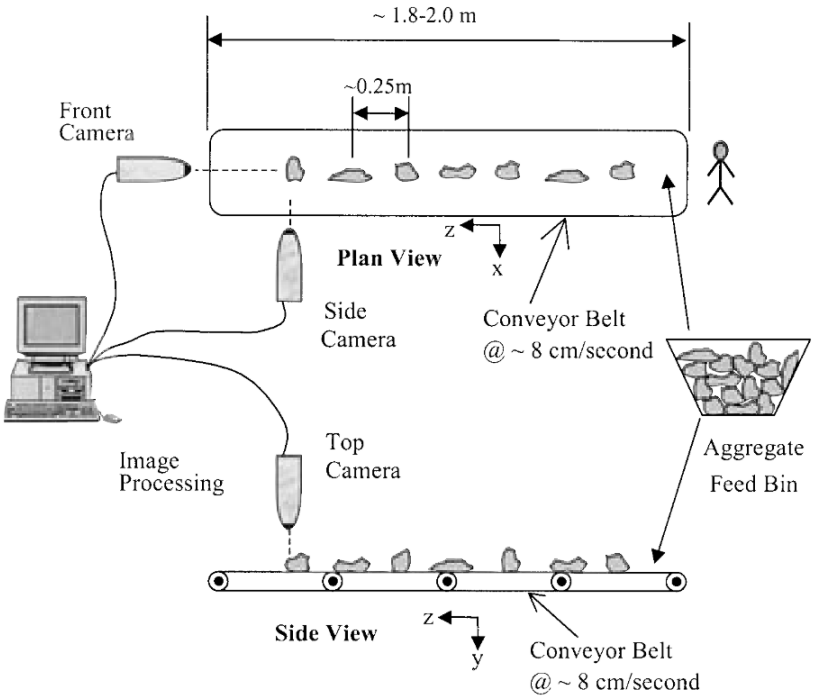

Figure 3 Schematic view of UI-AIA [19]

Later, Xu et al. [21] compared the angularity indices calculated by the methods proposed by Masad et al. and Rao et al. with an online survey, which was conducted with six pavement engineers. The engineers rated the angularity of aggregates as shown in **Figure 4**. The authors found that both angularity indices linearly correlated with the responses of engineers.

Figure 4 Survey to rate the angularity of aggregate [21]

In a relatively new study, Descantes et al. [22] measured morphological properties of railway ballast by using a video analyzing device (VDG40 video grader) as shown in **Figure 5**. The device working by using the shadowgraph principle to capture images of aggregate particles. The camera captures the image of the aggregate while the particle falls freely between the camera and light source. In order to capture images, a charge-coupled device (CCD), a line camera is mounted to the device. The researchers analyzed angularity and roughness by using boundary coordinates of samples. In order to calculate angularity of aggregate (ANG), the researchers detected straight lines along the surface of aggregate by using Hough transform technique. Then, ANG was calculated by taking the mean value of sharpest salient angles between two adjacent straight lines as given in **Eq. 2-2**.

$$ANG = \frac{1}{n}\sum_{i=1}^{n} 1 - \frac{\alpha_i}{180^0}$$ Eq. 2-2

- ANG: Angularity of aggregate
- n: Number of angles considered
- α_i: Salient angle between two adjacent straight lines

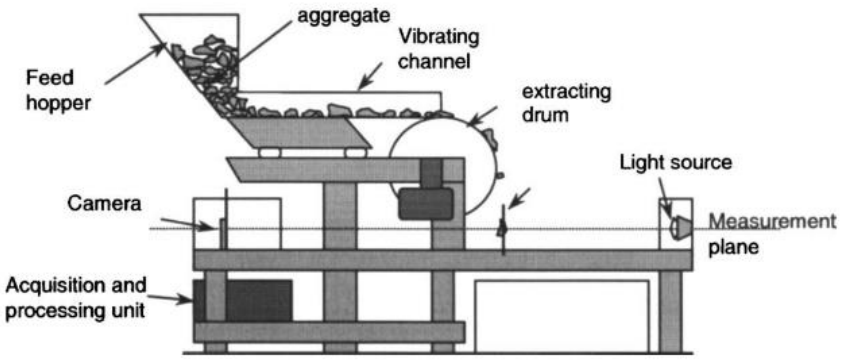

Figure 5 VDG40 overview [22]

In another recent study, Xie et al. [23] used digital image processing to measure the morphological indices of fine aggregates. In order to take pictures of fine particles, the researchers used a stereomicroscope device (**Figure 6**). The authors test Ceramic, Sand, Andesite, and Limestone in 1.18 mm, 0.6 mm, and 0.3 mm grain sizes. The researchers used Image Pro-Plus software to obtain perimeter, area, and dimensions. The authors measured sphericity by using the major and minor axis of equivalent ellipse and rectangularity by using the smallest bounding rectangle area. The researchers obtained a very good correlation with the results obtained from using image processing and with the results of the Sand Flow Test and Uncompacted Void Content Test.

Figure 6 Stereomicroscopy [23]

As summarized with a limited number of studies, there are various attempts utilizing different image capturing procedures, devices, and calculation methodologies for morphological indices. Consequently, all these approaches are valuable to precisely determining these parameters. Moreover, various researchers came up with innovative approaches using artificial intelligence to determine these indices from the bulk of aggregates (stockpiles). A few of those studies are summarized in this section.

As a recent innovative approach, Huang et al. [24] developed an approach that automatically segments and analyzes the morphology of stockpile by using deep learning. In this study, the researchers manually labeled aggregates in 164 stockpile images (11795 aggregates) to train the model. Plus, 20 additional images were taken to validate the model as shown in **Figure 7a** and **7b**. Basically deep learning model learns to identify aggregate from images by using the training dataset (images) and rates its learning accuracy by using the validation dataset. R-CNN (Regions with Convolutional Neural Network [25]) framework was used to detect the regions where aggregates were located. Then, the researchers used LCN

(Fully Convolutional Networks for Semantic Segmentation [26]) framework to detect aggregates separately. In order to obtain unit lengths, a 2.25 in reference ball was placed into the stockpile before taking the images. The researchers were able to calculate equivalent spherical diameter, flat and elongated ratios from segmented aggregate particles. The authors compared the detected aggregates' and manually labeled aggregates' equivalent sizes and flat and elongated ratios by plotting histogram and cumulative distribution graphs and the trends were almost similar. Consequently, Huang et al. developed a fully automated approach for detecting a limited number of morphological indices.

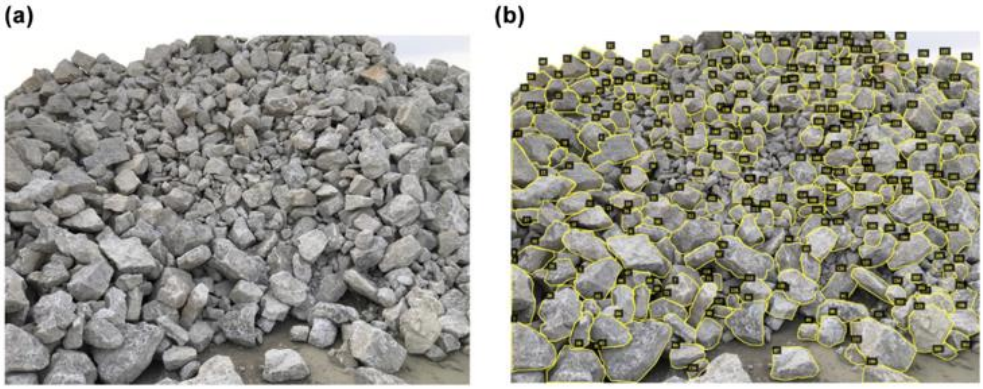

Figure 7 Stockpile image a) original stockpile image b) manually labeled aggregates [24]

Another recent innovative study by Pei et al. [27] used machine learning algorithm (extreme gradient boosting classification or XGBoost) to classify aggregates according to the shape by using 2D images. The image acquisition system that the authors used is shown in **Figure 8** and it is composed of Basler Aca1300-60gm industrial camera with Edmund Optics CFFL F1.3f 8.5 mm 2/300 lens, light source, and background plate. The authors applied a median filter to denoise the image and the then high increment filter to sharpen the edges of the particle. The researchers further applied different kernels to pre-process the images and at the end obtained binary images of samples. By using the chi-square test, mutual information method, and tree model methods the authors carried future importance analysis to decrease training time and increase the performance of classification. The authors used 1624 samples in the project and reached 78% accuracy in

classifying the aggregates to cubical, angular, irregular, flat, elongated, and flat and elongated types.

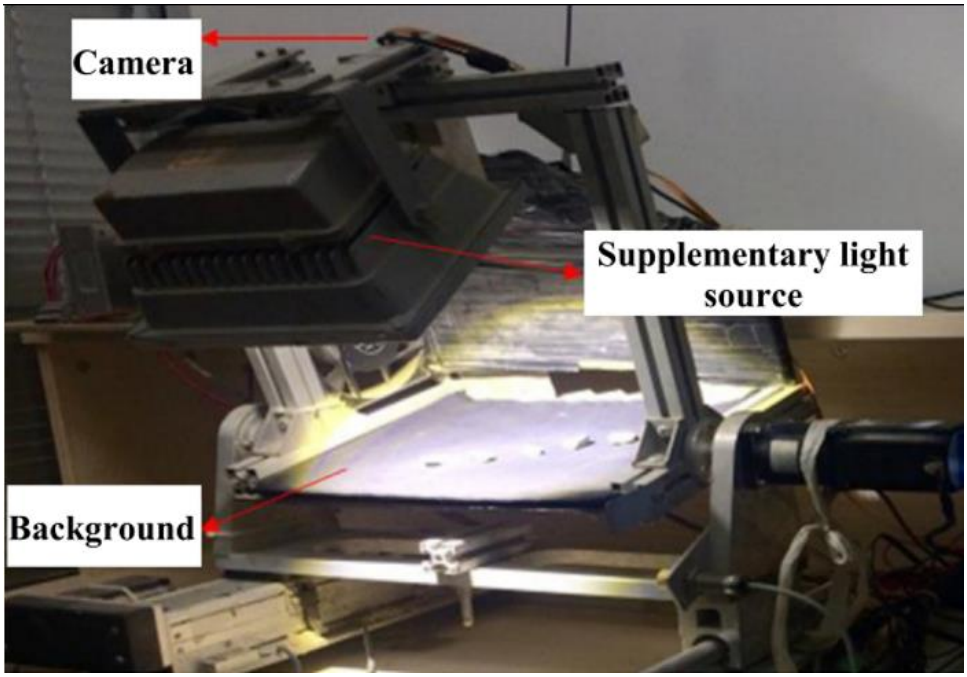

Figure 8 Aggregate image acquisition system [27]

To sum up, 2D approaches are still popular due to their ease, cost-effectiveness, and time efficiency. Moreover, studies to improve these approaches continue and their use is expending day-by-day.

2.3.2 3D Methods

This section discussed different devices and methods to create 3D models of aggregates. Since there have been various studies on this subject, a limited number of studies were summarized. The aim of this section was to present the use of different devices such as X-Ray tomography and different types of scanners.

The pioneering study by Garboczi [28] used X-ray tomography in order to represent aggregates in 3D by using spherical harmonic function techniques. The researchers used the grayscale concrete image obtained from tomography as shown in **Figure 9**. The real size of samples is $108\,mm^3$ and high-density particles

(aggregates) are appeared to be white. In order to separate contacting aggregates, the researchers used the Burning algorithm. After finding surface points of aggregates, the researchers applied spherical harmonic analysis. Obtaining spherical harmonic constants, the morphological indices were determined, as well the shape features such as volume and surface area of aggregate were also calculated using the generated 3D models.

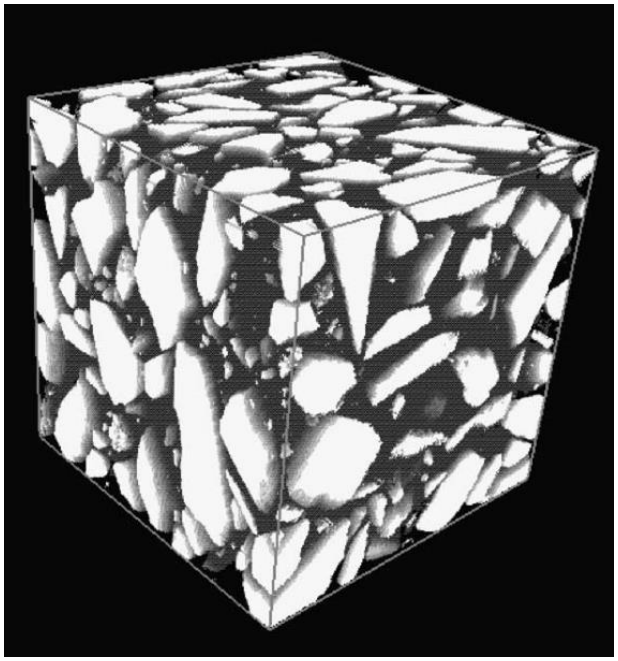

Figure 9 Grayscale image obtained from X-ray tomography [28]

In a recent study, Jin et al. [29] measured the properties of the aggregates by using a 3D solid model obtained from X-ray Computed Tomography (CT) imaging. The researchers calculated the sphericity index by dividing the radius of a sphere with a volume equivalent to the aggregate by the radius of the minimum bounding box. To calculate dimension index, the ratio of axes of aggregate, the researchers used the minimum bounding box dimensions.

In another recent study, Yang et al. [30] determined 3D AI and surface texture index (STI) of aggregates by using X-ray scanning. The authors used 15 coarse aggregates and covered each particle with paper in order to prevent contact with each other. The researchers scanned the samples with 0.1 mm intervals in the

vertical direction and rescaled the original images and then divided the entire surface $0.1x0.1\,mm$ squares to obtain cubic voxels. The voxels of the particles were visualized by using Abaqus software as shown in **Figure 10**. The researchers used 3D Sobel-Feldman operation to calculate the gradient direction of voxels. Accordingly, AI was calculated based on the change of gradient vector of surface voxel and STI based on the change of voxel amounts after a morphological operation.

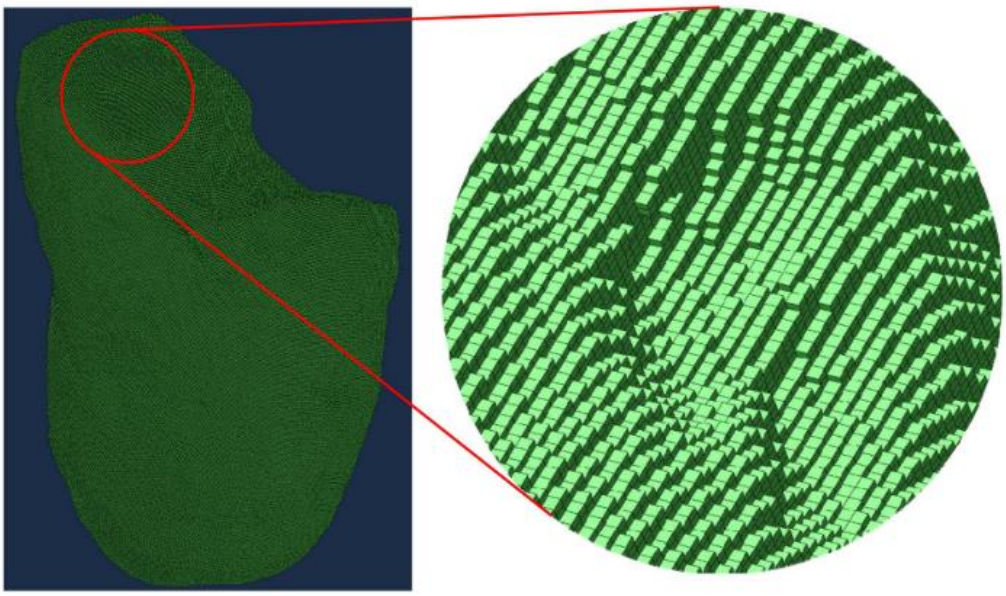

Figure 10 3D voxels visualized in Abaqus [31]

In another well-known study, Kutay et al. [2] analyzed different morphological indices of aggregates obtained from 2D and 3D methods. The researchers captured 2D grayscale images of aggregates by using AIMS and 3D images by using X-ray CT scanning. The researchers converted 2D grayscale images to binary images and analyzed these in MATLAB. On the other hand, the researchers applied threshold and labeled the outputs of X-ray CT by using X-ray CT Analysis Toolbox (XCAT) software developed by authors and converted to perimeter image, where the boundary of aggregate was white and rest was black. The researchers obtained the 3D Cartesian coordinates of each boundary voxel from perimeter images and converted them to spherical coordinates to determine the spherical harmonic

coefficients. The paper compared the 3D FI with 2D Form Factor [32], Shape Index [33] and Form Index [17] and obtained that trends were similar. The researchers also compared the 3D AI with different 2D angularities and observed a high correlation with 2D AI suggested by Masad which is also used in this study (Chapter 4).

The researchers [34] reported that the industrial X-ray CT devices' costs in the range of 60000 to 1000000 Euros. The X-ray CT device is the most expensive device utilized in 3D approaches. Moreover, the majority of the papers missed to mention the sample preparation and run durations, which is quite lengthy based on the hands-on experience.

As an alternative 3D imaging method, Kim et al. [4] characterized individual aggregate particles using a Laser-based Aggregate Scanning System (LASS) which utilized wavelet-based 3D particle descriptors. The researcher designed LASS prototype that was composed of a laser scanner fixed to a linear motion slide and passes over the aggregate sample as shown in **Figure 11**. The components of the prototype cost more than 20000$. The researchers measured the shape, angularity, and texture indices of aggregates from rounded limestone, river gravel, crushed limestone, crushed quartzite, and crushed granite sources. After scanning the aggregate from the top, the researchers converted 3D Cartesian coordinates of the particle to the polar coordinate domain and interpolated the bottom portion of the aggregate that was hidden from the scanner. The coefficients obtained from fine, middle, and coarse scaled wavelets were used to measure texture, angularity, and shape of aggregate, respectively. The researcher scanned particles twice to minimize possible data loss and analyzed outputs of LASS in LabView and Wavelet and Filter Bank Design Toolkit software. To validate the shape indices, the authors scanned twenty equidimensional and flat and elongated particles and revealed high correlations. The AI showed strong agreement with the visually separated round and angular samples selected by using ASTM D2488. Similarly, the researchers compared texture obtained from the analysis versus visually

separated rough and smooth aggregate particles and also obtained promising correlation.

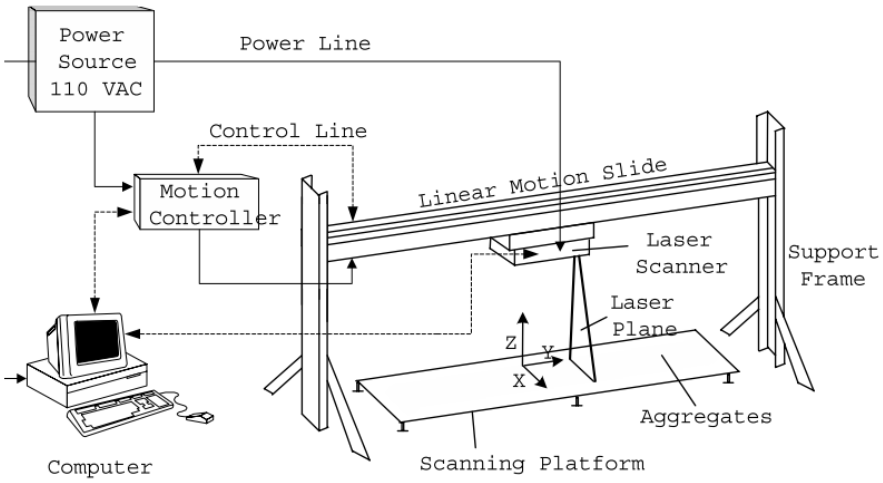

Figure 11 Laser-based aggregate scanning system (LASS) [4]

Another device was introduced by Sun et al. [35]. The shape characteristics of coarse aggregate were measured from point cloud data which was obtained by using an imaging system based on Gocator 3D intelligent sensor. The light emitter emits blue structured light to the surface of aggregate and reflected lights from the sample captured by the cameras as shown in **Figure 12**. The sensor has 0.5 mm accuracy in X, Y directions and 0.006 mm accuracy in the Z direction. The researchers stored point cloud coordinate information of 16bit RGB images in ImageX, ImageY, and ImageZ channels. Since the sensor is more sensitive to the environment in Z direction (height information), the researchers applied median filtering to ImageZ. The researchers used the Greedy Triangulation algorithm that triangulates the surface topography of the particles from the 3D point cloud data. The researchers obtained the length and width of aggregate from the minimum bounding rectangle, and the height directly from Gocator's output. The researchers also measured shape indices such as isometric ratio (measures elongation), flakiness ratio (thickness-width ratio) by using the measured dimensions, and sphericity index by using the maximum diameter of the convex hull that enclosed

point cloud. The authors measured the roundness, which measures the sharpness of projection of particle, using the perimeter and area of the projected shape.

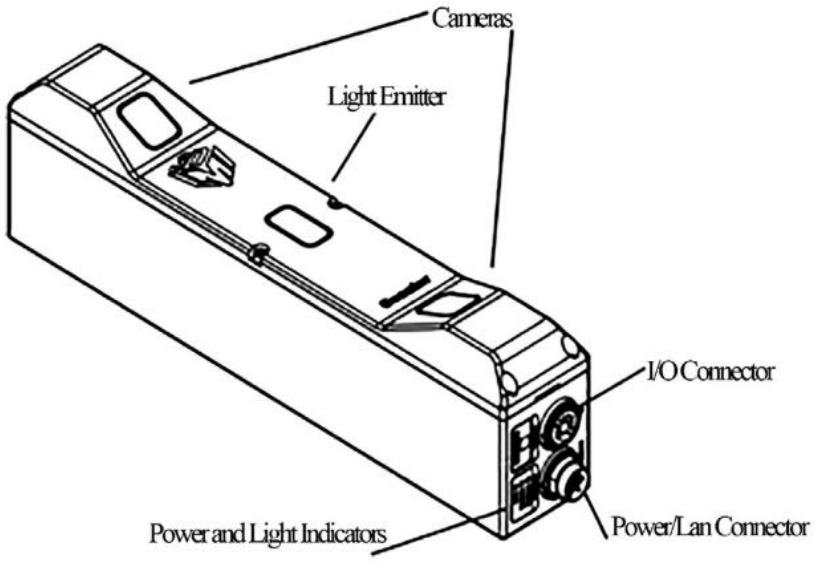

Figure 12 Structure of Gocator sensor [35]

In a recent study, Liu et al. [3] analyzed aggregates by using an optical scanner and validated the findings with X-ray CT analysis. The optical scanner consists of two cameras, one projection lens and a tripod as shown in **Figure 13**. The researchers scanned aggregates placing samples on the rotating turntable. The researchers used YXLON (Germany) industrial X-ray CT device in order to get high-resolution images of aggregates. The authors compared areas and volumes obtained from both imaging techniques and observed that round and angular particles' volume was mostly 4% and area 3% different. The difference between volume and area for flat or elongated particles was more than 7% and 5%, respectively.

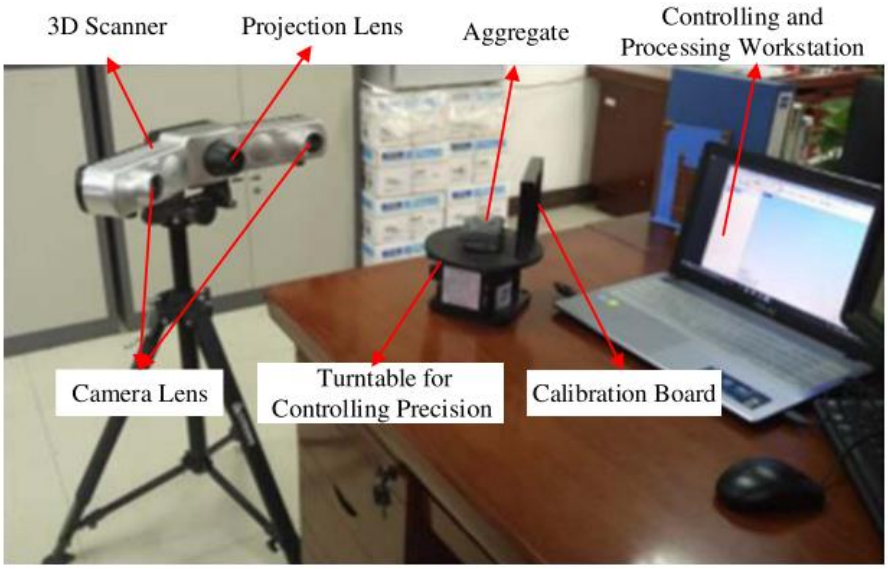

Figure 13 3D optical scanning [3]

In another recent study based on 3D photogrammetry, one of the early attempts was made by Heidelberg et al. [36]. In this study, a spherical harmonic model of aggregates was reconstructed by recording a video of aggregate particle by using a smartphone. The researchers stabilized aggregate on a rotating plate by using modeling clay. The smartphone placed on a tripod and recorded the 1,080-pixel resolution and 60 frames per second (fps) video of aggregate while rotating as shown in **Figure14**. The researchers used 3DF Zephyr Free software to extract images from the video file and mesh the surface of the particle. To scale the sample, the authors measured one dimension of the aggregate by using a caliper. The researchers used MATLAB to use spherical harmonic functions. However, this study was very limited.

Figure 14 Aggregate with smartphone camera setup [36]

In another early 3D photogrammetry approach, Zhao et al. [37] used a photographic system to model rocks in 3D and measure the morphological indices. The researchers placed the particle on a rotating table and captured its images with three cameras from different heights as shown in **Figure 15**. The researchers used Airsoft Photoscan software to obtain a 3D mesh of aggregate particles from the captured images. The researchers also scanned the particles with a laser scanner in order to analyze the accuracy of the photogrammetry approach. Thus, the deviation histogram of particle gathered by using two approaches were analyzed. Eventually, it was concluded that the accuracy of models obtained by photogrammetry were precise enough.

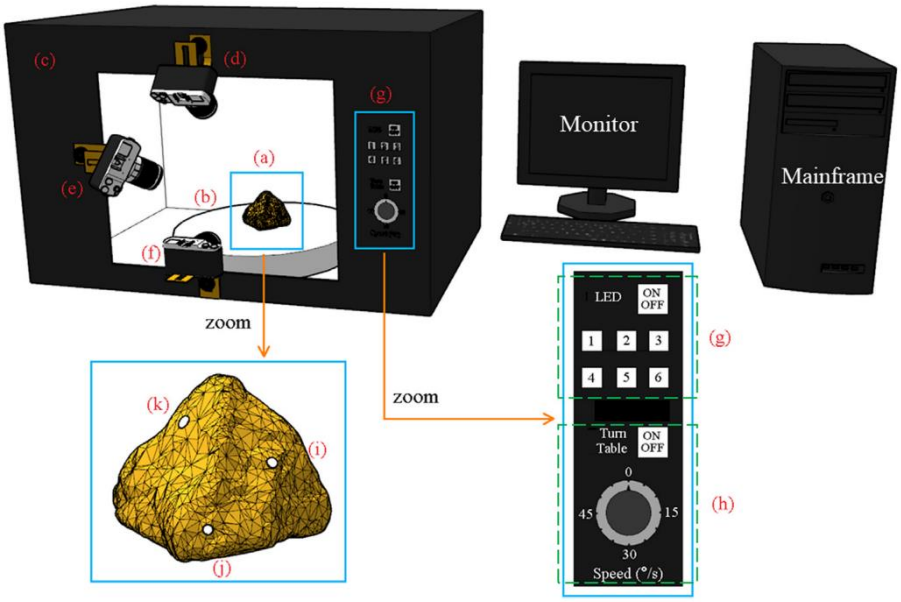

Figure 15 Photographic system [37]

As a summary, in recent years, various researchers attempted to develop 3D methodologies to precisely evaluate the morphological indices utilizing different devices. However, majority of these methods requires expensive testing setups that cannot be available in the majority of the laboratories.

2.4 Summary of the chapter

This chapter briefly introduces the well-known 2D and 3D methodologies in the literature. As discussed above, all these methodologies have advantages and disadvantages. Therefore, the aim of this study is to propose a methodology that is easy and less costly like 2D methods and also, as precise as 3D methods. The detail of the proposed methodology is presented in the following chapters.

Among the costs of setups from the literature, it was determined that the price of the devices that used both in 2D and 3D methods were more than 20000$. On the other hand, the price of this project including Nikon digital camera, tripod and three continuous lightings (another two lightings were provided by the department) the total cost of the project was less than 1000$.

CHAPTER 3

MATERIALS, SETUPS AND IMAGING PROCEDURES

This chapter discusses details about the aggregate source and number, sample preparation, capturing the images of aggregate for both 3D and 2D approaches. Also, obtaining 3D model of aggregate and editing the model explained in detail.

3.1 Aggregate Types

In order to identify the shape and morphological indices, 56 aggregates were analyzed in this study utilizing the proposed photogrammetry method and traditional 2D approaches. In the experimental matrix, aggregates were initially categorized according to their sizes and sources (or type). Five aggregate types were determined as basalt, dolomite, limestone, perlite, and river gravel based on their dominant shape characteristics and frequency of use in the construction sector. Basalt, limestone, and dolomite are the typical sources that are used in flexible pavement construction. River gravel was selected as its morphological indices are significantly different from the other sources. Perlite, a light aggregate, is not a typical aggregate source for road construction but added to the experiment matrix to validate the calibration of the proposed methodology. Moreover, two coarse aggregates sizes were selected as retaining on $1/2$″ and $3/8$″ sieves for each source. The details on the number of aggregates analyzed per aggregate type and size were presented in **Table 1.**

Table 1 Number of aggregates for each type and retaining sieve size.

Type	Size	
	1/2"	3/8"
Basalt	4	5
Dolomite	8	7
Limestone	4	5
Perlite	5	5
River Gravel	7	6
Total	**28**	**28**

3.2 Procedures of Creating 3D Model

3.2.1 Sample Preparation

In order to capture the 2D images of the aggregates from different angles, the aggregate was initially glued to a rod from its major axis to keep it stable during the photoshoot. If not, not hardened glue or using a rope to hang the aggregate will result in defects in the 3D model. In order to provide the desired stability of the setup, 5 minutes two-component epoxy was used to stick the aggregate to a 1 mm diameter metallic stick. The stick was positioned perpendicular to the approximate center of the aggregate and the setting took about half an hour (**Figure 16b)**.

It should be noted that the amount/type of the glue and the diameter of the stick was optimized after various trials and errors. While editing the 3D model of the aggregates, the glue and stick were removed from the model. If they cover more surface on the aggregate, the deleted portion of the aggregate might lead to an accuracy problem. Thus, this step in the procedure is a bit tricky and needs fine work.

Moreover, if the surface color of the aggregate was uniform, the software can mismatch the points on the surface and this may result in errors in the 3D model. Therefore, in order to obtain the correct representation of aggregate, random lines/dots were drawn on the surface of aggregates with colored pencils.

In order to determine the actual sizes of the aggregates, circular papers with $2.05\,mm$ (**Figure 16b**) or $1.97\,mm$ diameters were attached on the surface of aggregates as reference dimensions. It should be noted that the shape and size of the reference paper are not essential for the procedure and users to implement this methodology can attach a reference in different shapes or sizes. However, the reference paper should be as small as possible in order to avoid covering the irregularities on the surface of the aggregate.

3.2.2 Setup

In this study, for the proposed photogrammetry method and traditional 2D approaches, the pictures were captures using a handheld DSR camera, Nikon D3400 digital camera with an 18-5 mm lens. The size of each image is approximately 6 MG and dimensions 6000x4000 pixels.

In order to get high-resolution 3D models, it is essential to light the aggregate properly during the photo shoot. Therefore, the aggregate were lightened by three continuous lights (800W) with reflectors at the level of aggregate's height, which were positioned approximately 120^0 apart from each other. In order to get a correct representation of the aggregate, the white reflectors are covered with newspapers. Since the 3D modeling software take the background as a reference during rendering (when the image does not have positioning information), the non-uniform background will help the photogrammetry programs render correctly.

In addition, shadows were eliminated by placing two more continuous lights (800W) with softboxes which reflected the light from a higher elevation. The locations of these lights were chosen randomly according to the lighting needs (**Figure 16a)**.

Figure 16 3D photogrammetry setup a) setup b) aggregate

3.2.3 Photography

During the photo shoot, the camera should be held 20-30 cm away from the aggregate and zoom should not be used. Also, the flash of the camera should be turned off. Photos of the aggregate were taken by elevating the camera at five different heights by using a tripod as shown in **Figure 17a**. Starting from the mid-height of aggregate (**elevation 0**), approximately 50 images 7^0 apart from each other were taken by moving in a circular motion as shown in **Figure 17b**. Changing the elevation of the camera approximately 45^0 higher than **elevation 0,** approximately 20 images, which were 18^0 apart from each other, were captured **in elevation 1**. For **Elevation 2,** the elevation of the camera was positioned approximately $\mathbf{45^0}$ lower than **elevation 0** and images were captured similar to Elevation 1. Finally, for the **elevation 3** and **4,** the camera positioned nearly 80^0 away from the **elevation 0**. These elevations should not be 90^0 to eliminate the shadows of the camera on the aggregate's surface. Ten more photos were taken at these final elevations. Positions of the cameras were presented from top and side, in **Figures 17b** and **17c,** respectively. Overall imaging procedure takes 30-45 minutes and with the preparation of aggregate, the overall process took more than one hour.

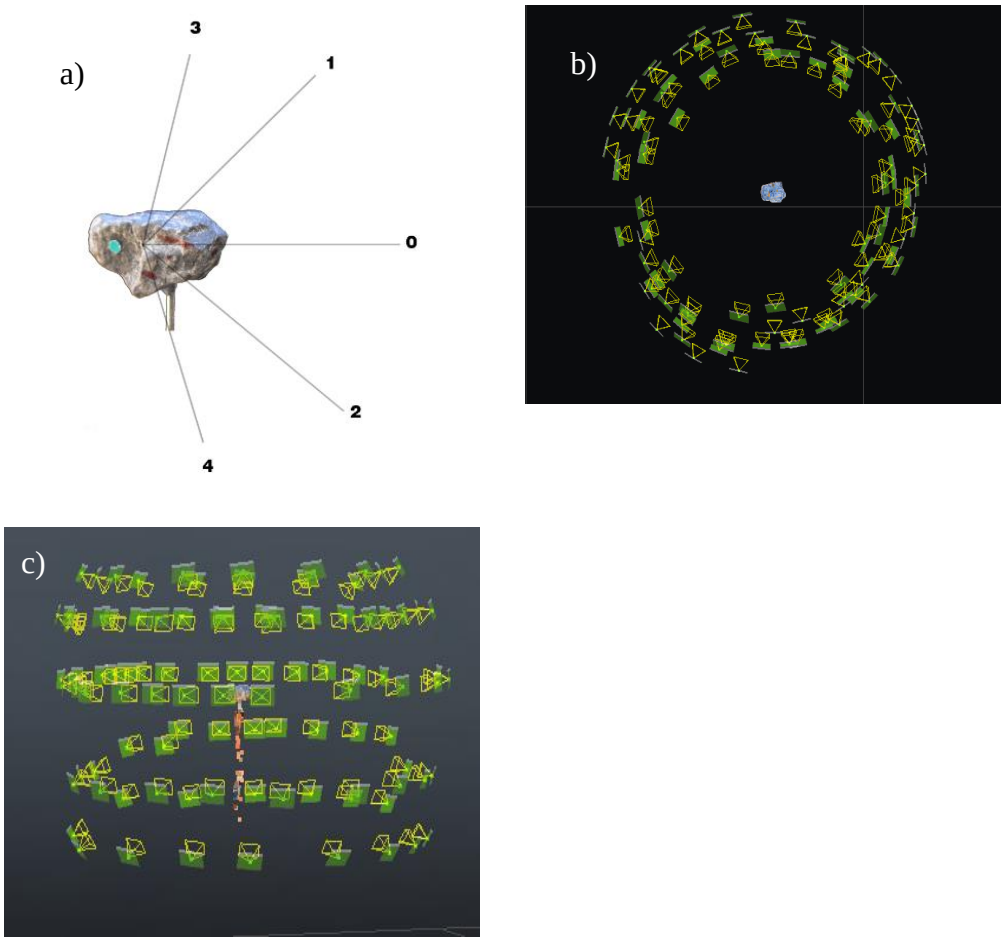

Figure 17 Camera positions a) elevations of camera b) top view of camera positions c) side view of camera positions

3.2.4 Creating 3D Model

In order to obtain a 3D point cloud or 3D mesh of any object, there exists various commercial and free software such as Autodesk ReCap, Elcovision 10 and ContextCapture. In this study, the authors used the educational license of ContextCapture to obtain the 3D models from 2D images.

The ContextCapture software can be used with either images or videos taken by any compact digital, mobile phone, DSLR, or fisheye camera. Although the software does not have minimum pixels requirements, the quality and the extent of the final work depend on the camera resolution. In other words, the high-resolution

camera captures more information than the low-resolution camera. Therefore, more images are required to describe the object in 3D with a low-resolution camera and it will increase the rendering time and also vice versa is true. Moreover, the software supports various digital image formats such as JPEG, TIFF, and PNG as an input. ContextCapture can create 3D models from images that do not have positioning data by using arbitrary position, rotation, and scale of the image. The software works in 64-bit Windows XP/Vista/7/8/10 operating systems and a minimum of 8 GB RAM and 1 GB NVIDIA or AMD graphic cards. [38]

The ContextCapture software is composed of two main modules and both are required. The modules are [38]:

1. **ContextCapture Master**: This module is used for inputting data, editing the process settings, monitoring the rendering process, and visualizing the results.
2. **ContextCapture Engine**: This module works in the background without user interaction. The job of the module is 3D reconstructing or aerotriangulation.

In this research, the properties of the computer, which was used in rendering and analyzing, were:

- 64-bit Windows 10 Education operating system.
- Processor: Intel(R) Core(TM) i7-9750H CPU @ 2.60GHz, 6 Core(s), 12 Logical Processor(s).
- 32.0 GB RAM.
- Intel(R) UHD Graphics 630 and NVIDIA GeForce GTX 1650 graphic cards.

In this study, aggregate photos, captured using a DSLR (Nikon D3400) camera according to the aforementioned procedure in the previous section, were used as input to the ContextCapture. The photos were submitted to the aerotriangulation to determine the location of each image [38]. The aerotriangulation was processed

through ContextCapture Engine. The aerotriangulation process determines the position of the camera for each image as shown in **Figure 18a**. Before reconstructing the 3D model, the region of interest (**Figure 18b**, yellow bounding box) was placed around the aggregate to eliminate the unnecessary parts from the analysis. Then, the 3D model of the aggregate was reconstructed to obtain 3D Mesh in "obj" format. Depending on the number of photos, the production of the 3D mesh took about 20-60 minutes per aggregate. It should be noted that the duration of this process depends on the computer configuration. The output of reconstruction was shown in **Figure 18c** and at this stage, the model was ready for further editing.

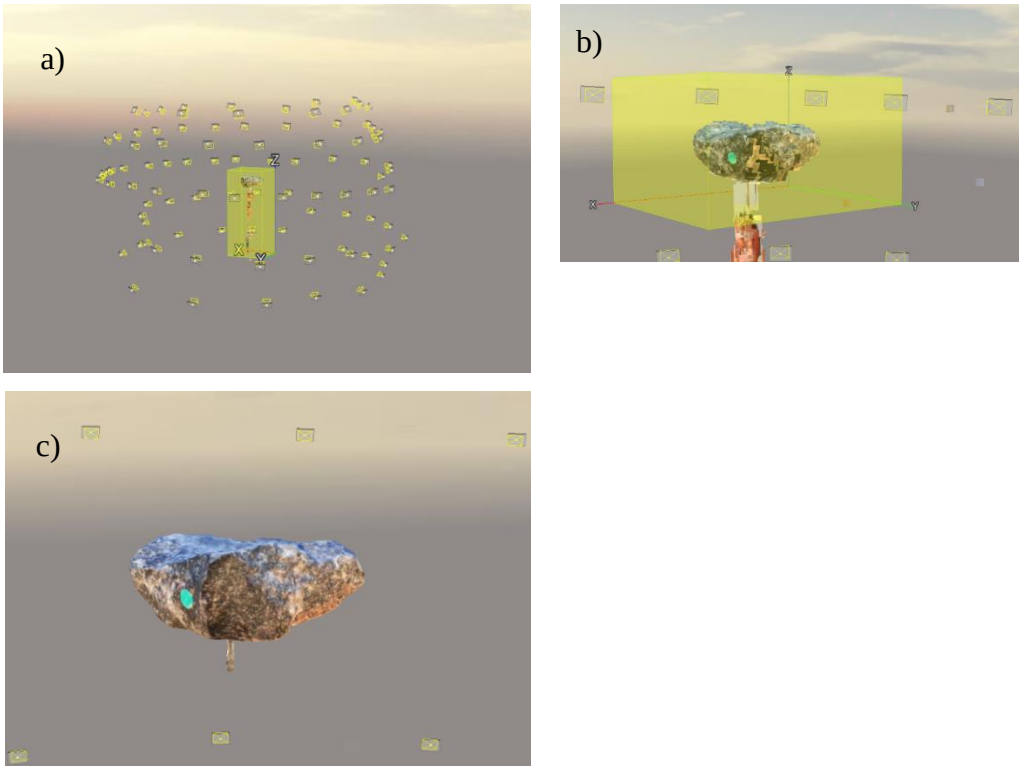

Figure 18 Creating 3D model from 2D images a) the result of aerotriangulation. camera position of each image b) 3D reconstruction region was redefined c) output of 3D reconstruction

3.2.5 Editing 3D Model

There are various free and commercial software available for editing 3D Mesh (i.e. MeshLab, Meshmixer, etc.). Upon these software, Meshmixer is a free software that has numerous features such as remeshing, hole filling, and 3D measuring [39]. Moreover, it has a user-friendly interface. Thus, it was used for editing the 3D aggregate models and measuring dimensions in this study.

The "obj" file, which was extracted from ContextCapture, was imported into Meshmixer (**Figure 19a**) for preparing the aggregate model for MATLAB analysis. Since the focus of the camera was on the aggerate during taking the pictures, the stick used to hold the aggregate was blurry as shown in **Figure 19a**. The stick and glue were removed from the model by using the Meshmixer. Therefore, the hole occurred on the surface of the aggregate as shown in **Figure 19b**. Meshmixer's Inspector tool was used to fill the hole as shown in **Figure 19c**. For all analyzes, this corrected area was approximately 0.5% of the overall surface of the aggregate, which was assumed within the exceptional error limits. The density of the default triangulation of the meshed object is shown in **Figure 19d**. The model can be also under (**Figure 19e**) or over (**Figure 19f**) triangulated by using the meshing tool of the Meshmixer. The true sizes of the aggregate were calculated by using the pixel vise dimensions of the little green circle sticker. The length of multiple approximate diameters of the sticker as shown in **Figure 19g** (lines passing through the approximate center) were measured using the Meshmixer's measuring tool. The average length was recorded to be later used to calculate the true dimensions of the aggregates. The ".ply" (Polygon File Format) file was extracted for default, over and under triangulated 3D mesh of each aggregate. Then, further analyzes were performed using the MATLAB programming language.

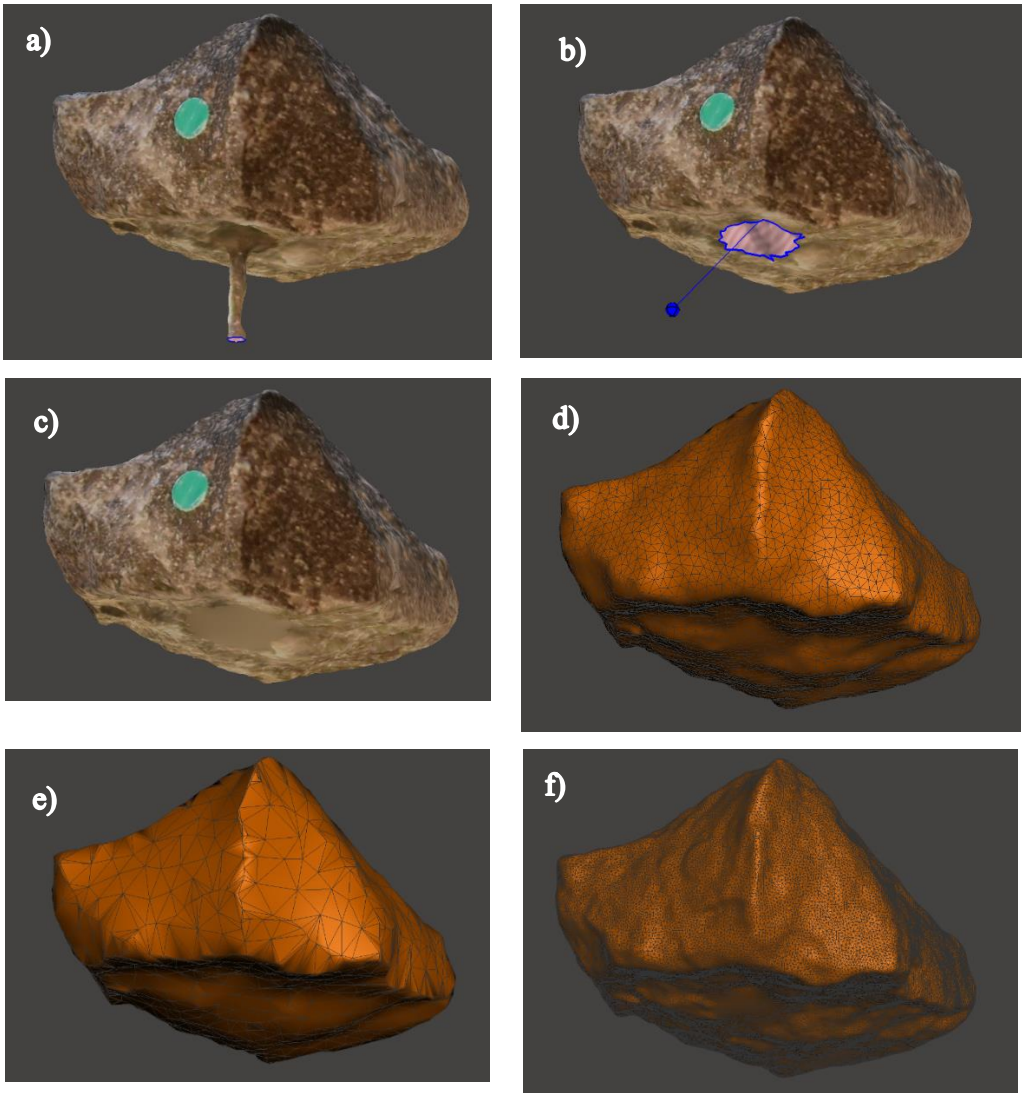

Figure 19 Editing 3D Model of aggregate a) view of the 3D aggregate model in Meshmixer obtained from ContextCapture b) hole on the surface of the aggregate model after removal of stick and glue c) hole filled by using Meshmixer's inspector tool d) triangulation density by default e) under triangulated 3D mesh f) over triangulated 3D mesh g) approximate diameter measure in Meshmixer

Figure 19 (cont'd) Editing 3D Model of aggregate a) view of the 3D aggregate model in Meshmixer obtained from ContextCapture b) hole on the surface of the aggregate model after removal of stick and glue c) hole filled by using Meshmixer's inspector tool d) triangulation density by default e) under triangulated 3D mesh f) over triangulated 3D mesh g) approximate diameter measure in Meshmixer

3.3 2D Imaging

3.3.1 Sample Preparation

Throughout the analysis, it was determined that white-colored parts of the surfaces resulted in some problems in 2D image processing. Since the background color of the aggregates is white while converting the image to black-while (or binary). These white portions were recognized as background. In other words, these parts were seemed to be holes on the surface of the binary images. Therefore, these white-colored portions of the aggregates were painted with colored pencils to represent aggregates correctly on binary images.

3.3.2 Setup

In order capture 2D images of aggregate, same camera and tripod was used as details given in **section 3.2.2**. Since binary image was used in 2D analysis the boundary of the aggregate should be clear. Therefore, lighting box (800W) that reflects the light upward was used.

3.3.3 Photography

The aggregates were placed on a lighting box to ensure clean and white background. In order to keep the aggregate stable in the desired plane, blu-tack was used. The amount of blu-tack should be so that it will keep the aggregate stable and should not be seen in the images of the aggregate. The camera was positioned so that it will capture the aggregate's image from the top and without any shadow around the aggregate. If not, shadows may look like a part of the aggregate in black-white images.

In addition, to detect the aggregate's original size a ruler placed near the aggregate as a reference in the pictures (See **Figure 20b**, **20c** and **20d**). Later, the pixel number corresponding to 1 mm length was used to calculate the true dimensions of the aggregates.

In order to calculate morphological indices and dimensions of the aggregates by using the traditional 2D method, the photos of each aggregate were taken in three different planes (or positions), as follows:

- **Longest Plane**: The aggregate was placed so that it lay on its surface which has the largest area (**Figure 20a** and **20b**).
- **Side Plane**: The aggregate from its longest plane was rotated 90^0 around its approximate major axis (**Figure 20a** and **20c**).
- **Vertical Plane**: The aggregate from its longest plane was rotated 90^0 to the vertical direction (**Figure 20a** and **20d**).

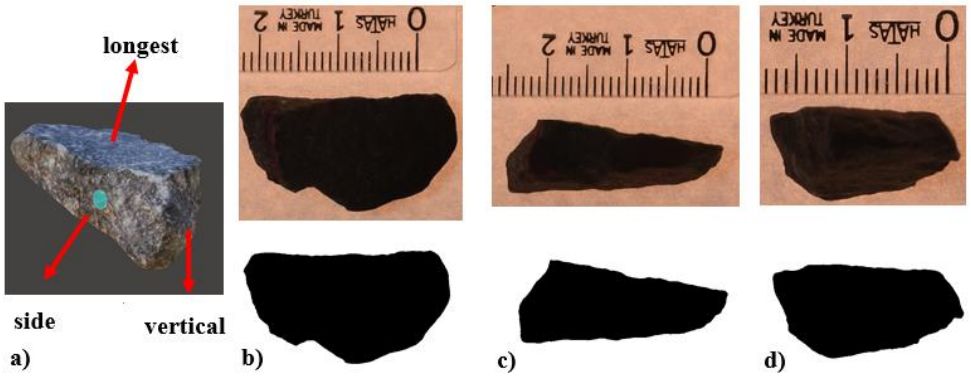

Figure 20 a) 3D model of the aggregate b) longest plane of the aggregate c), side plane of the aggregate, d) vertical of the aggregate (Note: Figures are rescaled.)

In addition, orthogonal binary images of three particles show in Appendix A.

3.3.4 2D Image Editing

To edit the pictures for the 2D approach, ImageJ free lightweight software was used. ImageJ has the ability to edit, analyze, and process TIFF, GIF, JPEG like images [40]. Initially, the number of pixels corresponding to 1 mm of the ruler was measured. Secondly, the photo was cropped in order get rid of unnecessary portions of the background. Then, the RGB image was converted to black-white (binary) image. Finally, the extracted image in TIFF format was analyzed in MATLAB to gather shape features and morphological indices. These steps were repeated for the three pictures taken from three planes of each analyzed aggregate.

3.4 Summary of Chapter

Using 56 aggregates from five different sources each sample fixed on the stick. From five different elevation 360^0 images of the sample capture by using digital camera. ContextCapture software was used to create 3D model from captured images. The stick was removed by using MeshMixer software. Each sample's three

orthogonal images were captured for the 2D approach. The captured images converted to binary images in order to analyze by 2D methods.

CHAPTER 4

THEORIES AND THEIR APPLICATION

This chapter discusses the theories and developed algorithms that were used in the determination of shape features morphological indices for both 2D and 3D methodologies.

4.1 3D Theories

4.1.1 Introduction

The surface of the aggregate was represented by point cloud and triangles in ".ply" document. The Toolbox Graph of MATLAB was used to read the ".ply" file [41]. The toolbox returned vertices and faces lists of the object. The vertices were the Cartesian coordinates of each point in the point cloud. The structure of the i^{th} vertex point was composed of x,y and z coordinates as given in **Eq. 4-1**. The triangles were formed using three vertices and the faces list stored each triangles' vertices index. The structure of j^{th} triangle (**Figure 21**) was composed of m, n and k which were the indices of m^{th}, n^{th}, and k^{th} points as shown in **Eq. 4-2**.

$$P_i = [x_i, y_i, z_i] \quad \text{Eq. 4-1}$$

$$F_j = [m, n, k] \quad \text{Eq. 4-2}$$

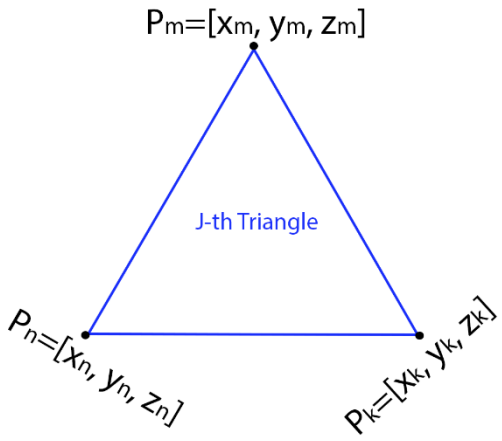

Figure 21 Vertices that represent the j^{th} triangle

4.1.2 Surface Area

The surface area of the aggregate was calculated by summing the area of each triangle on the 3D model as shown in **Eq. 4-3**. The area of each triangle was calculated by dividing the magnitude of the cross product of vectors by two as shown in **Eq. 4-4** [42]. The area of j^{th} triangle was calculated by using the first, second and third vertices obtained from face matrix.

$$A = \sum_{j=1}^{N} A_j \qquad \text{Eq. 4-3}$$

- A: Surface area of aggregate.
- A_j: Area of j^{th} triangle.
- N: Number of total triangles or size of faces list.

$$A_j = \frac{\left|(P_{F_{j2}} - P_{F_{j1}})x(P_{F_{j3}} - P_{F_{j1}})\right|}{2}$$ Eq. 4-4

- F_{j1}: Index pointing to first vertex of j^{th} triangle.
- F_{j2}: Index pointing to second vertex of j^{th} triangle.
- F_{j3}: Index pointing to third vertex of j^{th} triangle.
- $P_{F_{j1}}$: Cartesian coordinates of j^{th} triangle's first vertex.
- $P_{F_{j2}}$: Cartesian coordinates of j^{th} triangle's second vertex.
- $P_{F_{j3}}$: Cartesian coordinates of j^{th} triangle's third vertex.

4.1.3 Volume

The volume of the aggregate, represented by mesh, was calculated by creating tetrahedrons by connecting the surface triangles with the origin (0, 0, 0). The total volume of the mesh was calculated by dividing the sum of the determinant of the tetrahedrons' Jacobian matrix (**Eq. 4-5**) by six as shown in **Eq. 4-6** [43][44]**.** The distance from aggregate to reference point (origin) does not affect the aggregate's total volume, thus any other reference point can be also selected [44]. The determinant of Jacobian matrix has negative and positive values. Thus, the sum of Jacobian determinants independent of the selected reference point gives the same total volume.

$$J_j = \begin{vmatrix} {P_{F_{j1}}}^1 & {P_{F_{j1}}}^2 & {P_{F_{j1}}}^3 & 1 \\ {P_{F_{j2}}}^1 & {P_{F_{j2}}}^2 & {P_{F_{j2}}}^3 & 1 \\ {P_{F_{j3}}}^1 & {P_{F_{j3}}}^2 & {P_{F_{j3}}}^3 & 1 \\ O^1 & O^2 & O^3 & 1 \end{vmatrix}$$ Eq. 4-5

- J_j: Determinant of Jacobian matrix constructed from j^{th} triangle.
- F_{ji}: Index pointing to i^{th} vertex of j^{th} triangle.
- $P_{F_{ji}}$: Cartesian coordinates of j^{th} triangle's i^{th} vertex.
- ${P_{F_{ji}}}^1$: First element or x coordinate of the $P_{F_{ji}}$.

- $P_{F_{ji}}{}^{2}$: Second element or y coordinate of the $P_{F_{ji}}$.
- $P_{F_{ji}}{}^{3}$: Third element or z coordinate of the $P_{F_{ji}}$.
- O^1: Origin's x coordinate or zero.
- O^2: Origin's y coordinate or zero.
- O^3: Origin's z coordinate or zero.

$$V = \frac{1}{6} * \sum_{j=1}^{N} J_j \qquad \text{Eq. 4-6}$$

- V: Total volume of the aggregate.
- N: Number of total triangles or size of faces list.

4.1.4 Centroid of Aggregate

The centroid of the whole aggregate was calculated by dividing the sum of the dot product of centroid of each tetrahedron (**Eq 4-7**) to Jacobian determinant to six times of the total volume of the aggregate [44] as shown in **Eq. 4-8**.

$$C_j = \frac{P_{F_{j1}} + P_{F_{j2}} + P_{F_{j3}} + O}{4} \qquad \text{Eq. 4-7}$$

- C_j: Centroid of tetrahedron constructed from j^{th} triangle
- $P_{F_{ji}}$: Cartesian coordinates of j^{th} triangle's i^{th} vertex.
- O: Origin (0, 0, 0) of the Cartesian Coordinate System.

$$C_{3D} = \frac{\sum_{j=1}^{N} C_j * J_j}{6 * V} \qquad \text{Eq. 4-8}$$

- C_{3D}: Centroid coordinates of the 3D mesh (aggregate).
- J_j: Determinant of Jacobian matrix constructed from j^{th} triangle.
- N: Number of total triangles.
- V: Total volume of the aggregate.

4.1.5 Ray Triangle Intersection

The ray triangle intersection algorithm was used to determine the intersection point of line with a triangle [45]. According to the pseudo-code written by Möller and Trumbore, the algorithm was rewritten in MATLAB to determine radii or diameters of the aggregate for any arbitrary angle. Rather than approximating the aggregate as a box by using the boundary box, it is possible to calculate the dimensions without approximating the whole shape of the object utilizing this algorithm. The mesh surface of the aggregate composed of triangles and any radius was triggered as a ray by giving its elongation direction. All triangles were checked for the specific ray until the one of triangles responded to the intersection algorithm as shown in **Figure 22**.

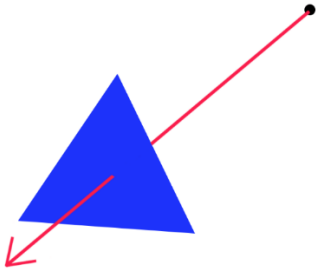

Figure 22 The ray intersected with triangle

4.1.6 Ellipsoidal to Cartesian Coordinates

In order to generate radii at any desired angle, the conversion of the ellipsoidal coordinate system to the Cartesian coordinate system was essential. The radius of the ellipsoid starts from the origin (0,0,0), which is the centroid of the ellipsoid, and ends at the point where it cuts/touches the surface of the ellipsoid. The starting point of the ellipsoid's i^{th} radius is always known and the end point's coordinates was calculated by using **Eq. 4-9**. The a_{3D}, b_{3D} and c_{3D} are the semi-axes lengths of the ellipsoid and these lengths were kept constant while calculating the radii's

coordinates. The ϕ and θ variables are the azimuthal angles and define the direction of each radius as shown in **Figure 23a**. Each radius was calculated from identical ϕ and θ.

$$x_i = a_{3D} * \cos\theta * \sin\phi \qquad \text{Eq. 4-9}$$
$$y_i = b_{3D} * \sin\theta * \cos\phi$$
$$z_i = c_{3D} * \cos\phi$$
$$0 \leq \theta < 360^0$$
$$0 \leq \phi \leq 180^0$$

- x_i, y_i, z_i: Cartesian coordinates of i^{th} radius.
- a_{3D}, b_{3D}, c_{3D}: Principal semi-axes of the ellipsoid.
- θ, ϕ: Azimuthal angles.

When ϕ was constant and θ was incrementally changed between $[0^0, 360^0)$ contour like or horizontal ellipse like radii sequence was generated as shown in **Figure 23a, line a**. On the other hand, when θ was constant and ϕ was changed incrementally between $[0^0, 180^0]$ the radii points' position was like vertical apple slices or crescent **Figure 23a, line b**. Ellipse (horizontal) and slice (vertical) like positions of radii play a crucial role in form index calculation which will be discussed further in section 4.1.9.

The azimuthal ϕ and θ degrees were started with 0^0 and were increased by $\Delta\phi$ and $\Delta\theta$ respectively to detect the radii's end coordinates. The increments should be so that the position and number of radii sequences (ellipse and slice) will be symmetrical. For instance, the position and number of horizontal/ellipse radii are symmetrical in **Figure 23b**. Otherwise, calculated form or angularity indices will not represent the aggregate's shape uniformly. Therefore, the modulo of ϕ by $\Delta\phi$ and θ by $\Delta\theta$ should be equal to zero. Also, $\Delta\phi$ should be smaller or equal to 90^0 and $\Delta\theta$ should be equal or smaller than 180^0. These conditions are crucial to use radii that are symmetrically positioned. For instance, if $\Delta\theta = 270^0$ the first radius will be at $\theta = 0^0$, the second will be at $\theta = 270^0$ which disturbs the symmetry. On

the other hand, for the analysis in this study, the angle increments were determined significantly small and futher discussed in Chapter 5 (Results and Discussions).

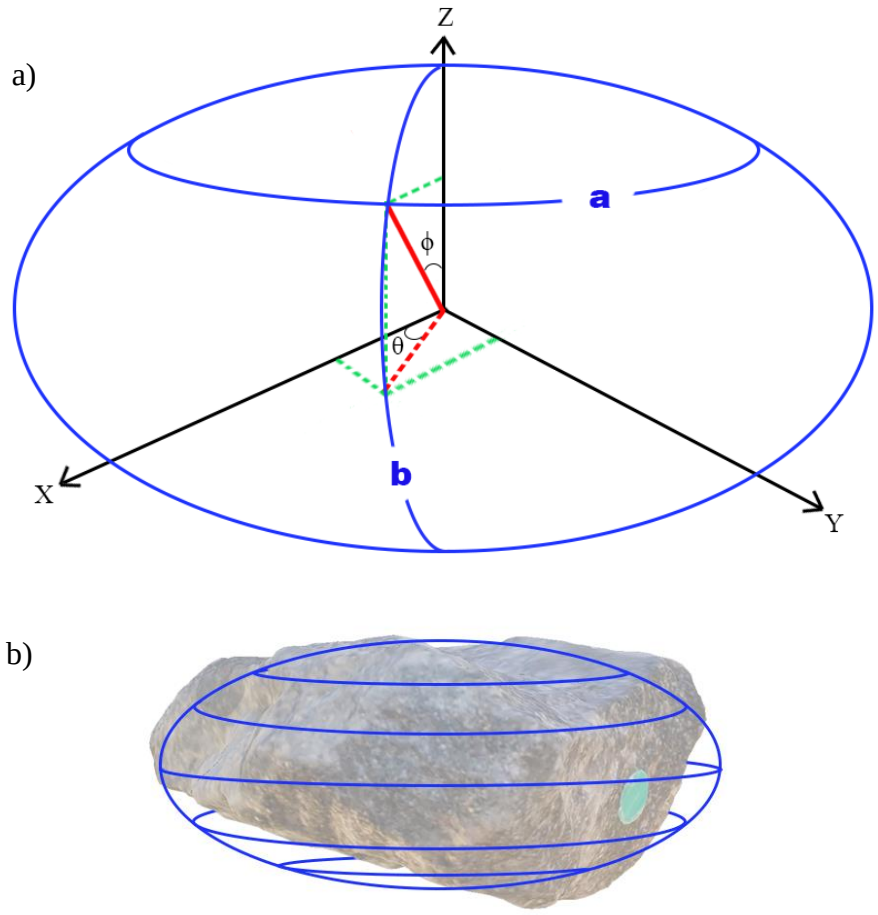

Figure 23 Ellipsoid a) radius at Azimuthal angles b) ellipse slices inside the ellipsoid

The number of total radii was calculated by using the **Eq. 4-10.** The end coordinates of radii at polar points of the ellipsoid, where $\phi = 0^0$ and $\phi = 180^0$, are the same. Therefore, the same radiuses calculated due to rotation should be eliminated. Therefore, the -1 value in the term $\left(\frac{180^0}{\Delta\phi} - 1\right)$ comes from the elimination of polar points and the number of the slice like positions are considered

by $\left(\frac{360^0}{\Delta\theta}\right)$. Finally, the $+2$ term in **Eq. 4-10** comes from considering the polar ellipses as two points.

$$N_{radii} = \left(\frac{180^0}{\Delta\phi} - 1\right) * \frac{360^0}{\Delta\theta} + 2 \qquad \text{Eq. 4-10}$$

$$180^0 \; mod \; \Delta\phi = 0$$

$$0 < \Delta\phi \leq 90^0$$

$$360^0 \; mod \; \Delta\theta = 0$$

$$0 < \Delta\theta \leq 180^0$$

- N_{radii}: Number of radii.
- $\Delta\theta, \Delta\phi$: Azimuthal angle increments.

Using the **Eq. 4-9** equation, the ellipsoidal coordinates of the sphere can be also calculated by assuming the semi-axes $(a = b = c)$ equal. Conversion from Cartesian to spherical coordinate system was essential to detect the aggregate's radii coordinates to calculate form index and conversion from Cartesian to ellipsoid coordinate is used to calculate the angularity index, further discussed in the following.

4.1.7 Rotation and Displacement of Coordinates

While calculating the angularity and form indices, the location and orientation of the aggregate were changed. Since these indices are very sensitive to the orientation of the aggregate and will be discussed later in detail. Thus, the vertices matrix was rotated by using the MALTAB's file exchange function [46]. The rotation function rotates the aggregate by pinning the origin of the Cartesian Coordinate System. If the aggregate's centroid is not shifted to the origin, the function will both rotate and displace the aggregate as shown in **Figure 24a and 24b**. Thus, rotating the aggregate without moving the centroid to the origin will pose it at a false location and orientation. Therefore, the centroid of aggregate was placed to Cartesian Coordinate System's origin as shown in **Figure 25a**. For this

purpose, the calculated centroid coordinates (C_{3D}) were subtracted from coordinates of vertices. Then the aggregate rotated along its centroid as shown in **Figure 25a and 25b**.

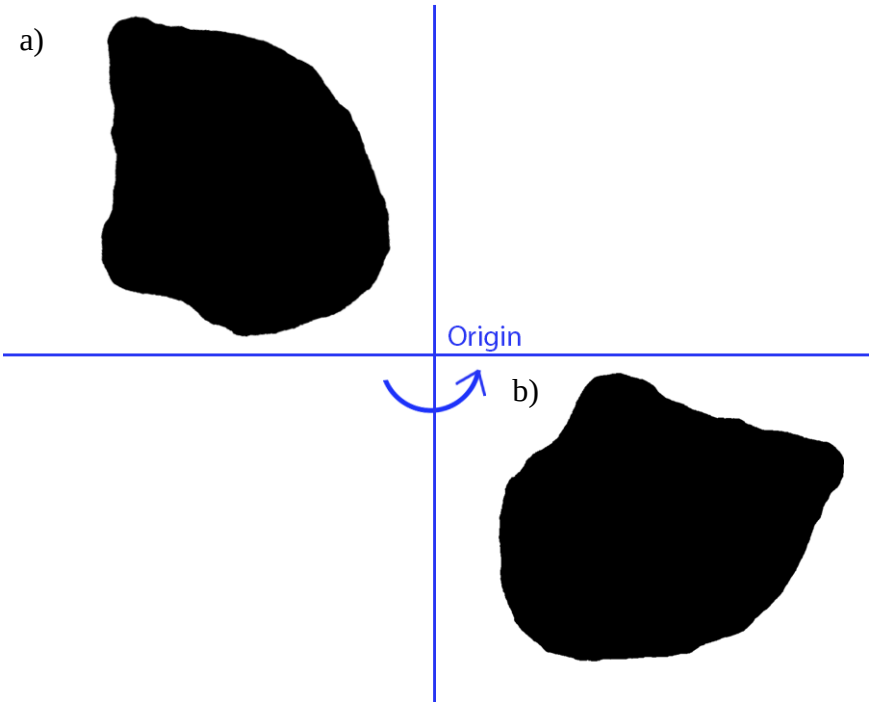

Figure 24 Aggregate rotated and displaced when its centroid is not at origin. a) initial position of aggregate b) rotated and displaced aggregate

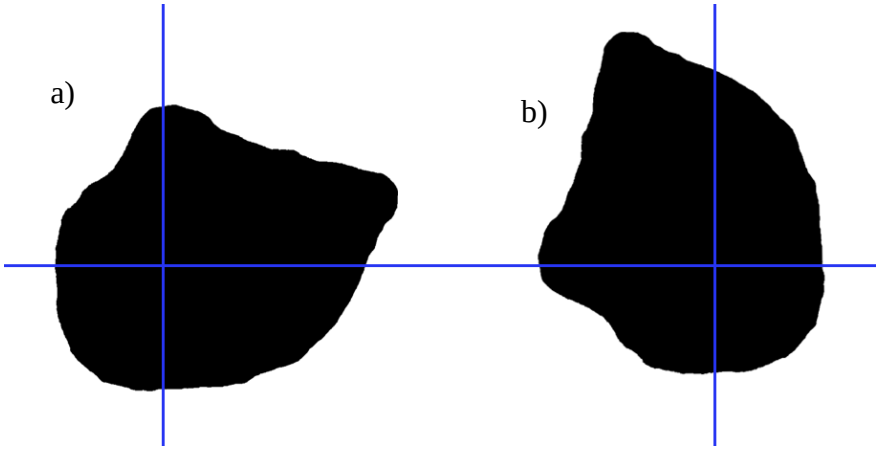

Figure 25 Aggregate rotated when its centroid at origin. a) initial position of aggregate b) rotated aggregate

4.1.8 Angularity Index

Angularity index (AI) is a measure of deviations at the surface of the aggregate and measures the difference of radii of the aggregate and corresponding ellipsoid [47]. The angularity index of 3D object (AI_{3D}) was calculated by summing the magnitude of the difference of aggregate's radius and equivalent ellipsoid radius and dividing by equivalent ellipsoid radius at given angles. The formulation given at **Eq. 4-11** calculates the AI_{3D} by summing the differences at angles θ and ϕ. The difference in the original shape and ellipsoid depends on the true and its equivalent ellipsoid radii. In other words, the difference measure is not affected by the next or previous radii as Form Index (FI). As a result, AI_{3D} is independent from the orientation (ellipse or slice positioned) of radii throughout the analysis. However, AI_{3D} is affected from $\Delta\theta$ and $\Delta\phi$ increments' values. The value of AI_{3D} increases when the angle increments ($\Delta\theta$ and $\Delta\phi$) get smaller since the number of radii increases. Therefore, Normalized 3D Angularity Index (NAI_{3D}) is proposed, **Eq. 4-12,** to make the angularity index independent from the value of angle increments [48]. The NAI_{3D} calculated by dividing the AI_{3D} by the number of radii generated from ellipsoid to Cartesian conversion (**Eq. 4-10**).

$$AI_{3D} = \sum_{\substack{\phi=0^0 \\ Step=\Delta\phi}}^{180^0} \sum_{\substack{\theta=0^0 \\ Step=\Delta\theta}}^{360^0-\Delta\theta} \frac{|R(\phi,\theta) - R_{EE}(\phi,\theta)|}{R_{EE}(\phi,\theta)} \qquad \text{Eq. 4-11}$$

- AI_{3D}: 3D Angularity Index.
- $R(\phi,\theta)$: Length of radius of the aggregate (3D model) at θ and ϕ angles.
- $R_{EE}(\phi,\theta)$: Length of equivalent ellipsoid radius at θ and ϕ angles.
- $\Delta\theta, \Delta\phi$: Angle increments.
- θ, ϕ: Azimuthal angles.

$$NAI_{3D} = \frac{AI_{3D}}{N_{radii}} \quad \text{Eq. 4-12}$$

- NAI_{3D}: Normalized 3D Angularity Index.
- N_{radii}: Number of radii generated by using ellipsoid to Cartesian conversion.

4.1.9 Form Index

Form Index (FI) measures aggregate's variations in the proportions [2], [17]. The 3D Form Index (FI_{3D}) calculated by taking the difference in the radius of θ, ϕ angles (initial radius) and $\theta, \phi + \Delta\phi$ (consecutive radius) and then the difference divided by the length of initial radius as shown in **Eq. 4-13**. The FI_{3D} of the aggregates was calculated by choosing the next radius from apple slice like position (θ is constant and ϕ is changing) as shown in **Figure 26a**. If consecutive radius is chosen from ellipse like position (ϕ is constant and θ is changing) as shown in **Figure 26b**, the differences close to polar points ($\theta = 0^0, \phi = 0^0$) will be very small. On the other hand, the difference of the initial and consecutive radius will be very large near mid ($\phi = 45^0$) of the aggregate. In other words, getting closer to the mid of aggregate as shown in **Figure 26c,** radii differences will increase. Thus, the differences closer to the mid of the aggregate will dominate the FI_{3D} and the differences near-polar point will be ignored. Therefore, FI_{3D} calculated from ellipse like posed radii will not represent the whole aggregate's variations.

$$FI_{3D} = \sum_{\substack{\theta=0^0 \\ Step=\Delta\theta}}^{360^0-\Delta\theta} \sum_{\substack{\phi=0^0 \\ Step=\Delta\phi}}^{180^0-\Delta\phi} \frac{|R(\theta,\phi+\Delta\phi) - R(\theta,\phi)|}{R(\theta,\phi)}$$ Eq. 4-13

- FI_{3D}: 3D Form Index of aggregate.
- $R(\theta,\phi)$: Length of aggregate's radius at θ,ϕ angles or current radius.
- $R(\theta,\phi+\Delta\phi)$: Length of aggregate's radius at $\theta,\phi+\Delta\phi$ angles or next radius.
- $\Delta\theta,\Delta\phi$: Angle increments.
- θ,ϕ: Azimuthal angles.

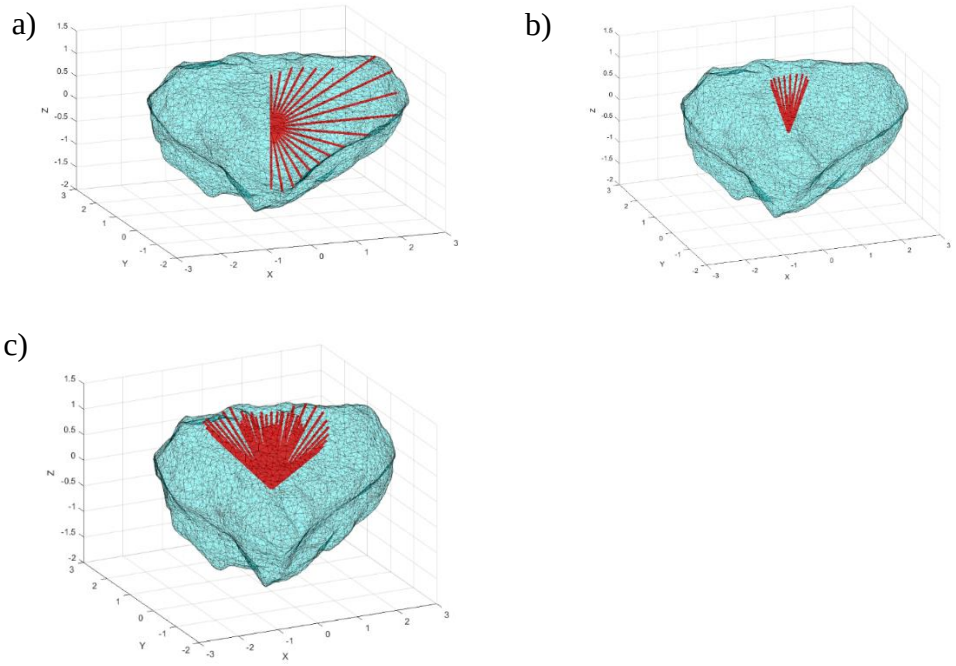

Figure 26 Radii orientations a) single slice like radii orientation in order to calculate form index b) single ellipse like radii orientation c) multiple ellipse like radii orientation

Since FI is calculated by using the length of initial and consecutive radii, the distance to the consecutive radii is important. Different $\Delta\theta$ and $\Delta\phi$ results in different FI_{3D} values for the same aggregate. Therefore, Normalized Form Index for the 3D object (NFI_{3D}) was calculated as in **Eq. 4-14** to make the FI

independent from increments up to some degree. NFI_{3D} is calculated by dividing FI_{3D} value by the square root of the number of radii of the aggregate [48].

$$NFI_{3D} = \frac{FI_{3D}}{\sqrt{N_{radii}}} \quad \text{Eq. 4-14}$$

- NFI_{3D}: Normalized Form Index of aggregate.
- N_{radii}: Number of radii of aggregate generated by using spherical to Cartesian conversion.

4.2 2D Theories

4.2.1 Angularity Index

In order to calculate the 2D angularity index, it is essential to find the difference of each radius of aggregate located at θ and equivalent ellipse radius. In order to generate equivalent ellipse radii length, **Eq. 4-15** [49] was used.

$$R_{EE}(\theta) = \frac{a_{2D} * b_{2D}}{\sqrt{{a_{2D}}^2 * (\sin\theta)^2 + {b_{2D}}^2 * (\cos\theta)^2}} \quad \text{Eq. 4-15}$$

- $R_{EE}(\theta)$: Radius of the ellipse, draw on aggregate, at θ angle.
- θ: Azimuthal angle varies between 0 and 360^0.
- a_{2D}, b_{2D}: Semi-axes of the ellipse.

The Angularity Index of 2D object (AI_{2D}) calculated by summing the differences of aggregate's radius and equivalent ellipse radius at θ angle as shown in **Eq. 4-16** [47]**.** The θ starts from 0^0 and is increased by $\Delta\theta$ degree until 360^0.

$$AI_{2D} = \sum_{\substack{\theta=0^0 \\ Step=\Delta\theta}}^{360^0-\Delta\theta} \frac{|R(\theta) - R_{EE}(\theta)|}{R_{EE}(\theta)} \quad \text{Eq. 4-16}$$

- AI_{2D}: 2D Angularity Index.

- $R(\theta)$: Length of radius of aggregate (2D image) at θ angle.
- $R_{EE}(\theta)$: Length of equivalent ellipse at θ angle.

Angularity Index was calculated for three orthogonal images of aggregate. In order to calculate angularity index for whole aggregate the weighted average of AI (AI_{2D}^{avg}) the equation at **Eq. 4-17** [50] was used.

$$AI_{2D}^{avg} = \frac{A_{longest} * AI_{2D}^{longest} + A_{side} * AI_{2D}^{side} + A_{vertical} * AI_{2D}^{vertical}}{A_{longest} + A_{side} + A_{vertical}} \quad \text{Eq. 4-17}$$

- AI_{2D}^{avg}: Form index obtained from weighted averaging.
- $A_{longest}$, A_{side}, $A_{vertical}$: Area of white pixels (aggregate) obtained from **longest**, **side** and **vertical** positions of each aggregate.
- $AI_{2D}^{longest}$, AI_{2D}^{side},$AI_{2D}^{vertical}$: 2D angularity index values obtained from **longest**, **side** and **vertical** positions of each aggregate

4.2.2 Form Index

The form index of 2D object (FI_{2D}) calculated by summing the differences of aggregate's current radius and next radius at θ angle as shown in **Eq. 4-18** [47]**.** The θ starts from 0^0 and is increased by $\Delta\theta$ degree until 360^0.

$$FI_{2D} = \sum_{\substack{\theta=0^0 \\ Step=\Delta\theta}}^{360^0-\Delta\theta} \frac{|R(\theta) - R(\theta+\Delta\theta)|}{R(\theta)} \quad \text{Eq. 4-18}$$

- FI_{2D}: 2D Form Index.
- $R(\theta)$: Length of radius of aggregate (2D image) at θ angle.
- $R(\theta+\Delta\theta)$: Length of radius at $(\theta+\Delta\theta)$ angle.

Form Index was calculated for three orthogonal images of aggregate. In order to calculate form index for whole aggregate, weighted average of FI (FI_{2D}^{avg}), the equation at **Eq. 4-19** [50] was used.

$$FI_{2D}^{avg} = \frac{A_{longest} * FI_{2D}^{longest} + A_{side} * FI_{2D}^{side} + A_{vertical} * FI_{2D}^{vertical}}{A_{longest} + A_{side} + A_{vertical}} \quad \text{Eq. 4-19}$$

- FI_{2D}^{avg}: Form index obtained from weighted averaging.
- $A_{longest}$, A_{side}, $A_{vertical}$: Area of white pixels (aggregate) obtained from **longest**, **side** and **vertical** positions of each aggregate.
- $FI_{2D}^{longest}$, FI_{2D}^{side}, $FI_{2D}^{vertical}$: 2D form index values obtained from **longest**, **side** and **vertical** positions of each aggregate

4.3 Application of 3D Algorithms

As discussed in the previous sections in detail, the Toolbox Graph framework [41] of MATLAB was used to extract vertices and faces of the object from the ".ply" file. Accordingly, the shape features and morphological indices of coarse aggregates were calculated by using vertices and faces lists.

4.3.1 Shape Features

The area and volume of the aggregate were calculated as explained in section 4.1.2 and 4.1.3. The area ($unit^2$) and volume ($unit^3$) units are converted to mm^2 and mm^3 respectively by using the diameter length of the green circle on the aggregate's surface (**Figure 19g**). The $unit$ based and true diameter lengths of the circle were measured by using Meshmixer and the digital caliper, respectively.

Then, the centroid of aggregate was calculated as in section 4.1.4. In order to shift the centroid of aggregate (C_{3D}) to Cartesian coordinate system's origin, the calculated centroid subtracted from point cloud (or vertices) coordinates of the aggregate. After this stage of the 3D mesh will equal to origin of the Cartesian coordinate system ($C_{3D} = (0, 0, 0)$).

The diameter of the aggregate is the dimension that starting from the surface of the aggregate and passing from the centroid elongated up to the other side as shown in **Figure 27**. Aggregate's longest diameter (L_{3D}) is the shape feature that was used in rotation. In order to find the aggregate's longest diameter (L_{3D}), point cloud data and ray triangle intersection algorithm was used. Aggregate's longest diameter's starting point cannot be on the surface of triangles (surface of mesh represented by triangles) and it is one of the vertices. On the other hand, longest diameter's end point (where touches other side) may be intersect the face of the triangle or one of its vertices. Consequently, all points in the point cloud was checked whether it is creating the longest dimension or not. Each point (start coordinate) treated as a ray in the direction of centroid (C_{3D}) and using the ray triangle intersection algorithm (section 4.1.5) the end point of each diameter was detected as shown in **Figure 27**. The length from the start coordinate (any vertex) to the end coordinate was measured for each diameter and the maximum diameter was chosen as the longest length (L_{3D}).

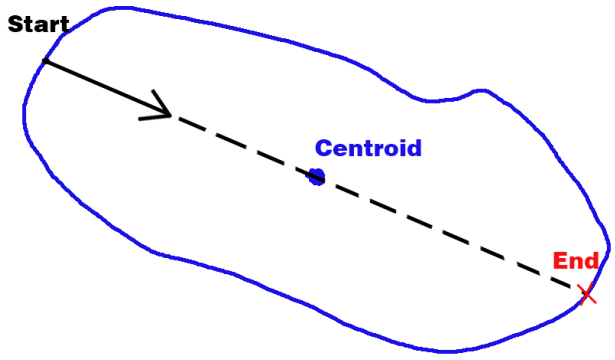

Figure 27 Diameter

In order to generalize the position of the model of the aggregate, it was rotated. After finding the longest diameter, the mesh model was rotated as discussed in section 4.1.7 so that the longest diameter will lie on the x-axis. This rotation was illustrated: the position of the L_{3D} and its target destination as shown **Figure 28a**. After rotation, the longest diameter and x-axis was matched as shown in **Figure 28b**.

a)

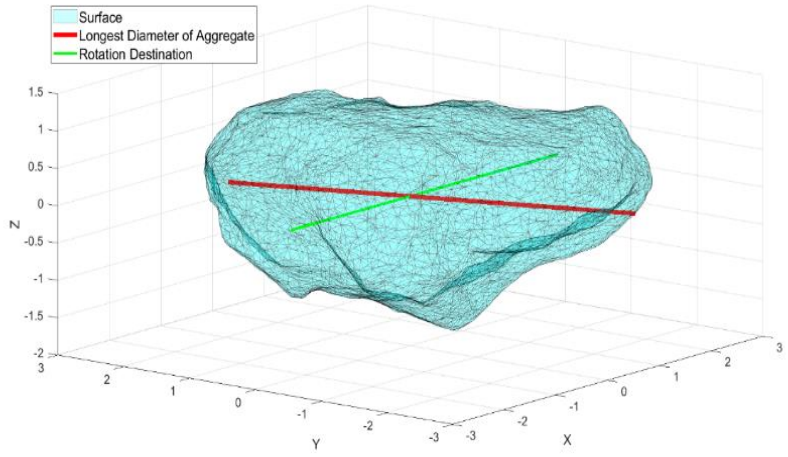

b)

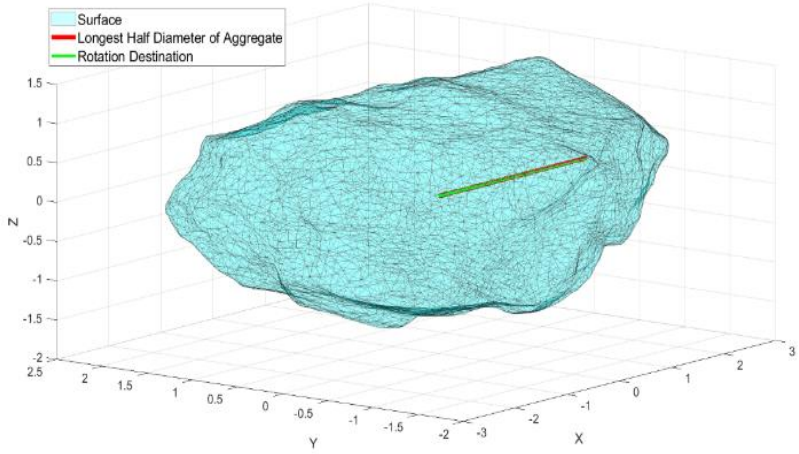

Figure 28 Rotation of aggregate's longest diameter a) longest diameter and its rotation destination (x axis) b) longest diameter lies on the x-axis

After rotating the aggregate's longest diameter to the x-axis, the aggregate completely was fixed by rotating its perpendicular shortest diameter (T_{3D}) to the z-axis. T_{3D} is the diameter that is perpendicular to the x-axis. The perpendicular shortest diameter was calculated by obtaining perpendicular diameters by using spherical to Cartesian coordinate system conversion and ray triangle intersection algorithms. To find the perpendicular shortest diameter, the following steps were used:

1. Unity radii points' ($a_{3D} = b_{3D} = c_{3D} = 1\,unit$) coordinates were calculated by choosing $\Delta\phi = 1^0$ and $\Delta\theta = 90^0$. Points calculated at this stage positioned like two rings which were parallel to the x-axis and perpendicular to the x-axis (**Figure 29a**).
2. In order to find the perpendicular smallest diameter, the parallel ring elements were deleted as shown in **Figure 29b**.
3. Unity radii were created by connecting C_{3D} (centroid of aggregate) and each ring element as shown in **Figure 29c**. These radii were assumed to be rays starting from the centroid toward each unity point (ring element).
4. Each ray extended or shortened (if distance to surface shorter than 1 unit) up to the surface of the aggregate and perpendicular radii were obtained (**Figure 29d**). The intersection points of the ray with the surface of aggregate are shown in **Figure 29e**.
5. Perpendicular radii combined so that diameters were obtained. For instance, the radius at $\phi = 0^0$, $\theta = 0^0$ created diameter with the radius at $\phi = 180^0$, $\theta = 0^0$.
6. Among perpendicular diameters, the shortest perpendicular diameter (T_{3D}) was obtained.

a)

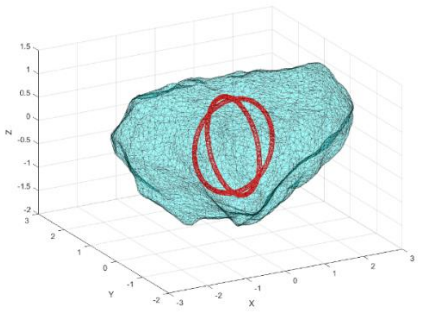

b)

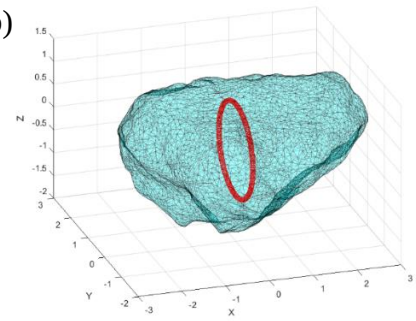

Figure 29 Generating perpendicular radii a) raw ring points; parallel ring and perpendicular ring b) after deletion of parallel ring c) unity radii perpendicular to x-axis d) radii perpendicular to x-axis. (unity radii extended/shorted up to surface of aggregate) e) intersection points of extended radii with the surface of aggregate

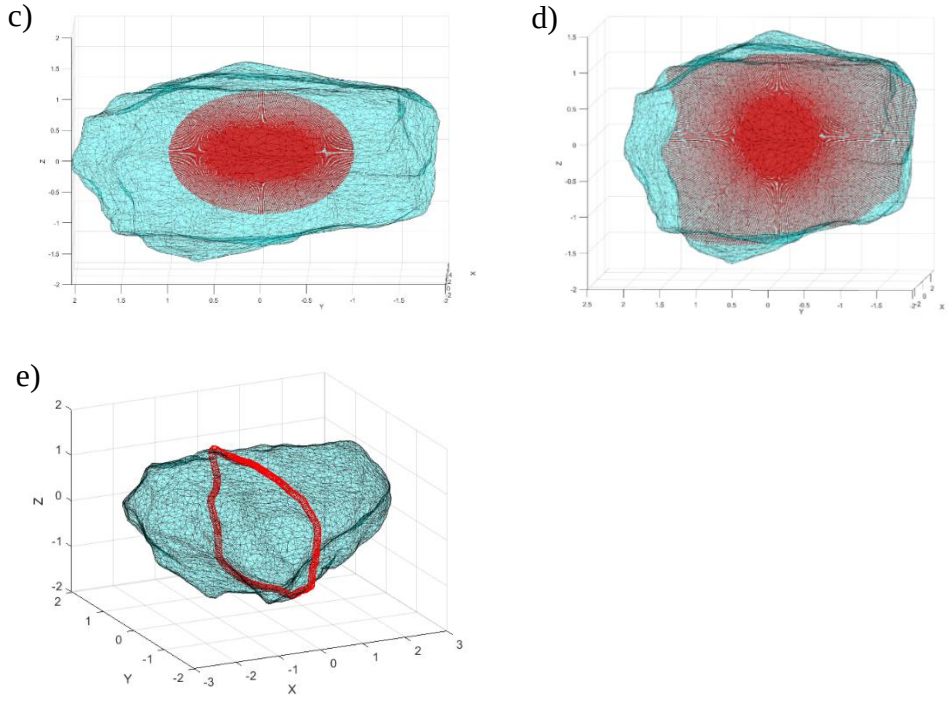

Figure 29 (cont'd) Generating perpendicular radii a) raw ring points; parallel ring and perpendicular ring b) after deletion of parallel ring c) unity radii perpendicular to x-axis d) radii perpendicular to x-axis. (unity radii extended/shorted up to surface of aggregate) e) intersection points of extended radii with the surface of aggregate

Point cloud data (vertices list) cannot be directly used in finding the overall shortest (S_{3D}) and mean (M_{3D}) diameters. As shown in **Figure 30,** the edges of the triangle were assumed to be vertices and distance from C_{3D} to vertices (**dotted lines**) may not be the shortest distance. S_{3D} may be the distance from C_{3D} to some point which is on the surface (**solid line**) of the triangle. Similarly, (M_{3D}) should not be calculated from vertices data since point cloud may not represent aggregate's whole surface. The point cloud may contain more points where aggregate is angular but less data may be available for smoother surface. The overall mean diameter may be dominated by locations where diameters were generated from high densely located points. In order to calculate morphological indices and shape features independent from point distribution uniformity, the radii were created artificially by using spherical to Cartesian conversion and ray triangle intersection algorithms.

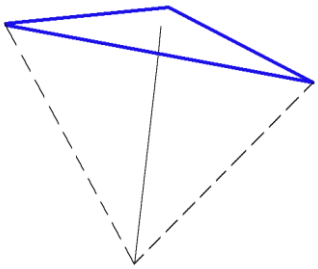

Figure 30 Distance to the face and vertices of triangle

Steps in order to generate artificial radii as follows:

1. Unity radii points' ($a_{3D} = b_{3D} = c_{3D} = 1\ unit$) coordinates were generated for $\Delta\phi$ and $\Delta\theta$ degree increments that were chosen by the user as shown in **Figure 31a**.
2. The generated unity radii extended or shortened to the surface of aggregate by using the ray triangle intersection algorithm as shown in **Figure 31b**.
3. Diameters were generated by matching the gendered radii according to their θ and ϕ values.
4. Overall shortest diameter (S_{3D}) was obtained from the minimum length among the diameters.
5. The average length of the diameters was assumed to be overall mean diameter (M_{3D}) of the aggregate.

a) b)

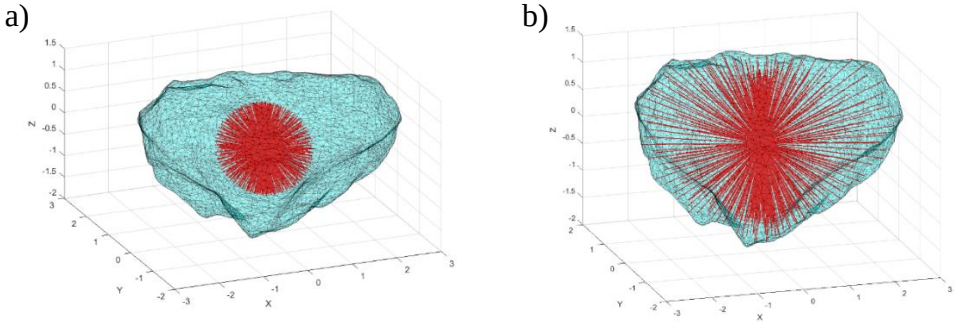

Figure 31 Generation of artificial radii a) unity radii generated by $\Delta\phi$ and $\Delta\theta$ degree increments b) unity radii extended/shortened up to the surface of aggregate

4.3.2 Angularity Index

Angularity index was calculated from the difference of aggregate's radii and equivalent ellipsoid radii. Differently than previous study [48], in this thesis the ellipsoid generated by using shortest diameter of aggregate and both studies' ellipsoid generating method will be introduced in this section.

In order to generate the imaginary ellipsoid around the aggregate, it was assumed that ellipsoids' longest semi-axis was equal to the longest diameter of aggregate ($a_{3D} = \frac{L_{3D}}{2}$). On the other hand, other semi-axes were determined as follows:

- **Ellipsoid by smallest**: Other semi-axes of the ellipsoid was assumed to be equal to the overall shortest half diameter ($b_{3D} = c_{3D} = \frac{S_{3D}}{2}$).
- **Ellipsoid by mean**: Other semi-axes of the ellipsoid was assumed to be equal to overall mean half diameter ($b_{3D} = c_{3D} = \frac{M_{3D}}{2}$).

The results with the assumption of **ellipsoid by mean** was presented in the previous study [48]. In this thesis, the details of the **ellipsoid by smallest** were introduced to improve the correlation between 3D and 2D methods.

If the angularity index was calculated before rotating with respect to the longest diameter, the ellipsoid would be differently positioned for each aggregate. In other words, the longest diameter of the ellipsoid and longest diameter of the aggregate would be mismatched as shown in **Figure 32a**. After fixing the aggregate and ellipsoid longest diameters should lie on the x-axis as shown in **Figure 32b**.

a) b)

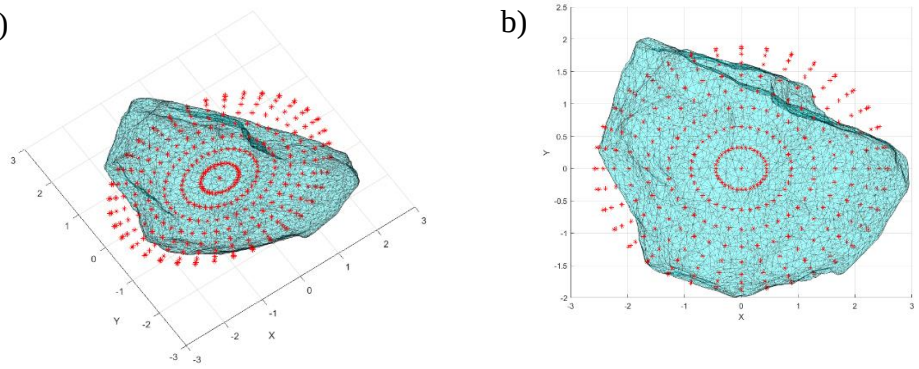

Figure 32 Ellipsoid and aggregate's positions a) ellipsoid radii generated before rotation of aggregate b) ellipsoid radii generated after rotation of aggregate (longest diameters of ellipsoid and aggregate lie on the x-axis)

In order to calculate AI_{3D}, ellipsoidal to Cartesian conversion and ray triangle intersection algorithms were used. The radii of aggregate and equivalent ellipsoid were generated artificially as listed below:

1. The ellipsoid radii were generated by using semi-axes values for $\Delta\phi$ and $\Delta\theta$ angle increments (by ellipse like manner) as shown in **Figure 33a**.
2. Then ellipsoid radii were extended or shorted to the surface of aggregate in order to obtain equivalent aggregate radii.

Both ellipsoid and equivalent aggregate radii were shown in **Figure 33b** by red and black lines, respectively. Recording each aggregate radius and equivalent ellipsoid radius, AI_{3D} and NAI_{3D} were calculated as explained in section 4.1.8.

a) b)

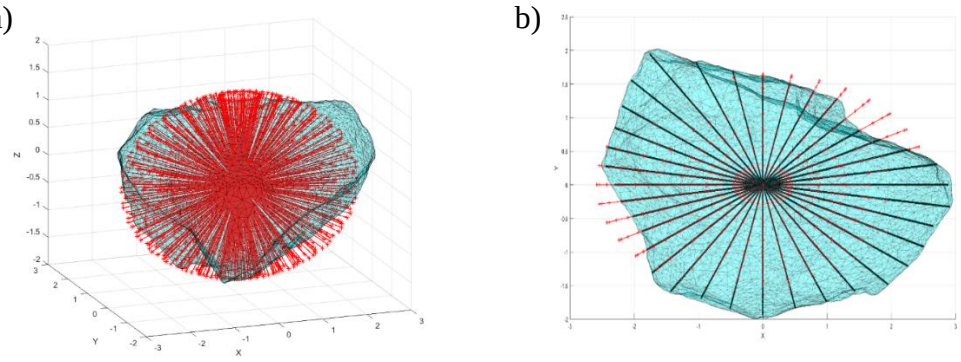

Figure 33 Radii of ellipsoid and aggregate a) radii of ellipsoid b) radii of ellipsoid (red) and aggregate (black)

4.3.3 Form Index

In 3D form index calculations, it is important to define initial and consecutive radii. Firstly, unity radii were generated by using spherical to Cartesian conversion algorithm for $\Delta\phi$ and $\Delta\theta$ angle increments. Secondly, unity radii were extended or shortened to the surface of aggregate by using ray triangle intersection algorithm. Lastly, as explained in section 4.1.9, initial and consecutive radii were determined by using slice (crescent) like manner.

FI_{3D} was calculated for three different position of aggregate. In previous study [48], the 3D form index calculated after rotating the aggregate's longest diameter to x-axis. In order to improve 2D and 3D form index correlations this thesis introduces 3D form indices with new positions. It should be noted that the position of the aggregate plays a crucial role in the correlation between 2D and 3D FI. The positions were summarized as follows:

- **Free z position**: The longest diameter was fixed on the x-axis but the aggregate position around the x-axis was assumed to be free. In other words, the T_{3D} was not fixed to the z-axis.
- **Shortest to z position**: The longest axis was similarly fixed on the x-axis, and the perpendicular shortest length was fixed to the z-axis. It was

assumed that the initial radius was always starting from T_{3D} for each crescent line.

- **Longest to z position**: The longest diameter was fixed on the z-axis. On the other hand, T_{3D} was fixed to the x-axis. It was assumed that the initial radius was always starting from L_{3D} for each crescent.

In previous research [48] only **free z** position was used to calculate 3D form index. On the other hand, this thesis calculates FI_{3D} according to aggregate's **shortest to z** and **longest to z** positions. Aggregate oriented to **shortest to z** position as explained in section 4.3.1. On the other hand, orienting **longest to z** positions requires further operations. Steps to change aggregate's position to calculate the form index for the **longest to z** position were summarized as follows:

1. The aggregate was rotated so that its longest diameter lay on the z-axis.
2. Unity points were obtained by using spherical to Cartesian conversion and choosing $\Delta\phi = 90^0$ and $\Delta\theta = 1^0$ as shown in **Figure 34a**.
3. Two polar points were deleted from unity points in order to obtain perpendicular (z-axis) points as shown in **Figure 34b**.
4. Unity points were assumed as a ray and extended/shortened to the surface of aggregate as shown in **Figure 34c**.
5. Combining these radii, diameters were obtained.
6. The shortest among those diameters was the shortest perpendicular diameter and aggregate rotated around the z-axis so that the perpendicular shortest diameter lay on the x-axis.

After reorienting the aggregate, the radii were regenerated as in other positions and normalized FI values were calculated and presented in the following Chapter 5.

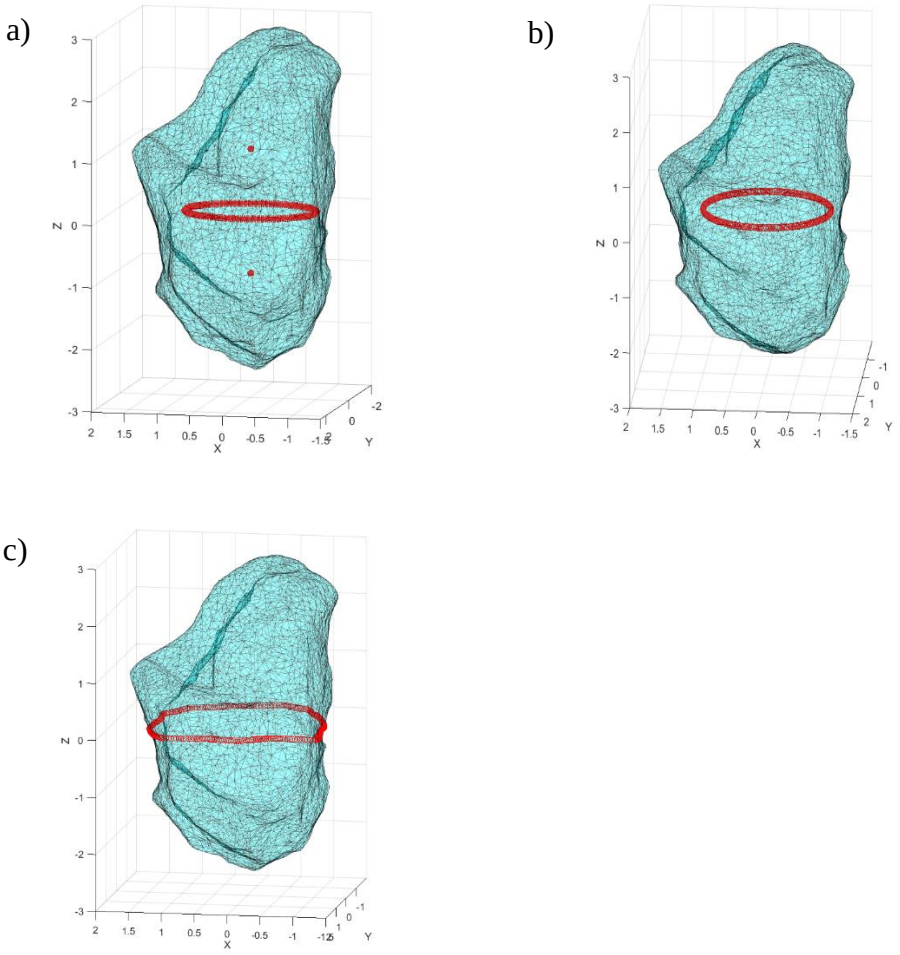

Figure 34 Generating radii that perpendicular (z-axis) a) ring with polar points b) unity radii ring when longest diameter on z-axis c) intersection points of radii perpendicular to z-axis.

4.4 Application of 2D Algorithms

The aggregates were analyzed three positions (**longest**, **side** and **vertical**) for the 2D method. Black-white (binary) TIFF images (**Figure 35a**) of the aggregate were imported to MATLAB in order to detect shape features and morphological indices. In order to use image processing tools of the MATLAB, the white pixel of the aggregate's image was converted to black and black pixels converted to white as

shown in **Figure 35b**. In other words, the aggregate should be represented by white pixels, and background should be represented by black pixels.

a) b)

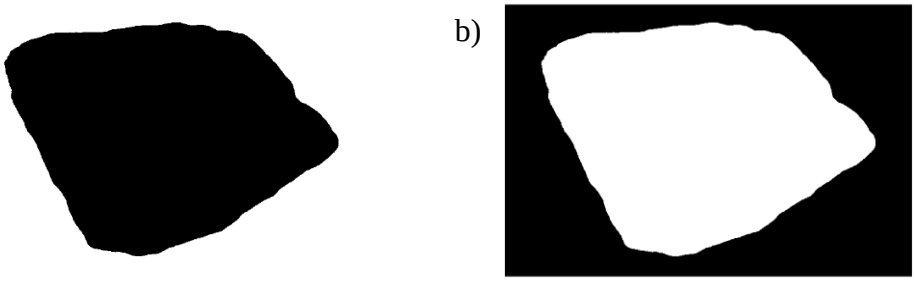

Figure 35 Binary images of aggregate a) image exported from ImageJ software b) white pixels was converted to black and black pixels to white

4.4.1 Shape Features

Longest, shortest and intermediate diameter of each aggregate was calculated by detecting the boundary coordinates of the binary image. Boundary coordinates of aggregate were detected by using MATLAB FEX Detect Boundary function [51]. The x and y coordinates of centroid (C_{2D}) were obtained by averaging x and y values of boundary coordinates, respectively. Then, the centroid of the aggregate was shifted to the origin of Cartesian coordinate system by subtracting C_{2D} from boundary coordinates. The centroid of each aggregate position would be $C_{2D} = (0, 0)$ from this stage.

Distances from the centroid to boundary image were assumed as the radii of the aggregate. Using MATLAB's four-quadrant inverse tangent function, the angle of each boundary coordinate was calculated. Consequently, by using angle and radius values, the diameters were generated. Then, the equivalent number of pixels to 1 mm length in the ruler was equated to convert the unity to the metric system. In other words, diameters were converted to mm by dividing their pixel vise values to the 1 mm equivalent pixel number. All diameters were obtained from **longest**, **side** and **vertical** positions of each aggregate and merged in one list. To sum up,

longest (L_{2D}), shortest (S_{2D}) and mean (M_{2D}) diameters were obtained for all aggregates.

As previously discussed for the proposed 3D approach, the aggregate initially should be rotated to get generalized FI and AI. The orientation of the longest diameter of each position (**longest**, **side,** and **vertical**) could be at any location as shown in **Figure 36a**. In order to generalize orientation of the images, the aggregates were rotated so that its positional longest diameter (i.e. longest diameter of **vertical** position) lay on the y-axis as shown in **Figure 36b**.

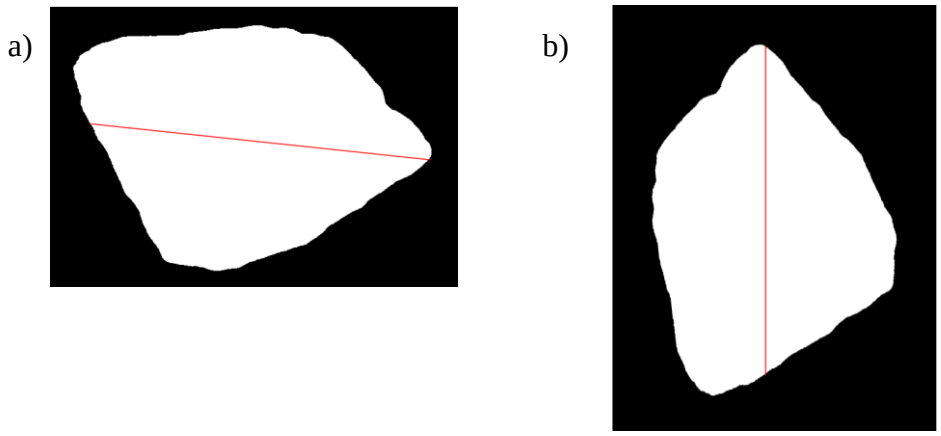

Figure 36 Rotation of binary image a) longest diameter and original position b) longest diameter rotated to y-axis

Area of each position ($A_{2D}^{longest}$, A_{2D}^{side} and $A_{2D}^{vertical}$) was calculated by using MATLAB's *bwarea()* function. Areas were used to get a weighted average of form and angularity indices, which will be discussed later in this section.

4.4.2 Form Index

As explained in section 4.2.2, the form index was calculated by defining initial and consequent radii with $\Delta\theta$ increments. In this study, As Masad suggested the $\Delta\theta$ was chosen as 4^0 [7]. Since the boundary coordinates and their radians were recorded, starting θ from 0^0 increased by $\Delta\theta$ each time. Using the recorded radii (**Figure 37**), which $\Delta\theta$ away from each other, FI_{2D} was calculated for the **longest**

($FI_{2D}^{longest}$), **side (FI_{2D}^{side})** and **vertical ($FI_{2D}^{vertical}$)** positions of each aggregate. Then by using the FI_{2D} and A_{2D} of each orthogonal binary image the FI_{2D}^{avg} (form index by weighted average) was calculated as explained in section 4.2.2.

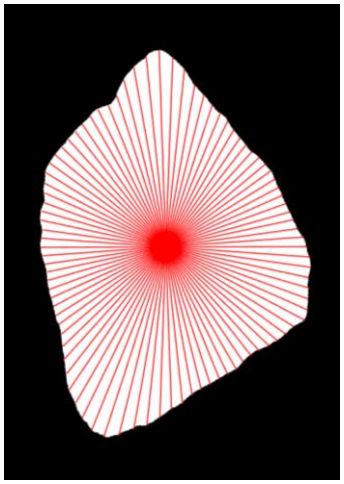

Figure 37 Radii Δθ degree away from each other

4.4.3 Angularity Index

As explained in section 4.2.1, to calculate the angularity index, it is essential to generate equivalent ellipse radii to aggregate radii. The radii of the aggregate were determined by $\Delta\theta$ degree ($\Delta\theta = 4^0$) increments. The equivalent ellipse radii can be generated for two different ellipses which are:

- **Ellipse by mean**: Ellipse's first semi-axis (a_{2D}) is the longest half diameter in the current position of aggregate (**longest, side** or **vertical**). The second semi-axis (a_{2D}) is the mean half diameter of the current position.
- **Ellipse by smallest:** Ellipse's semi-axes were generated by using the longest half diameter of overall positions ($\frac{L_{2D}}{2}$) and shortest half diameter of overall aggregate ($\frac{S_{2D}}{2}$). Depending on the position of aggregate semi-axis was chosen as follows:
    - **Longest position**: $a_{2D} = \frac{L_{2D}}{2}$, $b_{2D} = \frac{S_{2D}}{2}$

- **Side position**: $a_{2D} = \frac{L_{2D}}{2}$, $b_{2D} = \frac{S_{2D}}{2}$
- **Vertical position**: $a_{2D} = \frac{S_{2D}}{2}$, $b_{2D} = \frac{S_{2D}}{2}$

In the previous study, Oztur and Rashidzade [48] were used **ellipse by mean** in order to calculate the 2D angularity index (AI_{2D}). **Ellipse by mean** approach assumes each position' of the aggregate separately. In other words, the features were calculated separately for each face of the aggregate and then weighted averages were taken. On the other hand, in this thesis AI_{2D} was calculated by using **ellipse by smallest** that uses 2D orthogonal images of aggregate to obtain 3D information. Also, instead of using mean diameter in this thesis the smallest diameter was used due to the high correlation of smallest diameter between 2D and 3D approaches as discussed in Chapter 5.

After generating the equivalent ellipse radii, the aggregate look like as shown in **Figure 38**. The red center dot represents centroid, yellow dots represent aggregate's radii in $\Delta\theta$ increments and red ellipse like ordered dots represents the equivalent ellipse radii. The AI_{2D} was calculate for **longest** ($AI_{2D}^{longest}$), **side** (AI_{2D}^{side}) and **vertical** ($AI_{2D}^{vertical}$) positions and weighted average of AI (AI_{2D}^{avg}) were calculated based on the discussed method in section 4.2.1.

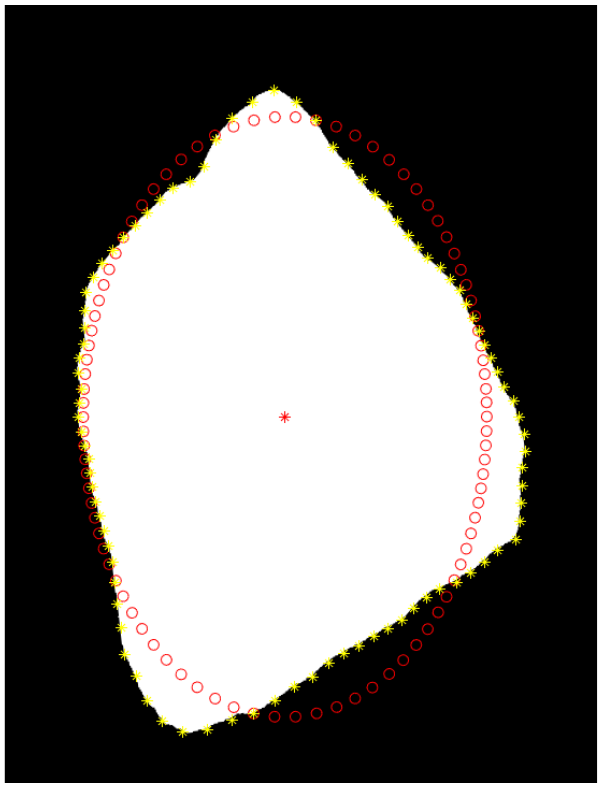

Figure 38 Yellow dots are aggregate radii and red dots are the corresponding ellipse radii

4.5 Summary of Chapter

This chapter contains detailed information about calculating centroid, surface area and volume of triangulated 3D model of aggregate. Also, introduces steps to create artificial radii by using spherical or ellipsoidal to cartesian conversion and ray-triangle intersection. Using the radii, the 3D sample rotation and displacement, diameters, form and angularity indices discussed in this section in theoretical and practical way. This chapter also detailly explains the steps that required in order to calculated shape features and morphological indices by using 2D approach.

CHAPTER 5

RESULT AND DISCUSSION

This chapter presents the results and findings that were obtained by the application of algorithms presented in Chapter 4. This section compares the shape feature and morphological indices that were obtained from 3D and 2D approaches. Moreover, predicted and measured volumes that were obtained by using the 3D approach and laboratory experiments, were compared in this section. Effects of different angle increments and triangulations were also discussed in this section to reveal the sensitivity of the proposed approach to different variables.

5.1 Shape Features

This section discussed the shape features (dimensions and volumes) of the coarse aggregates and compared 3D results with 2D and/or laboratory measurement results.

5.1.1 Dimensions

In this section, the longest, shortest and mean dimensions that were calculated from the proposed 3D approach and 2D methods were compared. As presented in **Figure 39a,** the correlation between the longest dimensions obtained from 3D (L_{3D}) and 2D (L_{2D}) was very high and the coefficient of determination (R^2) was 0.97.

The shortest diameters of aggregates obtained from the 3D approach and 2D method were presented in **Figure 39b**. The R^2 was 0.90 and it was relatively high. On the other hand, the R^2 of mean diameters (**Figure 39c**) was 0.67 and it was lower than the R^2 of the longest and shortest diameters. In this section, 3D shortest

and mean diameters obtained by choosing $\Delta\theta = \Delta\phi = 4^0$. The angle increment was furher discussed with sensitivity analysis at the end of this chapter. Detailed values of dimensions for flat elongated, angular and round particles that obtained from 3D approach and 2D method tabulated in Appendix B.

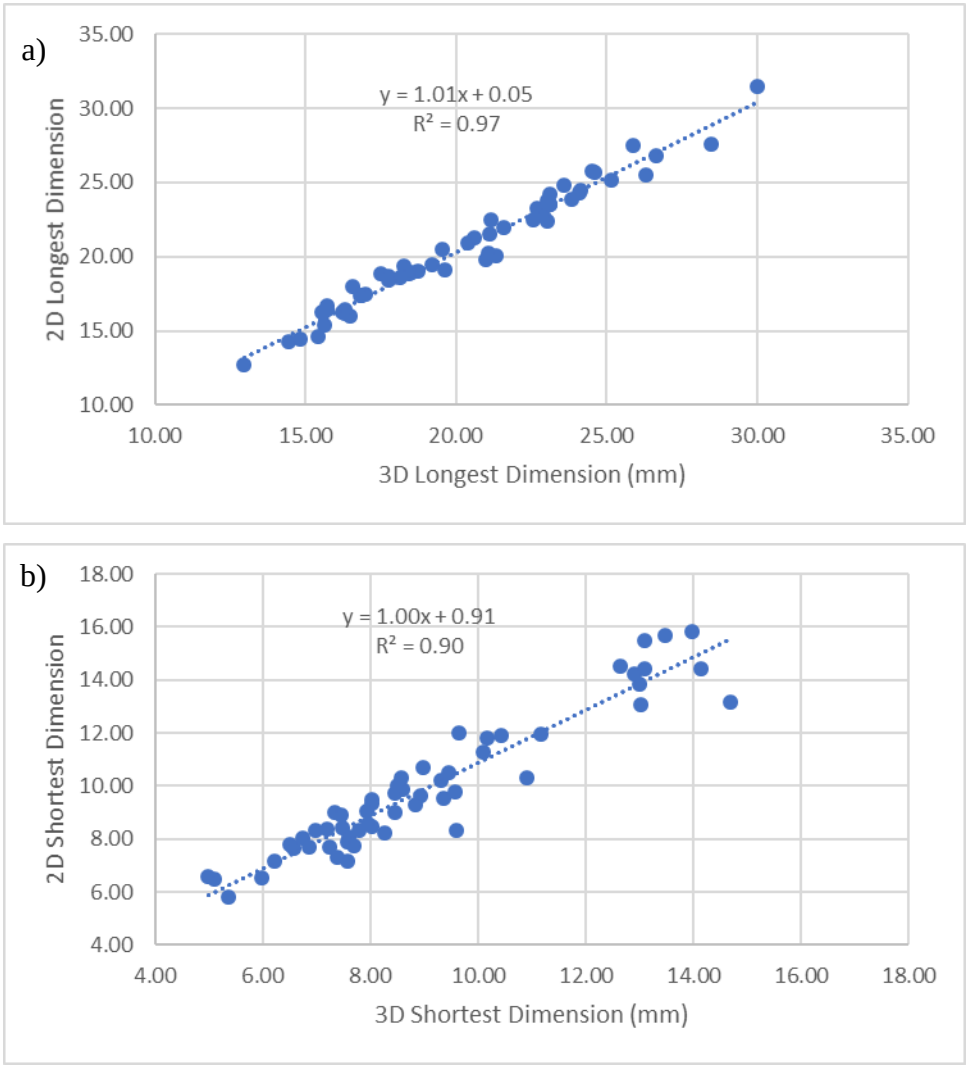

Figure 39 Comparison of 3D and 2D dimensions a) L_{3D} vs L_{2D} graph b) S_{3D} vs S_{2D} graph c) M_{3D} vs M_{2D} graph

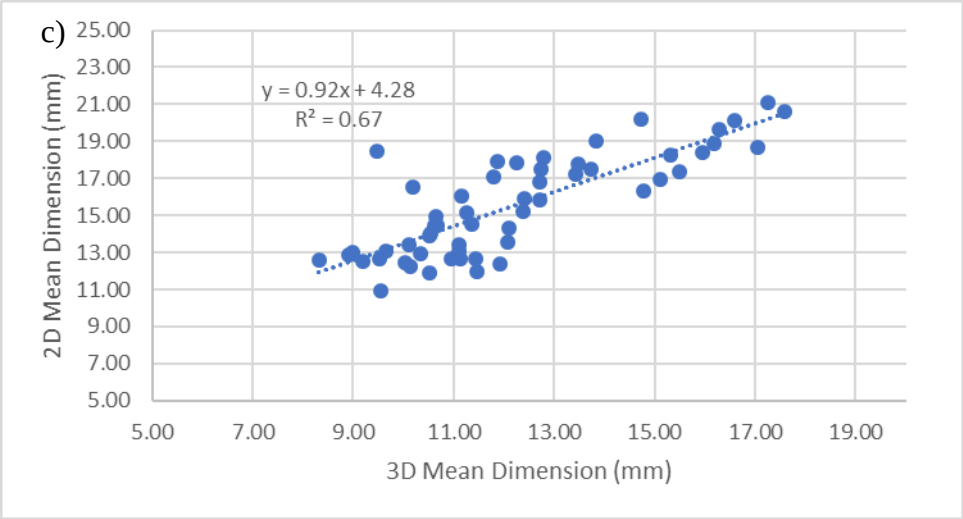

Figure 39 (cont'd) Comparison of 3D and 2D dimensions a) L_{3D} vs L_{2D} graph b) S_{3D} vs S_{2D} graph c) M_{3D} vs M_{2D} graph

As presented in **Figure 39a**, the correlation between the longest dimensions obtained from 3D (L_{3D}) and 2D (L_{2D}) was very high. It should be reminded that the positions of the aggregate in the 2D method were positioned manually, which might result in a slight mismatch with the longest dimensions. For instance (an exaggerated example), if the experimenter shoots the images of a cube from sides only, the diagonal line might not be captured. In this case, the L_{2D} will be smaller than L_{3D}. To eliminate this type of error, the cube should be fixed on its 1-2 edges and the camera should capture at other 6 - 7 edges. In other words, L_{2D} depends on the human factor whereas the 3D method calculates L_{3D} automatically independent from the human factor.

Considering the human factor discussed earlier, the linear correlation of shortest dimensions was slightly lower than the longest dimension as shown in **Figure 39b**. When 2D black and white images captured based on the dominating surface of the aggregate (largest area), the analyzes might not be able to detect the shortest dimension (S_{2D}). For the hypothetical figure shown in **Figure 40**, the two sides of the rectangular box are covered with thin rectangular planes, which have a size larger than the faces of the box. Assuming that the real centroid is located inside

the small box and it is required to capture three orthogonal images of aggregate. It would be significantly hard to capture the small rectangular box from the **longest**, **side** and **vertical** positions of the object since orthogonal binary images will show the planes as a larger box and the real box (smaller) smallest dimension could not be detected.

Also, it is a fact that the centroid of aggregate in the 3D model was not at the same location as in 2D. Therefore, this leads to the differences in the longest and shortest dimensions.

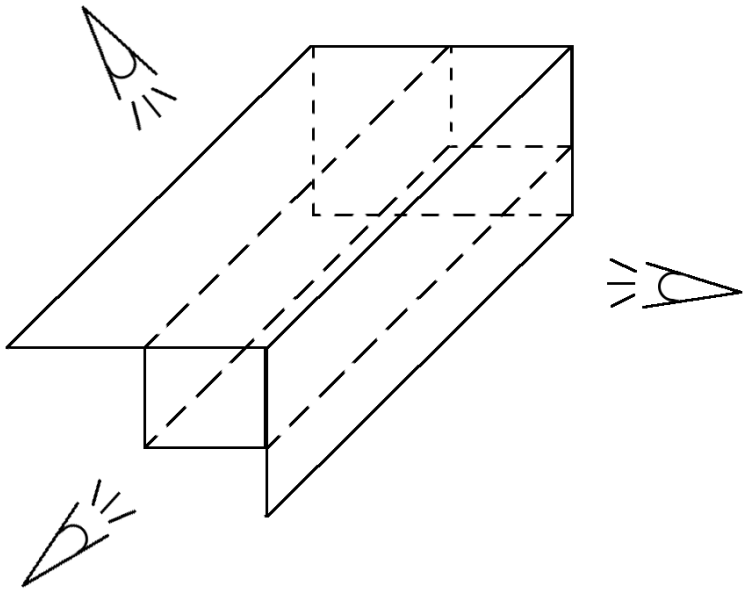

Figure 40 Hypothetical image where shortest diameter view blocked for 2D method's longest, side and vertical positions

The mean diameters obtained from 2D (M_{2D}) and 3D (M_{3D}) were also analyzed. As expected, the correlations were not as high as the shortest and longest diameters. The 3D mean diameters were different, as closely located diameters were dominating the mean diameters. In other words, for instance, for flat elongated aggregates, the number of dimeters that represent the flat portion (dominating surface) is more than the number of diameters that represent the

elongated portion of aggregate. Thus, there are significant differences between the 3D and 2D approaches.

5.1.2 Volume

Through the 3D model, it was also possible to calculate the volume of aggregates. The volumes obtained from 3D photogrammetry were also compared with the volumes obtained by laboratory experiments performed according to ASTM C127 (Standard Test Method for Relative Density and Absorption of Coarse Aggregate) [52] and the correlation was very high ($R^2 = 1.00$) as shown in **Figure 41**, which indicated the precision of the proposed approach.

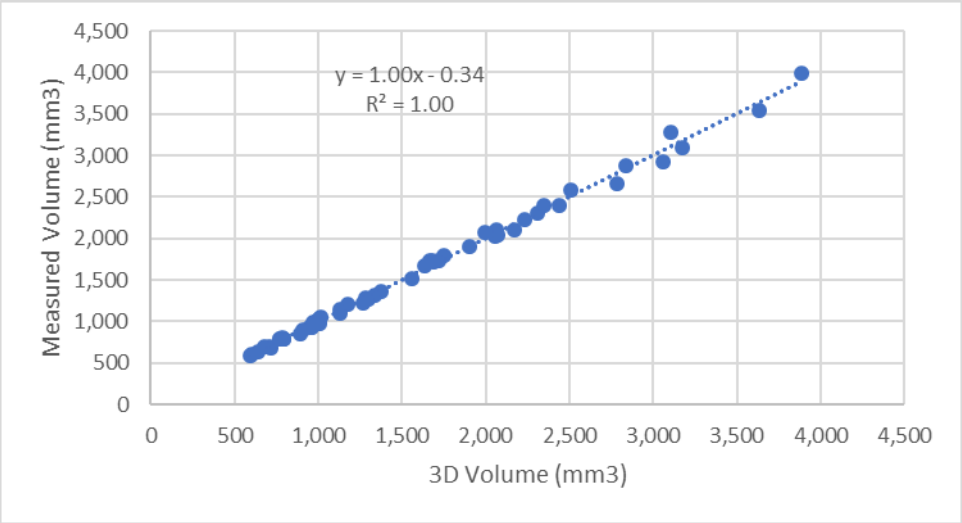

Figure 41 Volumes obtained from 3D photogrammetry vs ASTM C127 volumes

The proposed 3D method allowed users to calculate the volume of the complex shaped aggregate without any sensitive apparatus. Also, the precise volume calculation by using ASTM C127 requires more than a day for one aggregate, on the contrary, the proposed method only takes about 2-3 hours at the same precision level.

5.2 Morphological Indices

This section discussed the morphological indices of the coarse aggregates. It was aimed to compare the proposed 3D approach and 2D methods. Also, the section contains sensitivity analyze results according to aggregate type, different angle increments, triangulation size and triangulation distributions.

5.2.1 Form Index

This section presented the graphs of Normalized Form Index (NFI_{3D}) values that obtained from **shortest to z** and **longest to z positions** of aggregate versus FI_{2D}^{avg} determined by traditional 2D method. The NFI_{3D} that obtained by fixing aggregate's longest diameter to the x-axis and perpendicular shortest diameter to the z-axis (**shortest to z** position) compared with the weighted average of 2D form index in **Figure 42a**. The R^2 was 0.75 which was higher than the coefficient obtained from the previous study ($R^2 = 0.63$) [48]. The R^2 was increased to 0.90 by fixing the longest diameter (L_{3D}) to the z-axis and perpendicular shortest diameter (T_{3D}) to the x-axis as shown in **Figure 42b**. In this section, NFI_{3D} calculated by choosing $\Delta\theta = \Delta\phi = 4^0$ and FI_{2D}^{avg} was calculated by choosing $\Delta\theta = 4^0$. In addition, the form index values of three aggregates are shown in Appendix B. As the value of form indices (for both methods) gets smaller, the aggregate is more roundish and as it gets higher, the aggregate is more flat and elongated.

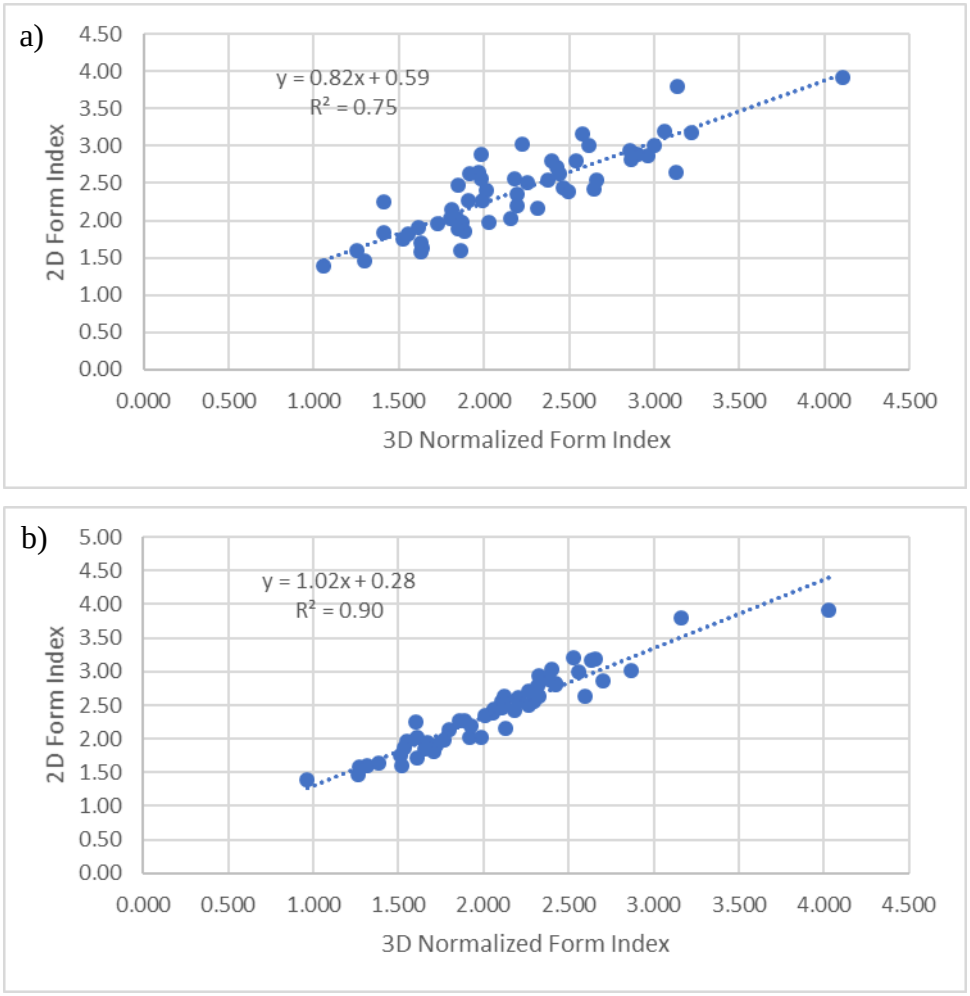

Figure 42 Comparison of 3D and 2D form indices a) NFI_{3D} obtained from **shortest to z** position of aggregate vs FI_{2D}^{avg} b) NFI_{3D} obtained from **longest to z** position of aggregate vs FI_{2D}^{avg}

The possible reasons that increase the linear correlation:

- In the previous study [48], the NFI_{3D} generated from **free z** position of aggregate by using radii at $\theta = 90^0$ and $\theta = 180^0$ (ϕ increased by $\Delta\phi$ for each θ) was highly correlated with FI_{2D} that was obtained from the **vertical** position ($FI_{2D}^{vertical}$). Since the aggregate does not have a generalized position around the x-axis, the FI_{2D}^{side} may or may not be correlated with

FI_{3D} that generated from $\theta = 0^0$ and $\theta = 270^0$ (ϕ increased by $\Delta\phi$ for each θ). Since, the weighted average calculated for 2D FI values, the **vertical** position generally had the smallest surface, thus its effect of $FI_{2D}^{vertical}$ was limited and therefore, the correlation NFI_{3D} for **free z** position of aggregate and FI_{2D}^{avg} was slightly low.

- The FI_{3D} generated from **shortest to z** position of aggregate at $\theta = 90^0$ and $\theta = 180^0$ (ϕ increased by $\Delta\phi$ for each θ) had a high correlation with $FI_{2D}^{vertical}$. The FI_{3D} generated from **shortest to z** position of aggregate at $\theta = 0^0$ and $\theta = 270^0$ (ϕ increased by $\Delta\phi$ for each θ) had correlated with FI_{2D}^{side}. If the weighted average of two highly correlated positions was considered, the correlation NFI_{3D} for **shortest to z** position of aggregate and FI_{2D}^{avg} was comparatively high.
- The FI_{3D} generated from **longest to z** position of aggregate by using radii at $\theta = 90^0$ and $\theta = 180^0$ (ϕ increased by $\Delta\phi$ for each θ) was highly correlated with $FI_{2D}^{longest}$. The FI_{3D} generated from **longest to z** position of aggregate at $\theta = 0^0$ and $\theta = 270^0$ (ϕ increased by $\Delta\phi$ for each θ) was also highly correlated with FI_{2D}^{side}. Taking a weighted average of two highly correlated positions which had larger areas increased the correlation of NFI_{3D} for **longest to z** position of aggregate and FI_{2D}^{avg} dramatically.

5.2.2 Angularity Index

The 3D Normalized Angularity Index (NAI_{3D}) that calculated by using **ellipsoid by smallest** was compared with the 2D weight averaged angularity index (AI_{2D}^{avg}) that was calculated by using e**llipse by smallest** as presented in **Figure 43**. The R^2 of NAI_{3D} and weighted average of 2D orthogonal angularity indices was determined as 0.77. In the previous study [48], the authors compared NAI_{3D} that obtained by **ellipsoid by mean** and AI_{2D}^{avg} by **ellipse by mean**. The R^2 was 0.74 in that previous research. As the value of angularity indices (for both methods) gets

smaller, the aggregate is more ellipsoidal or less angular and as it gets higher, the aggregate is more angular.

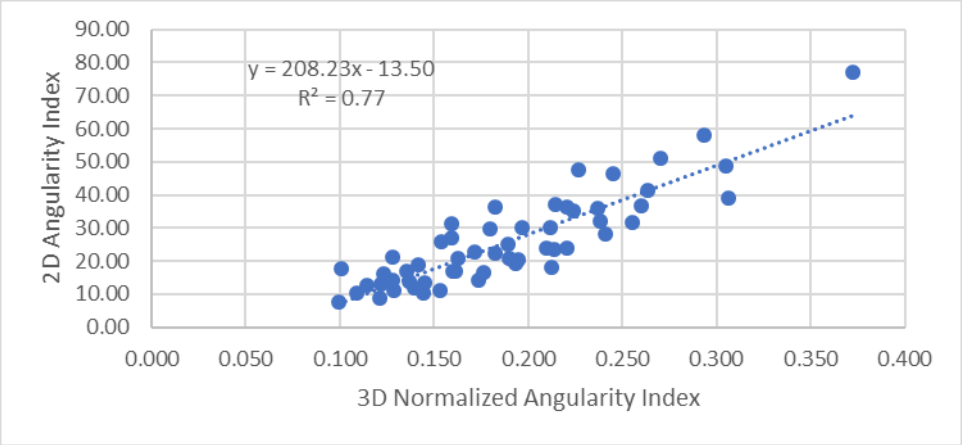

Figure 43 NAI_{3D} by ellipsoid by shortest vs. AI_{2D}^{avg} by shortest ellipse

Previously, each orthogonal images had its own ellipse which was independent from the ellipses generated at other positions until taking the weighted average. Therefore, the correlation between 2D and 3D angularity indices was not as high as in the new method. Also, the overall mean diameter, that used in 3D (M_{3D}), is not much related with mean diameter that obtained from each position of the aggregate in 2D. Therefore, using mean diameters, that was not highly correlated, did not result in a high correlation with 2D and 3D AI.

The new NAI_{3D} that was calculated by **ellipsoid by shortest** was slightly high correlated with the AI_{2D}^{avg} that was calculated by using the **shortest ellipse**. Since the correlation between the longest and shortest diameters was high than the correlation of mean diameters and triggering the 2D AI results as 3D, the correlation was slightly high.

5.3 Morphological Indices by Visual Inspection

In this section, four aggregates' NAI_{3D}, NFI_{3D} by **shortest to z** and **longest to z** values presented in **Figure 44**. The image contains angular (**Figure 44a**), flat and elongated and angular (**Figure 44b**), and two round samples (**Figure 44c** and **44d**). Samples **a** and **b** are both angular particles and the code detected them correctly. The NFI_{3D} of sample **a** reduced when calculated by using **longest to z** position and increased for sample **b** which also makes sense because sample **b**'s flat and elongates more than **a**. On the other hand, NFI_{3D} by **shortest to z** of sample a is less than sample a. It very hard to say how much should be difference therefore both NFI_{3D} values make sense.

Both samples **c** and **d** are round and indices support the visual inspection. The 3D approach was able to detect that, sample **d** slightly angular than sample **c**. On the other hand, sample **c** is slightly flatter than sample **d**. Conforming this information by visual inspection is really hard and results may vary depending on the inspector. Therefore, it is safer to compare the results by using the 2D approach.

Figure 44 Aggregate's morphological indices a) angular b) flat and elongated c) round d) round

5.4 Morphological Indices by Aggregate Source

In this section, NAI_{3D}, NFI_{3D} by **shortest to z** and **longest to z** position were results based on the aggregate source are given in **Figure 44a**, **44b** and **44c**, respectively. The average values of morphological indices clustered under aggregate sources from Basalt, Dolomite, Limestone, Perlite and River Gravel (one specially selected flat elongated aggregate excluded).

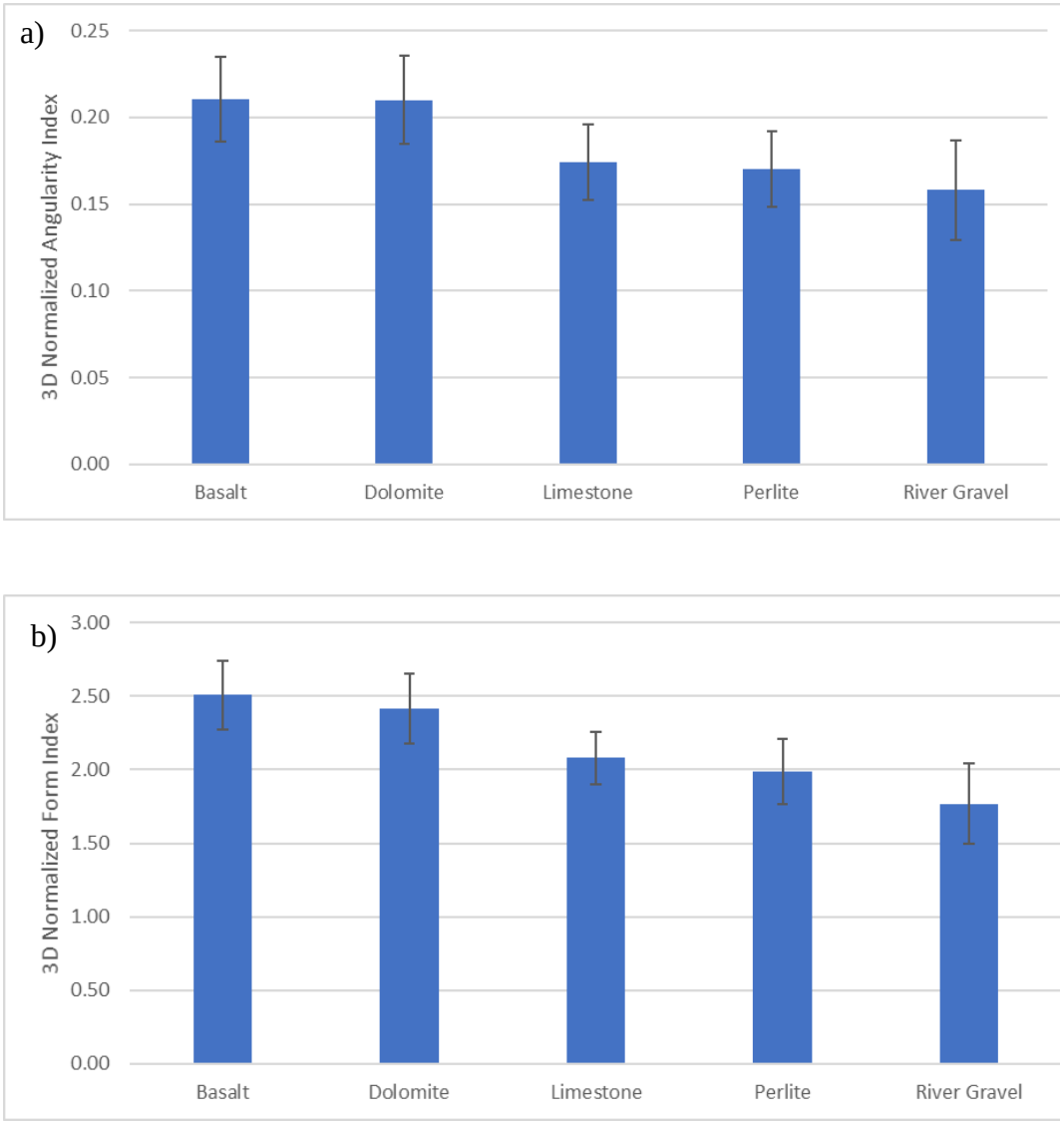

Figure 45 Average and standard deviation values of morphological indices by aggregate source a) Normalized Angularity Index b) 3D Normalized Form Index by shortest to z position c) 3D Normalized Form Index by longest to z position

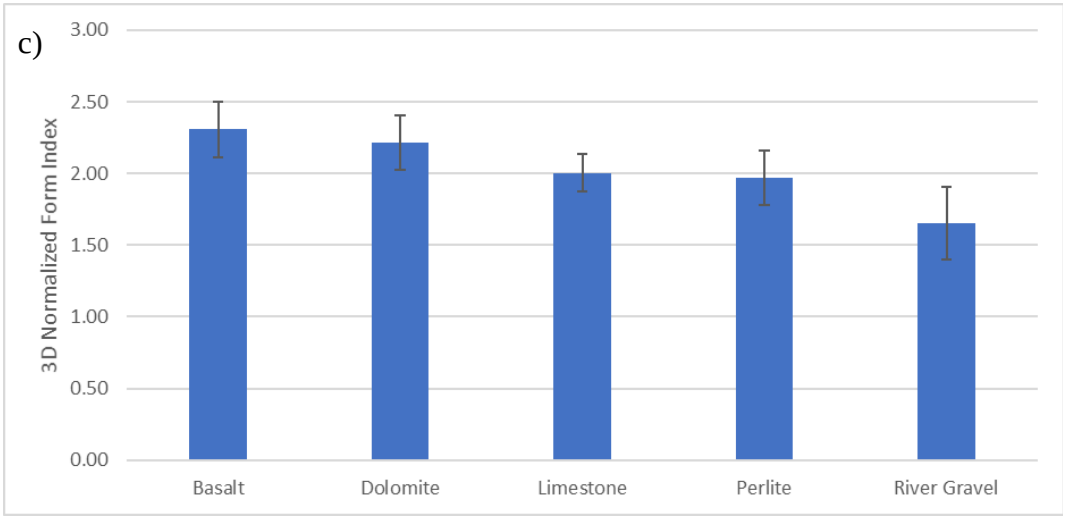

Figure 45 (cont'd) Average and standard deviation values of morphological indices by aggregate source a) Normalized Angularity Index b) 3D Normalized Form Index by shortest to z position c) 3D Normalized Form Index by longest to z position

5.5 Sensitivity Analysis

5.5.1 The Sensitivity of the Morphological Indices to the Angle Increments

Within this study, the angle increments used in the shape features and morphological indices analysis were kept constant at 4°. However, the selection of these criteria was not discussed up to this point. Therefore, in this section, the sensitivity of the proposed 3D method to angle increment was studied. In this study, angle increments were kept equal ($\Delta\theta = \Delta\phi$) for NAI_{3D} and NFI_{3D} and in this section differences of morphological indices for different angles (still $\Delta\theta = \Delta\phi$) were presented. All indices compared with the value obtained for 1^0 increments.

The NAI_{3D} values for different $\Delta\theta$ (=$\Delta\phi$) angle increments were given in **Table 2**. The angle increments from 1^0 to 90^0 degree for flat and elongated, angular and round particles were compared with the result of NAI_{3D} that was calculated for 1^0

increment. Up to 10^0, the differences in $NAI_{3D}$was less than 5%. It was concluded that the predicted NAI_{3D} the diffrence between 1° and 4° was less than 2%. Considering the runtime (section 5.6), the difference was assumed to be acceptable in this study.

Table 2 3D Normalized Angularity Index (NAI_{3D}) values and differences at different angle increments.

	NAI_{3D}			Difference, %		
$\Delta\theta$	Flat and Elongated	Angular	Round	Flat and Elongated	Angular	Round
1	0.37	0.22	0.11	0.00	0.00	0.00
2	0.37	0.22	0.11	0.03	0.46	0.15
3	0.37	0.23	0.11	0.19	0.97	0.26
4	0.37	0.23	0.11	0.05	1.45	0.45
5	0.37	0.23	0.11	0.13	1.85	0.53
6	0.37	0.23	0.11	0.35	2.34	0.59
9	0.37	0.23	0.11	0.06	3.93	0.88
10	0.37	0.23	0.11	0.20	4.21	0.89
15	0.37	0.24	0.11	0.04	5.33	0.59
20	0.38	0.23	0.11	0.89	3.51	0.10
30	0.36	0.24	0.11	2.87	5.90	1.02
45	0.40	0.22	0.10	7.86	0.44	3.76
90	0.74	0.34	0.07	98.08	52.33	31.39

Moreover, the NFI_{3D} values that were determined by using **shortest z** and **longest z** position generated for different angle increments were also studied and given in **Table 3a** and **3b,** respectively. The NFI_{3D} by **shortest to z** is less sensitive to angle increment when compared to the NFI_{3D} by **longest to z**. Normalized form index difference up to 10^0 was less than 7% for **shortest to z** position. On the other hand, the NFI_{3D} by **longest to z** difference up to 10^0 was slightly passed by 10%. The difference of NFI_{3D} values that obtained by using $\Delta\theta = \Delta\phi = 4^0$ was less than 5% when compared to the values obtained by using $\Delta\theta = \Delta\phi = 1^0$, which was also accepted within the accuracy margin of the study.

Table 3 3D Normalized Form Index (NFI_{3D}) values and differences at different angle increments a) obtained by using shortest z position of aggregate b) obtained by using longest z position of aggregate.

a)

NFI_{3D} (by shortest to z)				Difference, %		
$\Delta\theta$	Flat and Elongated	Angular	Round	Flat and Elongated	Angular	Round
1	4.24	3.00	1.10	0.00	0.00	0.00
2	4.17	3.00	1.08	1.70	0.04	1.54
3	4.15	3.00	1.07	2.10	0.01	2.56
4	4.11	3.00	1.06	3.20	0.10	3.20
5	4.09	2.99	1.05	3.53	0.24	4.19
6	4.07	2.99	1.05	4.01	0.51	4.56
9	4.01	2.97	1.03	5.55	1.16	6.25
10	4.02	2.96	1.02	5.35	1.48	6.89
15	3.93	2.93	0.96	7.25	2.21	12.06
20	3.79	2.86	0.96	10.55	4.70	11.95
30	3.95	2.90	0.87	6.96	3.49	20.43
45	3.91	2.50	0.84	7.90	16.71	23.59
90	2.90	1.91	0.46	31.55	36.21	58.18

b)

NFI_{3D} (by longest to z)				Difference, %		
$\Delta\theta$	Flat and Elongated	Angular	Round	Flat and Elongated	Angular	Round
1	4.12	2.91	1.01	0.00	0.00	0.00
2	4.08	2.89	0.99	1.00	0.49	1.84
3	4.05	2.89	0.97	1.67	0.73	3.32
4	4.03	2.87	0.97	2.27	1.27	4.26
5	3.95	2.86	0.96	4.10	1.50	4.92
6	3.92	2.840	0.94	4.84	2.37	6.54
9	3.87	2.80	0.91	6.05	3.79	9.78
10	3.80	2.78	0.91	7.79	4.55	10.25
15	3.71	2.72	0.86	9.93	6.41	14.75
20	3.71	2.67	0.82	10.10	8.13	18.24
30	3.83	2.57	0.75	7.16	11.68	25.93
45	4.27	2.72	0.69	3.67	6.49	31.22
90	5.24	3.03	0.57	27.04	4.15	43.65

5.5.2 The sensitivity of Analysis to Triangulation

In this section, the results of normalized 3D angularity and form indices by using over ($\cong 50 \frac{points}{mm^2}$), default ($\cong 8 \frac{points}{mm^2}$) and under ($\cong 2 \frac{points}{mm^2}$) were presented. Three particles, (i) flat and elongated, (ii) angular and (iii) round, were used in this section in order to discuss the findings. Also, the sensitivity to uniform and non-uniform triangulations of these aggregates was separately analyzed in this section.

In this thesis, it was previously assumed that the over triangulated models represent the surface of the particles in more detail. Therefore, the morphological indices obtained by using default and under triangulation were compared with the indices obtained by using over triangulation.

The NAI_{3D} values obtained by using **ellipsoid by shortest** for different triangulations were shown in **Figure 46a**. Difference of NAI_{3D} between default and over triangulation was less than 1%, whereas the variation was less than 10% for under triangulation. On the other hand, it was observed that the NFI_{3D} by **shortest to z** position (**Figure 46b**) was less sensitive to triangulation size and differences were less than 2% for both default and under triangulation. The NFI_{3D} obtained by using **longest to z** position (**Figure 46c**) was more sensitive to triangulation size when compared to the NFI_{3D} by **shortest to z** position and differences were less than 10%.

a)

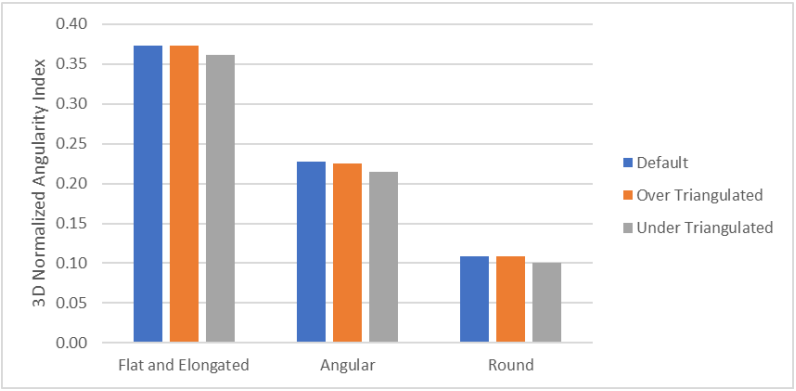

Figure 46 Morphological index values for default, over and under triangulation a) NAI_{3D} b) NFI_{3D} by shortest to z position c) NFI_{3D} by longest to z position

b)

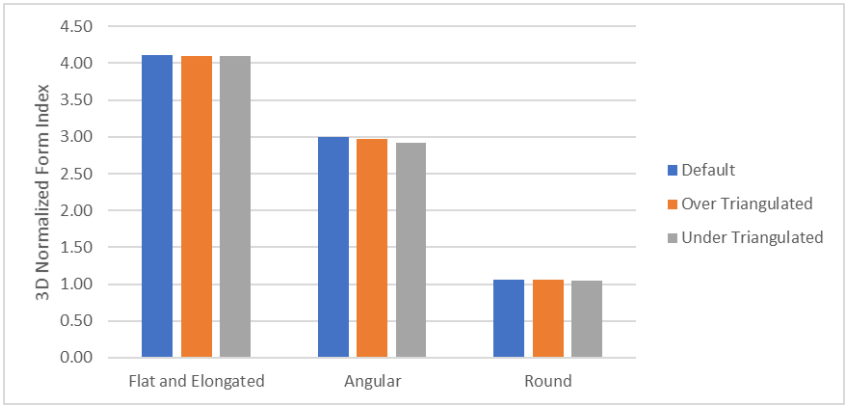

c)

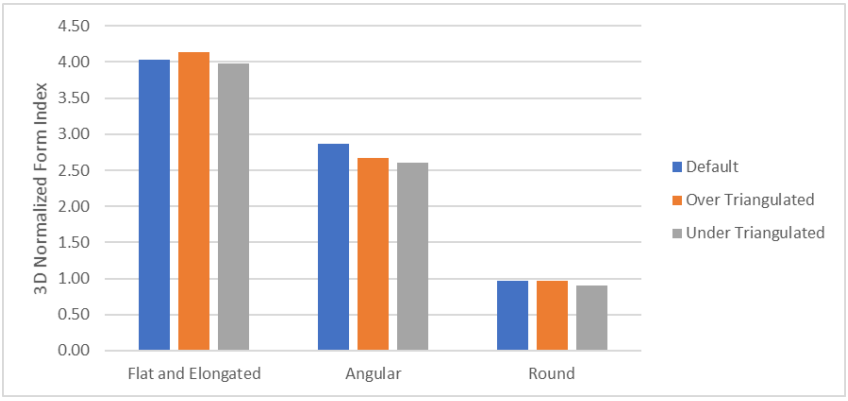

Figure 46 (cont'd) Morphological index values for default, over and under triangulation a) NAI_{3D} b) NFI_{3D} by shortest to z position c) NFI_{3D} by longest to z position

The different triangulations of flat and elongated, angular, and round aggregates were illustrated in **Figure 47a, 47b and 47c,** respectively. Since the run duration increased dramatically as angle increment gets smaller, the sensitivity analyzes were implemented only on three aggregates. Also, the sensitivity of aggregate was tested on non-uniform triangle distribution. The under-triangulated model of flat and elongated (**Figure 47a**) and round (**Figure 47c**) samples were non-uniformly distributed. The maximum difference of flat and elongated and round particles' NAI_{3D} and NFI_{3D} by **longest to z** that obtained in under and over triangulated model was less than 10% and NFI_{3D} by **shortest to z** differences were less than 1%. On the other hand, the differences of particles' NAI_{3D} and NFI_{3D} by **shortest to z** that obtained in default and over triangulated model was less than 1% and

NFI_{3D} by **longest to z** differences were less than 8%. It was concluded that the maximum difference between over and default triangulation in all indices were less than 10%. Therefore, the default triangulation was used in the overall study.

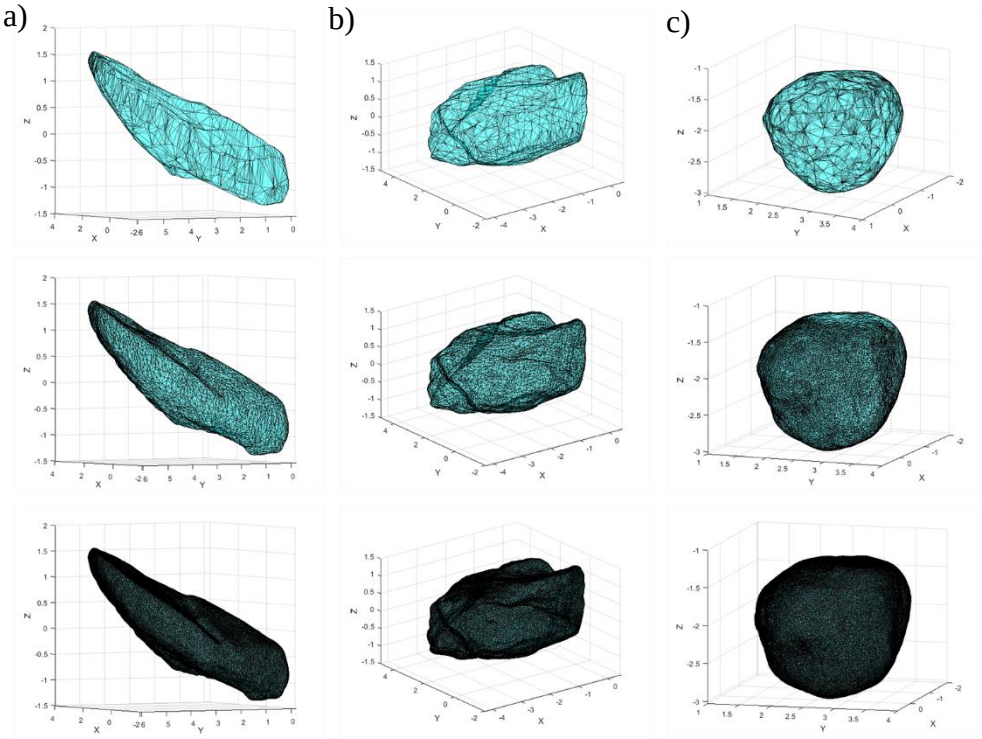

Figure 47 Top to bottom under, default and over triangulated aggregates. a) flat and elongated b) angular c) round

5.6 The efficiency of the proposed algorithm

In this section, the developed MATLAB code was analyzed in terms of running time. The code run in the device that parameters is mentioned in Chapter 3. Depending on triangulation size and angle increment, the run time may vary for three samples that flat and elongated, angular and round particles. The run time was around 10-20 minutes for over, and less than 5 minutes for both default and under triangulation as shown in **Figure 48a**. The run time dramatically increased as the angle increment gets smaller as shown in **Figure 48b**. Therefore, it was concluded

that the user may reduce the run duration by choosing the optimum triangulation size and angle increment. This thesis mainly analyzed shape feature and morphological indices for $\Delta\theta = \Delta\phi = 4^0$ and run duration is less than 5 minutes for that specific angle increment.

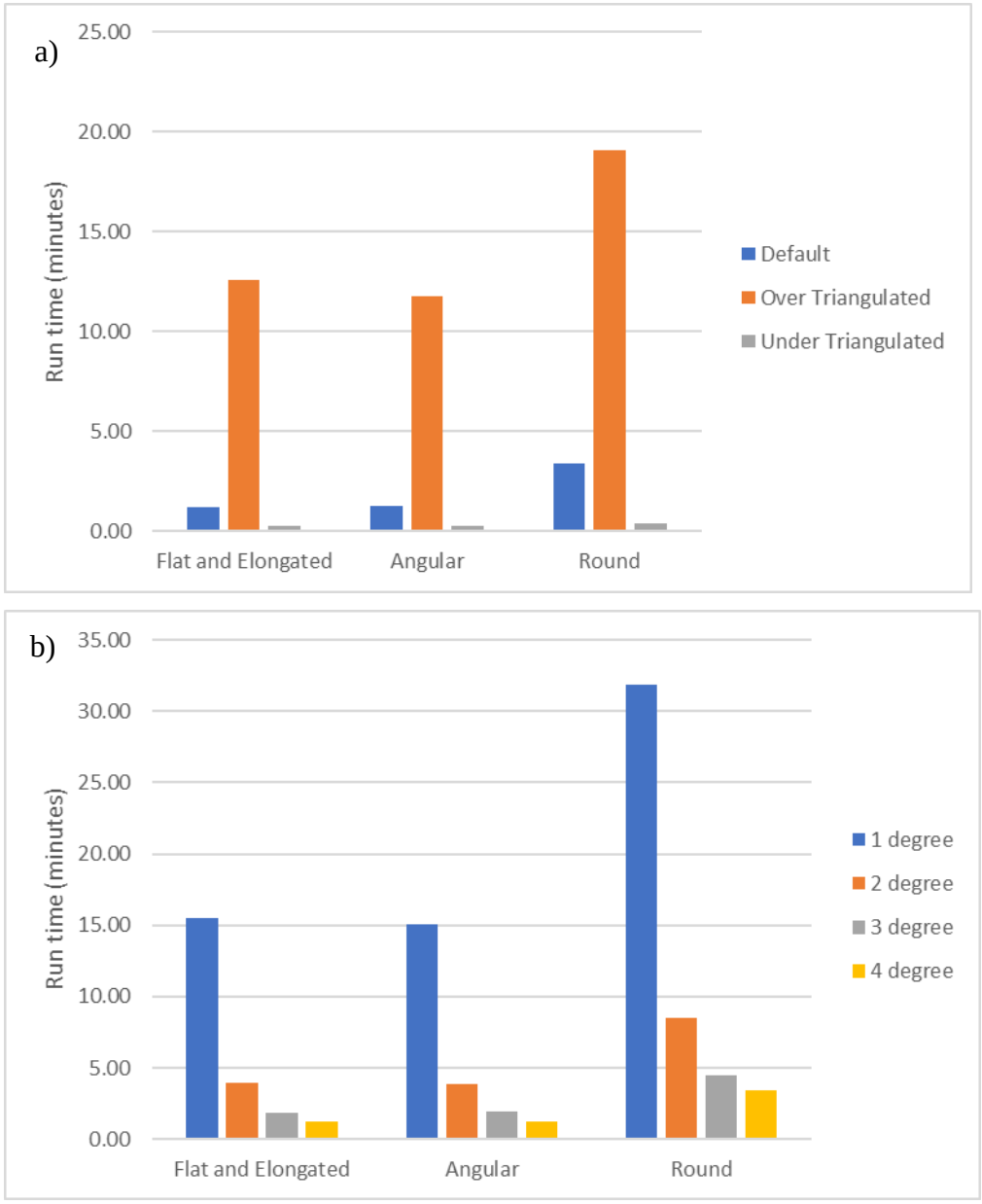

Figure 48 Run duration in minutes a) for over, default and under triangulation b) for different angle increment

5.7 Summary of Chapter

This chapter compared the shape features and morphological indices obtained from 3D and 2D approaches. It was concluded that while the longest and shortest diameters were highly correlated, the median diameters were poorly correlated due to shortcomings of traditional 2D methodologies. Also, correlations between morphological indices 2D and 3D were studied and the findings agreed with previous studies in the literature. Besides, the sensitivity of the proposed approach was studied in detail and assumptions of this study were verified.

CHAPTER 6

CONCLUSIONS AND RECOMMENDATIONS

6.1 Conclusions

The morphology of coarse aggregates significantly affects the performance of flexible pavements. This study introduces a novel 3D approach based on 3D photogrammetry to measure morphological indices and shape features. Although there are limited new studies that utilized photogrammetry in the construction industry, this study was the first detailed attempt that utilized photogrammetry to determine the aggregate properties.

In this study, the aim was to develop a cost-effective alternative to existing 3D techniques (i.e. X-Ray CT, laser scanning, etc.) using a digital camera. Within this study, a detailed guideline including a testing setup and analysis methodology was introduced to measure morphological indices (angularity and form indices) and also shape features (volume, surface area, and diameters) utilizing the triangulated 3D aggregate model that was obtained by 3D photogrammetry method.

The 3D aggregate surface model was constructed utilizing 2D images all around surface images. The point cloud data gathered from the surface model was analyzed, edited, and meshed using commercial and free software as discussed in the previous chapters in detail. Then, this data was used to determine the shape features and proposed morphological indices. Moreover, these features and indices were compared with respect to the traditional 2D approach. Besides, in order to evaluate the success of the proposed method, the predicted volumes and laboratory measurements were also associated.

Based on these analyses, the following conclusions were drawn:

- Longest, shortest, and mean dimensions were obtained using the proposed approach and major diameters obtained from orthogonal binary images of the aggregates were compared. The coefficient of determinations of longest, shortest and mean diameters were determined as 0.97, 0.90, and 0.67, respectively. Moreover, the correlations between the longest and shortest dimensions were also agreed with laboratory measurements. On the other hand, the mean dimension depends on the overall shape, and thus the correlation was relatively low. It indicates the precision and significance of the 3D approach.
- The predicted and measured volumes of coarse aggregates proved the precision of the proposed 3D approach as R^2 is equal to 1.00.
- Both form and angularity indices proposed in this study were normalized with respect to the number of data points on the surface of the aggregates to eliminate the effect of the magnitude.
- It was proven that triangulation is critical for the accuracy of the proposed method.
- Normalized 3D Angularity Index (NAI_{3D}) of coarse aggregates were determined and compared with the angularity index obtained by 2D method (AI_{2D}^{avg}). The semi-axis of the ellipse of AI_{2D}^{avg} calculated by using longest and shortest diameters of aggregate than obtained from orthogonal images. The determination coefficient of NAI_{3D} and AI_{2D}^{avg} was slightly high ($R^2 = 0.77$) when compared to a previous study [48]. Since 3D and 2D longest and shortest diameters are highly correlated, using these diameters as semi-axes of ellipsoid and ellipse increased the angularity indices' correlation.
- The NAI_{3D} values that calculated for different shaped particles at 1^0 ($= \Delta\phi = \Delta\theta$) angle increment was compared with different angle increments in order to measure the sensitivity of these parameter to angle increments. Consequently, the maximum difference NAI_{3D} that was obtained by using

4^0 and 1^0 angle increments was less than 2%. Therefore, it was assumed that 4^0 angle increments are accurate for the proposed approach. Moreover, the NAI_{3D} also analyzed for different number and distribution of triangles that formed the 3D particle surface and results were sufficiently acceptable.

- 3D form index (FI_{3D}) of particles were determined by using two different positions of aggregates in this study. **Shortest to z** position obtained by rotating aggregate so that its longest diameter (L_{3D}) fixed to x-axis and perpendicular shortest diameter (T_{3D}) to z-axis and **longest to z** position obtained by fixing L_{3D} to z-axis and T_{3D} to x-axis. The FI_{3D} for both positions calculated by using the differences of radii in slice-like (crescent) order. It was proven that the form index depends on the position of the aggregate.
- The correlation between the Normalized 3D Form Index (NFI_{3D}) and the weighted averages of 2D form indices (FI_{2D}^{avg}) calculated from **shortest to z** and **longest to z** position were 0.75 and 0.90, respectively.

  The NFI_{3D} were also calculated utilizing different angle increments in the range of 1° to 90°. It was concluded that the NFI_{3D} by **shortest to z** was less sensitive than **longest to z.** The maximum difference was determined between 4^0 to 1^0 and was less than 5%. Also, the NFI_{3D} sensitivity tested for different triangle distribution and sizes, a maximum 10% difference was recorded.

As a summary, the proposed method measures morphological indices with high accuracy and overall process comparatively cheaper than the previous 3D studies. the total cost of the proposed imaging setup is less than 1000$. Therefore, it can be concluded that this thesis presents an economical measure of the morphology of aggregates by utilizing 3D photogrammetry. Moreover, the sample preparation, photoshoot, creation of the 3D model, and calculation of shape features and morphological indices take 30 minutes, 30-35 minutes, 20-60 minutes, and 5 minutes. In other words, the overall process takes in the range of 85-135 minutes, which is in fact not lengthly as compared to other 3D methods.

In conclusion, based on these findings discussed above, the proposed imaging approach can be successfully utilized as a quality control/assurance method by the construction industry.

6.2 Recommendations

In this study, 3D normalized indices were determined by rotating equal angle increments ($\Delta\phi$=$\Delta\theta$). On the other hand, in the feature studies, the effect and sensitivity of non-equal angle increments may be studied. It should be also noted that the mean diameter and angularity index are dependent on spherical and ellipsoidal conversions. Thus, the effects of distances between artificial radii on morphological indices may be further studied. Additionally, an extra sensitivity analysis can be added to the study to limit the number of images taken for obtaining the 3D model. Besides, the amount of time that is spent to prepare the aggregate samples and to capture the images can be reduced by designing a self-rotating imaging setup. Consequently, the system can be fully automated and commercially available for the use of industry.

In the near future, the existing conventional standards should be replaced with image-based direct quantitative analysis. Besides further studies are needed to link the morphological indices to mechanical performance of asphalt mixtures.

REFERENCES

[1] A. T. Papagiannakis and E. A. Masad, *Pavement Design and Materials*. Hoboken, NJ, USA: John Wiley & Sons, Inc., 2012.

[2] M. E. Kutay, H. I. Ozturk, A. R. Abbas, and C. Hu, "Comparison of 2D and 3D image-based aggregate morphological indices," *Int. J. Pavement Eng.*, vol. 12, no. 4, pp. 421–431, 2011.

[3] Y. Liu, F. Gong, Z. You, and H. Wang, "Aggregate Morphological Characterization with 3D Optical Scanner versus X-Ray Computed Tomography," *J. Mater. Civ. Eng.*, vol. 30, no. 1, 2018.

[4] H. Kim, C. T. Haas, A. F. Rauch, and C. Browne, "Wavelet-Based Three-Dimensional Descriptors of Aggregate Particles," *Transp. Res. Rec. J. Transp. Res. Board*, vol. 1787, no. 02, pp. 109–116, 2002.

[5] C. Jin, F. Zou, X. Yang, K. Liu, P. Liu, and M. Oeser, "Three-dimensional quantification and classification approach for angularity and surface texture based on surface triangulation of reconstructed aggregates," *Constr. Build. Mater.*, vol. 246, 2020.

[6] P. J. BARRETT, "The shape of rock particles, a critical review," *Sedimentology*, vol. 27, no. 3, pp. 291–303, 1980.

[7] E. Masad and T. Fletcher., "Aggregate imaging system (AIMS): basics and application," 2005.

[8] J. Chen, M. K. Chang, and K. Y. Lin, "Influence of Coarse Aggregate Shape on the Strength of Asphalt Concrete Mixtures," *J. East. Asia Soc. Transp. Stud.*, vol. 6, pp. 1062–1075, 2005.

[9] P. Cui, Y. Xiao, B. Yan, M. Li, and S. Wu, "Morphological characteristics of aggregates and their influence on the performance of asphalt mixture," *Constr. Build. Mater.*, vol. 186, pp. 303–312, 2018.

[10] S. S. Neham, R. K. Ali, and H. A. Ashour, “Evaluation of hot mix asphalt resilient modulus based on aggregate morphological properties,” *IOP Conf. Ser. Mater. Sci. Eng.*, vol. 433, no. 1, 2018.

[11] Y. Lei *et al.*, “Effect of key aggregate morphology and mold modulus on the spatial distribution of internal air voids in the compacted asphalt mixture,” *J. Test. Eval.*, vol. 48, no. 6, pp. 4324–4342, 2019.

[12] J. Gao, H. Wang, Y. Bu, Z. You, X. Zhang, and M. Irfan, “Influence of Coarse-Aggregate Angularity on Asphalt Mixture Macroperformance: Skid Resistance, High-Temperature, and Compaction Performance,” *J. Mater. Civ. Eng.*, vol. 32, no. 5, 2020.

[13] ASTM Standard D3398, “Standard Test Method for Index of Aggregate Particle Shape and Texture,” *ASTM Int.*, pp. 1–4, 2006.

[14] ASTM Standard D5821, “Standard Test Method for Determining the Percentage of Fractured Particles in Coarse Aggregate,” *ASTM Int.*, pp. 1–6, 2017.

[15] ASTM Standard D4791, “Standard Test Method for Flat Particles, Elongated Particles, or Flat and Elongated Particles in Coarse Aggregate,” *ASTM Int.*, pp. 1–4, 2019.

[16] H. Wadell, “Volume, shape, and roundness particles,” *J. Geol.*, vol. 40, no. 5, pp. 443–451, 1932.

[17] E. Masad, D. Olcott, T. White, and L. Tashman, “Correlation of fine aggregate imaging shape indices with asphalt mixture performance,” *Transp. Res. Rec.*, no. 1757, pp. 148–156, 2001.

[18] “Aggregate Image Measurement System (AIMS),” *U.S. Dep. Transp. Fed. Highw. Adm.*, 2017.

[19] C. Rao, E. Tutumluer, and J. A. Stefanski, “Coarse Aggregate Shape and Size Properties Using a New Image Analyzer,” *J. Test. Eval.*, vol. 29, no. 5,

pp. 461–471, 2001.

[20] C. Rao, E. Tutumluer, and I. T. Kim, “Quantification of coarse aggregate angularity based on image analysis,” *Transp. Res. Rec.*, no. 1787, pp. 117–124, 2002.

[21] H. Xu, J. A. Prozzi, M. Y. Kim, and J. B. Hernandez, “Characterization of Aggregate Angularity in the Frequency Domain,” *Transp. Res. Rec. J. Transp. Res. Board*, vol. 2674, no. 10, pp. 324–334, 2020.

[22] Y. Descantes, Y. Fosse, and F. Milcent, “Automated Measurement of Railway Ballast Angularity,” *J. Mater. Civ. Eng.*, vol. 18, no. 4, pp. 612–618, 2006.

[23] X. Xie, G. Lu, P. Liu, D. Wang, Q. Fan, and M. Oeser, “Evaluation of morphological characteristics of fine aggregate in asphalt pavement,” *Constr. Build. Mater.*, vol. 139, pp. 1–8, 2017.

[24] H. Huang, J. Luo, E. Tutumluer, J. M. Hart, and A. J. Stolba, “Automated Segmentation and Morphological Analyses of Stockpile Aggregate Images using Deep Convolutional Neural Networks,” *Transp. Res. Rec. J. Transp. Res. Board*, vol. 2674, no. 10, pp. 285–298, 2020.

[25] R. Girshick, J. Donahue, T. Darrell, and J. Malik, “Rich feature hierarchies for accurate object detection and semantic segmentation,” *Proc. IEEE Comput. Soc. Conf. Comput. Vis. Pattern Recognit.*, pp. 580–587, 2014.

[26] V. Nekrasov, J. Ju, and J. Choi, “Fully Convolutional Networks for Semantic Segmentation,” *Br. Mach. Vis. Conf. 2016, BMVC 2016*, vol. 2016-Septe, pp. 124.1-124.14, 2016.

[27] L. Pei *et al.*, “Pavement aggregate shape classification based on extreme gradient boosting,” *Constr. Build. Mater.*, vol. 256, 2020.

[28] E. J. Garboczi, “Three-dimensional mathematical analysis of particle shape using X-ray tomography and spherical harmonics: Application to aggregates

used in concrete," *Cem. Concr. Res.*, vol. 32, no. 10, pp. 1621–1638, 2002.

[29] C. Jin, F. Zou, X. Yang, and Z. You, "3D Quantification for Aggregate Morphology Using Surface Discretization Based on Solid Modeling," *J. Mater. Civ. Eng.*, vol. 31, no. 7 , 2019.

[30] X. Yang, S. Chen, and Z. You, "3D Voxel-Based Approach to Quantify Aggregate Angularity and Surface Texture," *J. Mater. Civ. Eng.*, vol. 29, no. 7, 2017.

[31] B. Sukumaran and A. K. Ashmawy, "Influence of inherent particle characteristics on hopper flow rate," *Powder Technol.*, vol. 138, no. 1, pp. 46–50, 2003.

[32] C. Y. Kuo, J. D. Frost, J. S. Lai, and L. B. Wang, "Three-dimensional image analysis of aggregate particles from orthogonal projections," *Transp. Res. Rec.*, 1996.

[33] L. Wang, X. Wang, L. Mohammad, and C. Abadie, "Unified Method to Quantify Aggregate Shape Angularity and Texture Using Fourier Analysis," *J. Mater. Civ. Eng.*, vol. 17, no. 5, pp. 498–504, 2005.

[34] A. du Plessis, S. G. le Roux, and A. Guelpa, "Comparison of medical and industrial X-ray computed tomography for non-destructive testing," *Case Stud. Nondestruct. Test. Eval.*, vol. 6, pp. 17–25, 2016.

[35] Z. Sun, C. Wang, X. Hao, W. Li, and X. Zhang, "Quantitative evaluation for shape characteristics of aggregate particles based on 3D point cloud data," *Constr. Build. Mater.*, vol. 263 , 2020.

[36] A. B. Heidelberg, M. Lanotte, and M. E. Kutay, "Three-Dimensional Reconstruction and Morphological Characterization of Aggregates Using Imaging and Spherical Harmonics," *J. Test. Eval.*, vol. 49, no. 4, 2021.

[37] L. Zhao, S. Zhang, D. Huang, X. Wang, and Y. Zhang, "3D shape quantification and random packing simulation of rock aggregates using

photogrammetry-based reconstruction and discrete element method," *Constr. Build. Mater.*, vol. 262, 2020.

[38] Bentley Systems, "ContextCapture User Guide," 11-Jan-2019. [Online]. Available: https://docs.bentley.com/LiveContent/web/ContextCapture Help-v9/en/GUID-E71D0658-82CD-46F3-B400-17F95A3939EE.html. [Accessed: 27-Aug-2020].

[39] Autodesk, "Meshmixer," Apr-2018. [Online]. Available: http://www.meshmixer.com/. [Accessed: 29-Aug-2020].

[40] R. Wayne, "ImageJ." [Online]. Available: https://imagej.nih.gov/ij/docs/intro.html. [Accessed: 26-Oct-2020].

[41] G. Peyre, "Toolbox Graph," *MATLAB Central File Exchange*, 19-Jul-2019. [Online]. Available: https://www.mathworks.com/matlabcentral/fileexchange/5355-toolbox-graph?s_tid=prof_contriblnk. [Accessed: 31-Aug-2020].

[42] I. Nystroem, J. K. Udupa, G. J. Grevera, and B. E. Hirsch, "Area of and volume enclosed by digital and triangulated surfaces," *Med. Imaging 2002 Vis. Image-Guided Proced. Disp.*, vol. 4681, no. May 2002, pp. 669–680, 2002.

[43] H. B. Newson, "On the Volume of a Polyhedron Published," in *Annals of Mathematics*, 1899, vol. 1, no. 1/4, pp. 108–110.

[44] A. R. Keneti and A. Jafari, "Determination of volume and centroid of irregular blocks by a simplex integration approach for use in discontinuous numerical methods," *Geomech. Geoengin.*, vol. 3, no. 1, pp. 79–84, 2008.

[45] T. Möller and B. Trumbore, "Fast, Minimum Storage Ray/Triangle Intersection," *ACM SIGGRAPH 2005 Courses*, p. 7, 2005.

[46] S. Sahli, "rotationVect3D(U, V, M_world)," *MATLAB Central File Exchange*, 2015. [Online]. Available:

https://www.mathworks.com/matlabcentral/fileexchange/49986-rotationvect3d-u-v-m_world. [Accessed: 08-Sep-2020].

[47] E. Masad, S. Saadeh, T. Al-Rousan, E. Garboczi, and D. Little, "Computations of particle surface characteristics using optical and X-ray CT images," *Comput. Mater. Sci.*, vol. 34, no. 4, pp. 406–424, 2005.

[48] H. I. Ozturk and I. Rashidzade, "A photogrammetry based method for determination of 3D morphological indices of coarse aggregates," *Constr. Build. Mater.*, vol. 262, 2020.

[49] A. A. Thabet, A. Hamzawy, and M. S. Badawi, "New mathematical approach to calculate the geometrical efficiency using different radioactive sources with gamma-ray cylindrical shape detectors," *Nucl. Eng. Technol.*, vol. 52, no. 6, pp. 1271–1276, 2020.

[50] T. Al-Rousan, E. Masad, E. Tutumluer, and T. Pan, "Evaluation of image analysis techniques for quantifying aggregate shape characteristics," *Constr. Build. Mater.*, vol. 21, no. 5, pp. 978–990, 2007.

[51] F. Alister, "Detect Boundary," *MATLAB Central File Exchange*, 2003. [Online]. Available: https://www.mathworks.com/matlabcentral/fileexchange/4249-detect_boundary-zip?s_tid=prof_contriblnk. [Accessed: 27-Oct-2020].

[52] ASTM Standard C127, "Standard Test Method for Relative Density (Specific Gravity) and Absorption of Coarse Aggregate," *ASTM Int.*, p. 5, 2015.

APPENDICES

A. 2D Binary Images and 3D Model

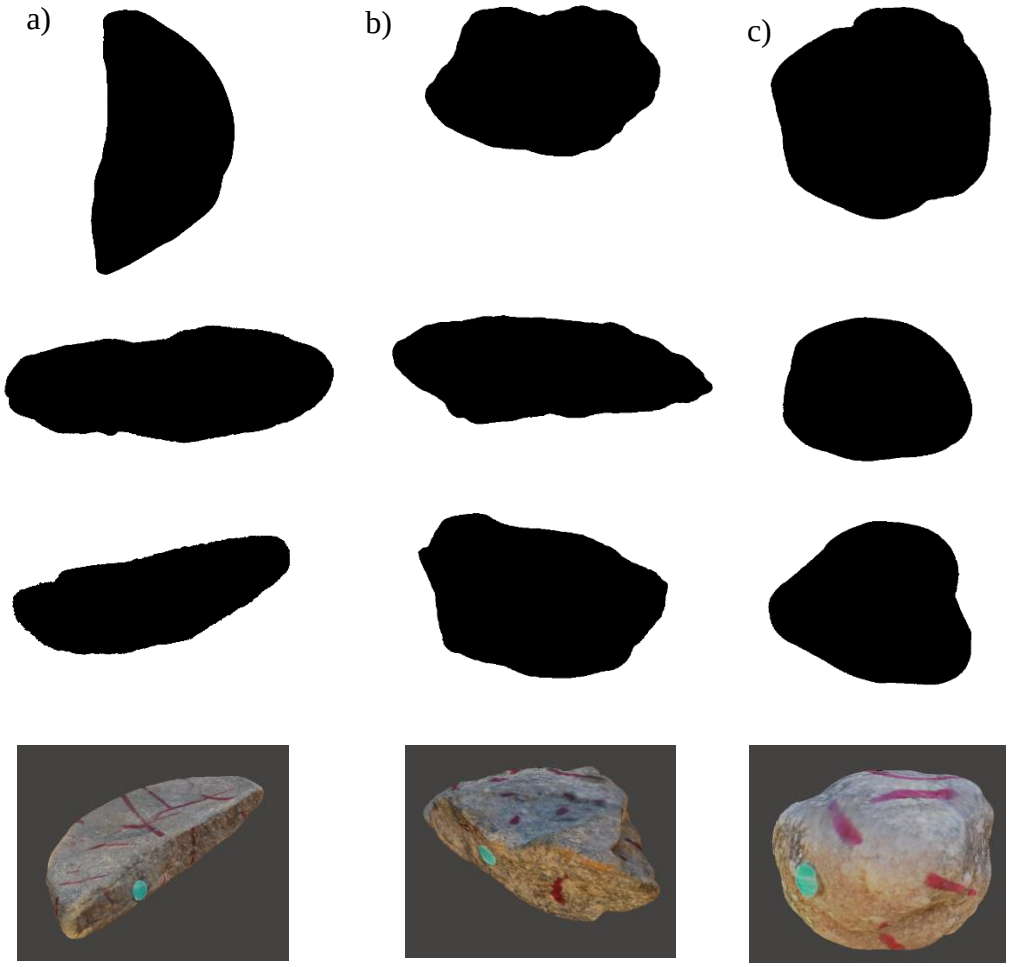

Figure A. 1 Binary images of aggregate top to down longest, side and vertical positions and 3D model a) flat and elongated b) angular c) round

B. Shape and Morphological Index Values by 2D and 3D Methods

Table B. 1 Values of diameters, surface areas, angularity indices and form indices of three aggregates that obtained from orthogonal images and 3D approach.

Shape	Flat and elongated	Angular	Round
Source	River Gravel	Basalt	River Gravel
Sieve size	1/2''	1/2''	3/8''
Area of longest position (mm^2)	434	313	141
Area of side position (mm^2)	209	183	116
Area of vertical position (mm^2)	112	174	102
Longest diameter of longest position (mm)	31.45	25.52	14.28
Longest diameter of side position (mm)	28.06	27.48	13.89
Longest diameter of vertical position (mm)	20.41	18.65	12.39
Shortest diameter of longest position (mm)	16.26	15.02	12.00
Shortest diameter of side position (mm)	8.77	8.09	10.40
Shortest diameter of vertical position (mm)	6.48	11.23	10.30
Mean diameter of longest position (mm)	24.41	20.35	13.40
Mean diameter of side position (mm)	18.15	17.42	12.26
Mean diameter of vertical position (mm)	13.36	15.25	11.42
AI of long position	103.69	56.13	12.48
AI of short position	28.05	8.04	6.93
AI of vertical position	66.19	73.21	11.04

Table B. 1 (cont'd) Values of diameters, surface areas, angularity indices and form indices of three aggregates that obtained from orthogonal images and 3D approach.

FI of long position	3.32	2.31	1.15
FI of short position	4.73	4.82	1.34
FI of vertical position	4.73	2.36	1.76
3D			
# of radii in point cloud	9,032	10,858	25,806
# of artificial radii ($\Delta\theta = \Delta\phi = 4^0$)	3,962	3,962	3,962
Surface area (mm^2)	1,030	933	519
Volume (mm^2)	1,555	1,667	998
Longest diameter (mm)	29.98	25.88	14.45
Shortest diameter (mm)	5.09	7.59	10.90
Mean diamerter	9.48	11.87	11.93
Angularity index by ellipse by shortest	1,476	899	431
Normalized Angularity Index	0.37	0.23	0.11
Form index by shortest to z position	258.48	188.72	66.73
Normalized Form Index by shortest to z position	4.11	3.00	1.06
Form index by longest to z position	253.57	180.74	60.78
Normalized Form Index by longest to z position	4.03	2.87	0.97